Sub-synchronous Interactions in a Wind Integrated Power System

by

Don Hiranya Ravipriya Suriyaarachchi

A thesis submitted to the Faculty of Graduate Studies in partial fulfillment of the requirements for the degree of Doctor of Philosophy

The Department of Electrical and Computer Engineering
The University of Manitoba
Winnipeg, Manitoba, Canada

To my wife Erandi and little son.....

Acknowledgements

This thesis is the outcome of several years of hard work and struggle. I may have not made it through if I have not received the support of some wonderful people throughout this period. It's an honour for me to extend my heartiest gratitude to all of them at this juncture.

First, my sincere gratitude must go to my advisor, Professor Udaya Annakkage, for his continuous advice, guidance, encouragement and patience throughout the course of this work. It has been a privilege to work under his guidance. I must also thank Dr. Darshana Muthumuni of the Manitoba HVdc Research Center for his support during the initial stages of my research.

Conducting this work would not have been possible without the financial support from the University of Manitoba, Manitoba Hydro and the Natural Sciences and Engineering Research Council.

My special thanks goes to Dr. Chandana Karawita of TransGrid Solutions Inc. for useful advice, support and encouragement throughout the research. I would like to thank all my friends and the staff of the Department of Electrical and Computer Engineering for their continuous encouragement and for making my years at the University of Manitoba a pleasant experience.

This acknowledgment would not be complete without thanking my family. I extend my heartfelt gratitude to my wife Erandi and my son for their patience, understanding and encouragements whenever I most needed. I would like to also thank my parents and my parents-in-law for all the love and support.

Hiranya Suriyaarachchi

July 2014

Summary

Sub-synchronous interaction in wind integrated power systems has been a popular area of research for the past few years. Ever since the incident in Texas in 2009, there has been a growing interest in sub-synchronous interactions between Type 3 wind power plants and series compensated transmission lines. Numerous research have been carried out in the past to study sub-synchronous interactions in such systems. However, there is a disagreement in the literature about the root cause of the sub-synchronous interaction between a Type 3 wind power plant and a series compensated transmission line. In some literature it has been claimed that the sub-synchronous interaction in such systems is due to self excitation and in some literature it has been claimed that it is due to sub-synchronous controller interaction.

This thesis presents a comprehensive procedure to study sub-synchronous interactions in wind integrated power systems effectively and efficiently. The proposed procedure involves a screening phase and a detailed analysis phase. The screening is performed using a frequency scan and the detailed analysis is performed using small signal stability analysis. To facilitate the small signal analysis, a detailed linearized model of a Type 3 wind power plant is presented in this thesis. The model presented includes the generator, a three-mass drive train model, rotor and grid side converter controller models, converter transformer model and a pitch controller model. To accurately capture the effects of sub-synchronous interactions, the ac network is modelled using dynamic phasors.

It is shown that by using the proposed procedure, the sub-synchronous interaction between a Type 3 wind power plant and a series compensated line is due to an electrical resonance between the wind power plant generator and the series capacitor. It is also shown that this interaction is highly controllable through the rotor side

converter current controllers. This fact is proven by studying the sub-synchronous interactions in a single machine power system as well as in multi machine power systems.

This thesis also presents a sub-synchronous interaction mitigation method using network devices. The performance of an SVC and a STATCOM is evaluated in this thesis. A small signal stability analysis based method is used to design a sub-synchronous damping controller. A method is presented to estimate the damping controller parameters systematically to obtain the desired performance using small signal stability analysis results.

Furthermore, it is shown that by strongly controlling the voltage of the point of common coupling, the damping of the oscillations produced by the sub-synchronous interaction between the wind power plant and the series compensated line can be improved.

Based on the findings of this research, the thesis proposes a number of recommendations to be adopted when studying the sub-synchronous interactions in wind integrated power systems. These recommendations will facilitate the completion of such studies effectively and pinpoint the root cause of the sub-synchronous interactions.

List of Principal Symbols

t	Time
ω_0	Fundamental angular frequency of power system
f_n	Network resonant frequency
T_m, T_e	Generator input mechanical torque and output electrical torque
H_b,H_h,H_g	Inertia constants of blades, hub and generator
ω_b,ω_h,ω_r	Speeds of blades, hub and generator
θ_{bh}, θ_{hg}	Angles between blades and hub, and hub and generator
K_1, K_2	Stiffness coefficients of the shafts connecting blades and hub, and hub and generator
Q_s, Q_g	Stator and grid side converter reactive power
K_{pQs}, K_{iQs}	Proportional and integral gain of the stator reactive power controller
$K_{p\omega r}$, $K_{i\omega r}$	Proportional and integral gain of the generator speed controller
K_{pdr}, K_{idr}	Proportional and integral gain of the RSC d axis current controller
K_{pqr}, K_{iqr}	Proportional and integral gain of the RSC q axis current controller
K_{pdc}, K_{idc}	Proportional and integral gain of the dc voltage controller
K_{pQg}, K_{iQg}	Proportional and integral gain of the GSC reactive power controller
K_{pdg}, K_{idg}	Proportional and integral gain of the GSC d axis current controller
K_{pqg}, K_{iqg}	Proportional and integral gain of the GSC q axis current controller
V_{dc}	DC capacitor voltage
C_{ser}	Series capacitor capacitance
X_{pcc}	PCC transformer inductance
R_l,L_l,C_l	Line resistance, inductance and capacitance
P_{pcc}	Active power injection at the PCC
I_{pcc}	Current flowing through the PCC transformer
V_R, V_I	Real and imaginary components of ac bus voltage
I_R, I_I	Real and imaginary components of ac current injected to a bus
$[A]$, $[B]$	System matrix and input matrix of a state space model
$[\Lambda]$	Eigenvalue matrix
λ	An eigenvalue
f, ζ	Frequency and damping ratio of an eigenvalue
$[\Phi]$, $[\Psi]$	Right and left eigenvector matrix
Φ_i, Ψ_i	Right and left eigenvectors of i^{th} eigenvalue
$p_k i$	Participation factor between k^{th} state and i^{th} mode
R_i	Residue of mode i

Table of Contents

List of Figures

List of Tables

Chapter 1

Introduction

For many years, demand for electricity was provided from traditional energy sources such as hydro, nuclear and fossil fuels. However at present, many countries have exploited most of the potential sources for hydro power, and fossil fuel reserves are fast diminishing. Also, electricity generation from fossil fuels and nuclear energy comes with a price for the environment. Therefore, in the future a major portion of the electricity demand needs to be provided from alternative energy sources. Renewable energy sources such as wind and solar are two attractive options, because they are clean and available abundantly. At present, wind power penetration in electric power systems is increasing rapidly. In year 2011, 40 GW of new wind generation was added [1] into power grids globally, which was the highest amount of wind generation added in a calender year. For the last two decades, China, the United States, Germany, Spain, and India share the largest representation of the world wide wind capacity, which amounts to 74% in 2011.[1]. The Strategic Energy Technology Plan [2] published by the European Commission sets a framework to accelerate the development of low carbon emission energy technologies so that by year 2020, 20% of Europe's energy comes from renewable sources. As part of this plan the European Wind Initiative aims to increase the wind penetration in Europe to 20% by 2020 and to 50% by 2050 [3]. A similar initiative in the United States has identified five Competitive Renewable Energy Zones (CREZ) in Texas which includes 11553 MW of new wind generation in the western part of the state [4].

1.1 Types of Wind Turbine-Generators

Considering the operation, wind turbine generators can be categorized as either fixed-speed or variable-speed wind turbine-generators. In fixed-speed wind turbine-generators the generator, which is either a squirrel cage or a wound rotor type, is directly connected to the ac network with the aid of a soft starter and a capacitor bank. In this type of wind turbine-generator, the unit is designed to operate optimally only for one rotor speed. Since the generator is directly coupled to the ac network, the torque fluctuations caused by the wind speed variations are transmitted to the network as power fluctuations. In case of weak networks, these power variations can lead to undesirable voltage fluctuations. Although the capacitor provides reactive power support, the reactive power consumption of a fixed-speed wind turbine can not be controlled. The main advantages of this type of wind turbine-generators are that they are simple, robust and inexpensive. On the other hand, the variable-speed wind turbine-generators can be operated optimally over a wide range of speeds. Also, the reactive power consumption can be controlled by means of the power electronic converter present in most variable-speed wind-turbine generators. However, controlling of variable-speed wind turbine-generators is complex and they are expensive when compared to the fixed-speed wind turbine-generators. Due to their merits, however, the variable-speed wind turbine-generators are the popular choice of wind turbine-generators nowadays.

By considering the speed controlling method as the criterion, wind turbine-generators are frequently classified into four configurations as shown in Figure 1.1 [5].

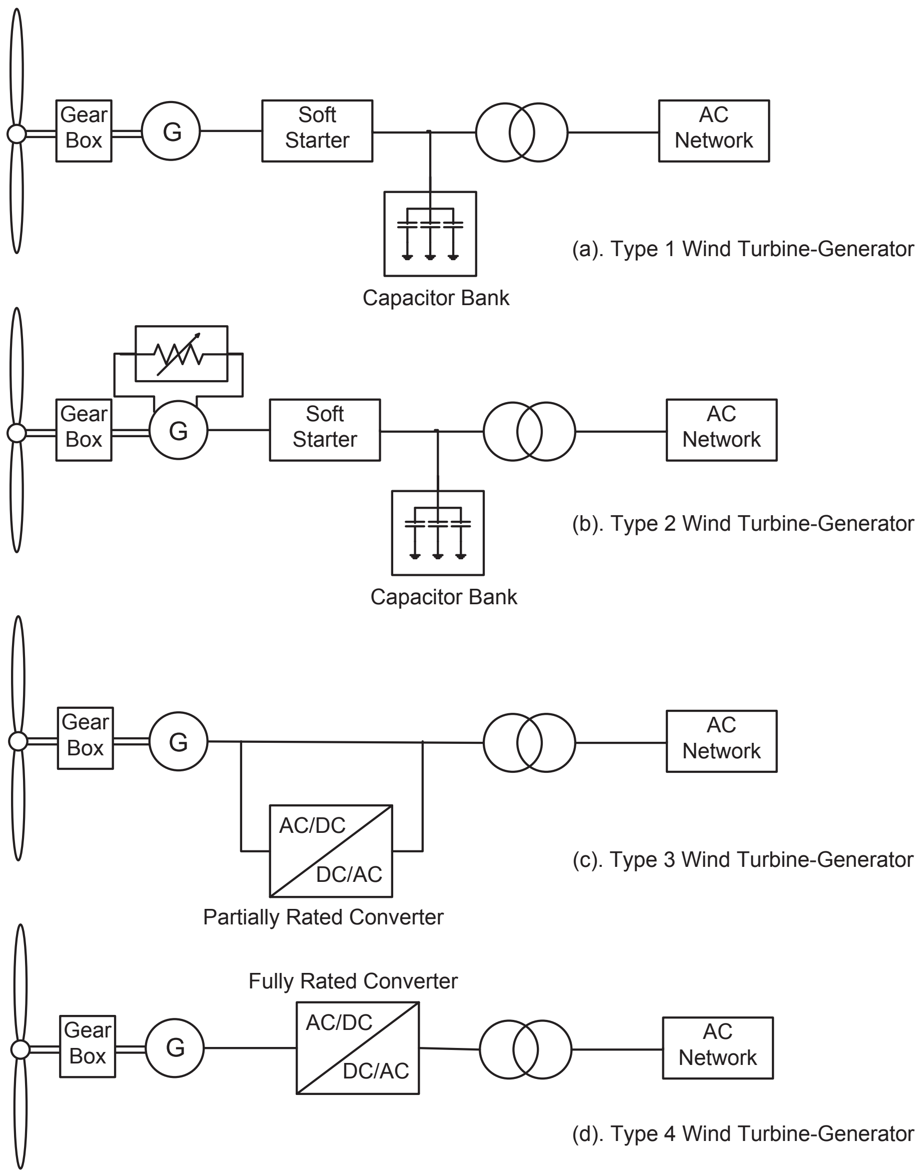

Figure 1.1: Wind turbine-generator configurations

Fixed-speed wind turbine-generators are classified as Type 1. Type 2 wind turbine-generators, which are also known as limited variable speed wind turbine-generators, use wound rotor induction generators. Since these generators are directly connected to the ac network as shown in Figure 1.1b, capacitor banks are used to limit the reactive power consumption from the ac network, similar to Type 1 wind turbine-generators. A limited speed control can be achieved by using the variable rotor resistor. The range of speed control depends on the size of the external rotor resistor, and typically a speed range of 0-10% above the synchronous speed can be achieved [5]. The wind turbine configuration shown in Figure 1.1c is classified as Type 3. These wind turbine-generators also use a wound rotor induction generator. The generator rotor is fed by a partially rated converter and hence they are also known as doubly-fed induction generators (DFIG). In this type of turbine-generator, the converter needs to be rated at only 1/3 of the rating of the generator [6]. Because of the additional controllability provided by the converter, the reactive power exchange with the ac network can be controlled precisely. The dynamic speed rage of the Type 3 wind turbine-generators depend on the size of the converter and typically a speed range of 70% to 130% of the synchronous speed is possible. Type 4 wind turbine-generators are connected to the ac network via a fully rated converter. Since the converter decouples the wind turbine from the ac network, the machine can be operated at any speed. In this configuration too, the reactive power exchange with the external network is controlled by the converter. Since the the converter is rated to the full rating of the wind turbine-generator, Type 4 wind units are expensive compared to Type 3 wind turbine-generators. Because of their reactive power controllability, Type 3 wind turbine-generators are widely used in new wind installations and Type 4 wind turbine-generators are mostly used in offshore wind power plants. The work presented in this thesis is focused on Type 3 wind turbine-generators.

Regardless of onshore or offshore, wind generation is often located in remote locations. Sometimes these locations are situated hundreds of kilometers away from the load centers. For example, the CREZ in west Texas is located about 400 miles away from the major load centers in east Texas. In such cases, the wind generation is connected to load centers by long series compensated ac transmission lines. Often due to economic reasons series compensation is achieved by installing series capacitors in long transmission lines. It has been known for many years that the series capacitors self-excite both synchronous and induction machines [7], but only after the two failures of the exciter shaft in one of the machines at the Mohave power plant in October 1971, the severity of the adverse effects of series capacitors on electrical machines came into the forefront of attention [8]. Since then extensive research has been performed to investigate the impact of series compensation on synchronous generators as well as on other devices such as HVdc converter terminals. Reference [4] reports an incident in which some generators in a wind power plant and the series capacitors sustained damages following a contingency. In this incident, the contingency made the wind power plant to become radial with a series compensated transmission line. Because of such incidents, it is important to understand the phenomena of sub-synchronous interactions in a wind integrated power system.

1.2 Sub-synchronous Resonance in Power Systems

A power system is a large combination of electrical and mechanical elements. The electrical system has many series and parallel combinations of inductive, capacitive, and resistive elements. Each series and parallel combination has a natural frequency. Therefore, the electrical system has many natural frequencies and typically they are well above the system operating frequency, which is either 60 or $50Hz$. Often, these higher frequency oscillations are well damped. Even if an under-damped oscillation is present, it can be easily filtered out. However, under certain conditions such as in the presence of series compensation, some of these natural frequencies can be below the nominal operating frequency. In such cases, they can interfere with the normal operation of the power system.

The IEEE working group on sub-synchronous resonance in power systems defines sub-synchronous resonance as "*a condition in the power system where the electrical system exchange a significant amount of power with the turbine-generator at one or more frequencies below the synchronous frequency*" [9]. Even a slight system disturbance can excite these inherent network resonances. In such an instance the electrical quantities in the system such as voltages and currents start to oscillate.

To understand this phenomenon mathematically, consider the simple example shown in Figure 1.2. It consists of a simple RLC circuit excited by a sinusoidal ac voltage source with the magnitude V_m and angular frequency ω_s.

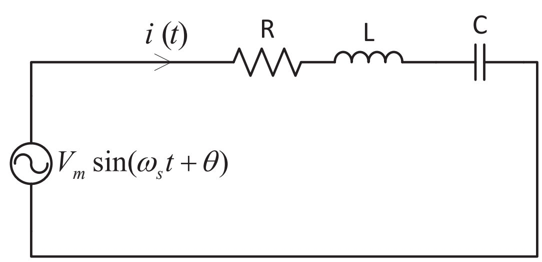

Figure 1.2: Simple RLC circuit

The impedance Z of the circuit in Laplace domain is given by

$$Z(s) = R + Ls + \frac{1}{Cs} \tag{1.1}$$

The Laplace transform of the voltage is,

$$V(s) = V_m \frac{s\sin\theta + \omega_s \cos\theta}{s^2 + \omega_s^2} \tag{1.2}$$

Therefore, the current flowing in the circuit $I(s)$ is easily obtained as,

$$I(s) = \frac{V(s)}{Z(s)} = \frac{\frac{sV(s)}{L}}{s^2 + \frac{R}{L}s + \frac{1}{LC}} \tag{1.3}$$

Equation (1.3) can be also expressed in the form,

$$I(s) = \frac{\frac{sV(s)}{L}}{s^2 + 2\zeta\omega_n s + \omega_n^2} \tag{1.4}$$

where,

$$\omega_n = \sqrt{\frac{1}{LC}}, \qquad \zeta = \frac{R}{2}\sqrt{\frac{C}{L}}$$

The terms ω_n and ζ in Equation (1.4) are known as the undamped natural frequency and the damping ratio, respectively.

Substituting from Equation (1.2) and taking the inverse Laplace transform, the current flowing through the circuit can be expressed in time domain in the following form [10]

$$i(t) = A\sin(\omega_s t + \psi_1) + Be^{-\zeta\omega_d t}\sin(\omega_d t + \psi_2) \tag{1.5}$$

The term ω_d is known as the damped natural frequency. It depends on the network parameters only and is given by,

$$\omega_d = \omega_n\sqrt{1-\zeta^2} = \frac{1}{2L}\sqrt{\frac{4L - R^2C}{C}} \tag{1.6}$$

From Equation (1.5) it is evident that the current flowing in the circuit consists of two terms: a sinusoidal term with the frequency of the driving voltage (ω_s) and a decaying sinusoidal component (transient) with the frequency (ω_d) determined by the network parameters. If the current given in Equation (1.5) is assumed to be of phase a of a three phase system. Then the currents for phases b and c will also have the two components present but with different coefficients for the transient components and different phase shifts for the sinusoidal part. Since power systems consist of a large combination of RLC components, the currents flowing in the power system consist of a large number of such transients.

To investigate the effect of the transient network currents on an electrical machine they need to be subjected to Park transform. It is a well known fact that the balanced sinusoidal currents produce dc currents in the d and q axis direction [10]. It can be shown that the Park transform of the transient current will produce many sine and cosine terms with the frequencies $\omega_s + \omega_d$ and $\omega_s - \omega_d$. The former is known as the super-synchronous frequency and the latter is known as the sub-synchronous frequency. Therefore, the transient network current will appear to the rotor as two components with the sub-synchronous frequency and super-frequency. Because of its high frequency, the super-synchronous currents normally have higher damping and hence do not pose a threat to the system stability. However, the sub-synchronous currents sometimes have low damping and hence can destabilize the power system. Therefore, the main focus of this thesis is on the sub-synchronous phenomena. Sub-synchronous phenomena in power systems are mainly divided into four categories, namely, induction generator effect, torsional interactions, torque amplification, and device dependent sub-synchronous oscillations [9] .

1.2.1 Induction Generator Effect

Exciting the network resonance frequencies induces sub-synchronous currents in the armature of the electrical machine. If a constant speed is assumed, the rotor of the synchronous machine is rotating at the synchronous speed, which is faster than the speed of the rotating magnetic field induced by the sub-synchronous armature current. Under these conditions, the synchronous machine can be considered as behaving similar to an induction machine with a negative slip. With the negative slip, the armature resistance when viewed from the rotor terminal is negative. If this negative resistance exceeds the total resistance of the network, the electrical system is self-excited. Self-excitation of electrical machines will make the current and voltage oscillations grow and eventually will lead to excessive currents and voltages that will damage the generator.

1.2.2 Torsional Interaction

A thermal generation unit consists of a number of steam turbines connected to the generator using a long shaft. Because of the presence of a number of masses, the mechanical system of a thermal generation unit has a number of natural frequencies. A system disturbance excites the natural modes in both electrical and mechanical systems. Thus the mechanical torque in the turbine-shaft system consists of its natural frequencies whereas the electromagnetic torque produced by the armature currents consist of the sub-synchronous frequency components corresponding to the network resonances. If the frequency of the induced sub-synchronous electromagnetic torque is close to one of the natural frequencies of the turbine-generator shaft system, the electrical system oscillations can help to sustain or grow the mechanical system oscillations and vice versa. This phenomena is known as torsional interaction.

1.2.3 Torque Amplification

Impact of the oscillations in the shaft system is twofold. Due to the torsional interactions there can be poorly damped or undamped oscillations in the shaft system. Even a small disturbance may be sufficient to excite these oscillations, which may take a long time to decay or may even grow with time. In both cases repeated exposure to such events may lead to shaft failure.

On the other hand, the oscillations produced by torsional interactions may be well damped. These oscillations may decay very quickly. However, in such cases the shaft torque can still be very high for few cycles following a large system disturbance such as a fault. The torque observed when the sub-synchronous electromagnetic torque frequency is closer to the one of the natural frequencies of the shaft system is higher than when they are not closer to each other. This amplification of torque is known as the torque amplification. Repeated exposure to torque amplification will significantly reduce the life of the shaft [11].

1.2.4 Device Dependent Sub-synchronous Oscillation

Sub-synchronous interactions are not limited to interactions between turbine-generators and series compensated lines. Other power system components such as HVdc converters [12], FACTS devices such as static var compensators [13], power system stabilizers, high speed governor controls, etc. may induce sub-synchronous oscillations. These devices use various controllers to obtain the desired performance. If the impact of these manipulations may be picked up by another controller in a different device, the two controllers can interact with each other. If these control actions oppose each other, it leads to an oscillatory behaviour.

It is worth to note that although sub-synchronous interactions were categorized into these groups they are not always mutually exclusive. When these categorizations were made [9]; the traditional generators were the main focus. Since then it has been found that the wind power plants are also vulnerable to sub-synchronous interactions in the presence of series compensated transmission lines.

1.3 Sub-synchronous Interaction Analysis Techniques

Several techniques are available to study sub-synchronous interactions (SSI) in power systems. The main objective of these techniques is to identify the potential conditions and locations that can create sub-synchronous interactions in various power system components. Once they are identified, the power system can be designed either to avoid such conditions, or to protect it from reaching undesirable operating conditions such as excessive voltages and currents resulting from sub-synchronous interactions. Also, these techniques will aid the design of appropriate mitigation measures. The next few sub-sections will introduce the sub-synchronous interaction analysis techniques that are presently being used.

1.3.1 Frequency Scanning

In frequency scanning, the presence of a network resonance is identified by calculating the driving point impedance over the entire sub-synchronous frequency spectrum. A sharp change in the impedance indicates a network resonance. The complementary frequency of the network resonance gives the resulting sub-synchronous interaction frequency. This is a widely used method to study sub-synchronous interactions in power systems with thermal generation. In such studies the synchronous generator is represented by its induction generator equivalent. However, there is no straight-forward method to convert the synchronous generator parameters to its induction generator equivalent. The induction generator equivalent parameters need to be obtained from the manufacturers. The reference [14] proposes a frequency scanning tool, which can be integrated with commercial transient stability tools. In this tool the synchronous generator is modeled as a voltage source behind the armature resistance and the sub-transient reactance. A comparison between four different frequency scanning methods is given in [15] and it has been shown that, the fast analytical methods are capable of producing accurate results as the electromagnetic transient simulation based methods. However, it was shown that the accuracy of the analytical methods depends on the level of the detail of the models used. Frequency scanning is mainly used as a screening technique. It is not straightforward to obtain the damping of the sub-synchronous oscillation using frequency scan results. However, methods have been developed to calculate the damping of the sub-synchronous oscillation [16], [17].

1.3.2 Small Signal Analysis

The small signal analysis of a dynamic system gives insight into the oscillatory behaviour of the system. The eigenvalues calculated from the linearized equations of the nonlinear system are used for the small signal analysis. Analysis of the eigenvalues reveals the frequency and damping of the oscillatory modes present in the system. Also, the eigenstructure information derived from the linearized system is used to obtain the participation factors and mode shapes, which are used to identify the root cause of the oscillations. Therefore, small signal analysis can be easily used to identify the type of sub-synchronous interaction present in the system [9],[10],[18],[19]. However, small signal analysis is not meant for time domain simulations as linearized models are only valid for small disturbances in the system. Therefore, large disturbance phenomena such as torque amplification cannot be studied using small signal analysis.

1.3.3 Electromagnetic Transient Simulations

Electromagnetic transient simulation uses detailed models that take into account the nonlinear characteristics of power system components [20]. Therefore, it gives the closest results to the actual behaviour of the power system. Therefore, electromagnetic transient simulation has been used to study sub-synchronous interactions in power systems [9],[10]. Dynamic behaviour of the system even under large system disturbances such as faults can be accurately studied using electromagnetic transient simulations. Hence, large signal phenomena such as torque amplification can be accurately studied using electromagnetic transient simulations. Since the output of an electromagnetic transient simulation is the time variation of various electrical and mechanical quantities in the system, identification of the root cause for the oscillatory problem of the system can be cumbersome.

1.3.4 Damping Torque Analysis

Damping torque analysis is mainly used to identify the potential sub-synchronous torsional interaction problems [21]. This method is mainly used when the mechanical shaft data are not readily available and the torsional oscillation frequencies are known. In this method, a small sinusoidal perturbation is added to the machine's speed reference and the corresponding change in electrical torque in phase with the speed is measured. This is used to estimate the inherent damping added by the electrical system at a particular torsional frequency. When performing the damping torque analysis the mechanical system needs to be decoupled from the electrical system.

1.4 Sub-synchronous Oscillations in Wind Power Plants

Since the vulnerability of the wind power plants to sub-synchronous interactions came to forefront, all aforementioned methods have been used to study sub-synchronous interactions in wind integrated power systems. In [22], sub-synchronous interaction between a wind power plant equipped with fixed speed induction generators and a series compensated line has been demonstrated using electromagnetic transient simulations. A small signal stability analysis is performed in [23] to analyze the sub-synchronous resonance between a Type 3 wind power plant and a series compensated transmission line. A more recent work [24] shows that the sub-synchronous resonance present in a variable speed system is mainly due to self-excitation rather than due to the torsional interactions. However, another recent publication claims, using time domain simulations, that the sub-synchronous interaction between Type 3 wind turbine-generators and series compensated transmission systems is due to controller interactions [25]. Such different conclusions calls for the need for more research to identify root cause and the type of sub-synchronous interaction present in wind integrated power systems.

Sub-synchronous interactions in the presence of traditional generation has been known for decades and the techniques described in the previous sub-sections are successfully being used to study them. In past few years, various researchers have used a number of these different tools to study the sub-synchronous interactions in wind integrated power systems. Although, those methods are capable in analyzing sub-synchronous interactions, they have their own limitations. For example, a frequency scan can only indicate the presence of a network resonance whereas electromagnetic transient simulations are cumbersome to identify the root cause of the sub-synchronous interaction. Also, electromagnetic transient simulations are time consuming and computationally heavy in case of large power systems. A systematic procedure will enable the user to identify the sub-synchronous interactions effectively and efficiently.

1.5 Sub-synchronous Interaction Mitigation

As described earlier in this chapter, current and voltage oscillations induced due to sub-synchronous interactions could cause physical damages to the power system equipment unless detected and mitigated promptly. A number of sub-synchronous interaction mitigation methods has been proposed in literature. Most of these methods are proposed to mitigate the sub-synchronous interactions between thermal generation and series compensated lines.

1.5.1 SSR Blocking Filters

SSR blocking filters are an effective means of mitigation of sub-synchronous torsional interactions in thermal generation systems. A filter with a high quality factor tuned to the torsional frequency is connected between the neutral point of the generator transformer and the ground [8], [26]. The filter introduces a positive resistance at the tuned frequency so that it improves damping. Also the filter impedance shifts the resonant frequency so that it is sufficiently away from the torsional frequency.

It has also been proposed to install SSR blocking filters at the series capacitor locations [27]. In this method the total impedance of the blocking filter and the series capacitor is less capacitive and more resistive at the problematic sub-synchronous frequency range.

1.5.2 Supplementary Excitation Damping Control (SEDC) and Relay Protection

A Supplementary excitation damping controller modulates exciter voltage reference signal at the torsional frequency. The torsional speed is used as the input to the SEDC [28],[26]. The SEDC improves the torsional damping by appropriately modulating the generator field voltage.

Protective relays are also used to trigger protective actions against the sub-synchronous resonance in power systems [26],[29]. The relays can use turbine-generators' shaft oscillations, current or voltage to detect the presence of sub-synchronous oscillations. The output signal provided by the relay is used to start the required corrective action such as tripping generators,lines or series capacitors.

1.5.3 Series Capacitor By-passing

The objective of this method is to reduce the level of series compensation so that the network resonant frequency is shifted away from the sub-synchronous torsional frequency of the turbine-generator unit. Reduction in compensation level is normally achieved by by-passing some of the capacitors in the series capacitor bank. The level of series compensation is selected to increase power transfer through the line. Therefore, reducing the compensation level will hamper this objective.

1.5.4 Using a Thyristor Controlled Series Capacitor (TCSC)

Sub-synchronous interaction problems in power systems are often caused by series capacitors. In this method the source of the problem is eliminated by replacing the series capacitor with a thyristor controlled series capacitor. In a TCSC the dynamic characteristics of the series capacitor at sub-synchronous frequencies is controlled by varying the firing angle of the thyristor. Performance tests carried on the Slatt TCSC in Oregon, USA using the nearby Boardman turbine-generating units has shown the effectiveness of TCSCs in sub-synchronous interaction mitigation [30].

1.5.5 Mitigation of SSI in Wind Integrated Power Systems

Some of the aforementioned mitigation techniques have also been applied to mitigate sub-synchronous interactions in wind integrated power systems. In [25] modifications to wind farm controllers were proposed to mitigate sub-synchronous interaction in Type 3 wind power plants. The proposed modifications include a reduction in rotor side converter controller gains and adding a supplementary damping controller to the rotor side converter controller. It has also been shown in the literature that a supplementary damping controller on the grid side converter controller is also capable of improving the damping of the sub-synchronous oscillations in Type 3 wind power plants [31]. However, modifications to the wind power plant controllers may be difficult to implement after the wind power plant is put into service.

A TCSC has been utilized to mitigate sub-synchronous interactions between a Type 1 wind power plant and a series capacitor [22]. Due to the remote location of the sites with wind power availability, there can be several series compensated lines in a wind integrated power system. The cost of replacing the series capacitors with TCSCs in such a system can be very high.

Series capacitor bypassing and tripping of wind power plant are two other mitigation methods. Reduction of series compensation level by bypassing some of the series capacitors reduces the power transfer capability of the transmission network. Also, the system will be deprived of a significant amount of generation if a large wind power plant is tripped to mitigate sub-synchronous oscillations. Therefore, both these methods might cause system stability problems and hence they may not be compatible with grid codes.

As mentioned previously in this chapter, transmission network expansions are needed due to the remote location of wind generation. In anticipation of large amounts of wind interconnection in the future, and to encourage the wind generation development, some system operators have taken an initiative to strengthen their transmission networks [4]. In these instances series compensation with series capacitors could be heavily used because of its economic benefits. Therefore, system operators need to ensure that interconnecting wind power plants does not create sub-synchronous interaction problems. The operators can setup interconnection requirements and guidelines and depend on wind developers to take required actions to avoid any sub-synchronous interaction issues.

If system operators can be more proactive and can ensure that their systems are immune to sub-synchronous interaction issues irrespective of the connecting wind power plant, the wind generation development can be independent of the transmission system development. This type of a global solution requires a network based sub-synchronous interaction mitigation method.

1.6 Thesis Objectives

The main objectives of this thesis are to

1. present a comprehensive analysis of the sub-synchronous interaction between a Type 3 wind power plant and a series compensated ac network to identify the cause and nature of the interaction.

2. propose a systematic procedure to effectively and efficiently identify the sub-synchronous interactions in a wind integrated power system.

3. propose recommendations on modeling and study requirements for sub-synchronous interaction analysis.

4. propose a network-based global solution to mitigate sub-synchronous interactions in wind integrated power systems.

1.7 Thesis Outline

The research reported in this thesis focuses on Type 3 wind power plants. The derivation of the linearized model of a Type 3 wind power plant is described in Chapter 2. It also describes the dynamic phasor representation of the ac network. The remainder of the thesis is organized as follows.

A validation of the linearized models derived in Chapter 2 is presented in Chapter 3. The time responses obtained with linearized models are compared with electromagnetic transient simulations obtained with PSCAD/EMTDC.

Chapter 4 presents the proposed sub-synchronous interaction study procedure. Using the proposed procedure a comprehensive analysis of the sub-synchronous interaction between a Type 3 wind power plant and a series compensated power system is presented. Also, the sensitivity of the sub-synchronous interaction to the wind power plant and network parameters is presented in Chapter 4.

The network based global sub-synchronous interaction mitigation method proposed in this thesis is presented in Chapter 5. This method utilizes either an SVC or a STATCOM to damp out the undesirable sub-synchronous oscillations. Small signal analysis results are used to design the damping controller. The performance of the proposed method will be verified using electromagnetic transient simulations.

The conclusions, contributions and suggestions for future work are presented in Chapter 6.

Chapter 2

Wind Integrated Power System Modelling

The modelling details of a wind integrated power system are presented in this chapter. This chapter describes the modelling of a Type 3 wind power plant, which is the main focus of this thesis.

2.1 Linearized Power System Models

The dynamic behaviour of a system may be expressed as a set of nonlinear differential equations as shown in Equation (2.1).

$$\dot{\mathbf{X}} = \mathbf{f}(\mathbf{X}, \mathbf{U}) \tag{2.1}$$

where,

$$\mathbf{X} = \begin{bmatrix} x_1 \\ x_2 \\ \vdots \\ x_n \end{bmatrix}, \qquad \mathbf{U} = \begin{bmatrix} u_1 \\ u_2 \\ \vdots \\ u_r \end{bmatrix}, \qquad \mathbf{f} = \begin{bmatrix} f_1 \\ f_2 \\ \vdots \\ f_n, \end{bmatrix}.$$

In Equation (2.1), $\mathbf{X}$ is a vector containing states x, $\mathbf{U}$ is a vector containing inputs u, n is the order of the system and r is the number of inputs. Note that $\mathbf{f}$ is independent of time. Such systems are called time invariant systems or autonomous systems. A system needs to be autonomous in order for it to be linearized. A power system for a given system configuration, and for a given operating condition can be expressed in the form shown in Equation (2.1). Therefore, a power system can be considered as an autonomous system.

When linearizing a nonlinear system, the nonlinear equations are linearized around an equilibrium point by expressing the nonlinear system using Taylor series and truncating after the first-order term. Therefore, in power systems the equilibrium point is selected as a steady state operating point obtained by solving power flow equations. At this equilibrium point, the time derivatives of states are zero and hence, Equation (2.1) can be written as,

$$\dot{\mathbf{X}}_0 = \mathbf{f}(\mathbf{X}_0, \mathbf{U}_0) = 0 \tag{2.2}$$

For a small perturbation around the steady state point, the states and inputs will become,

$$\mathbf{X} = \mathbf{X}_0 + \mathbf{\Delta X} \qquad \mathbf{U} = \mathbf{U}_0 + \mathbf{\Delta U}$$

Then, Equation (2.1) can be written as,

$$\dot{\mathbf{X}}_{\mathbf{0}} + \mathbf{\Delta}\dot{\mathbf{X}} = \mathbf{f}(\mathbf{X}_0 + \Delta\mathbf{X}, \mathbf{U}_0 + \Delta\mathbf{U}) \tag{2.3}$$

Expanding above equation in Taylor series with second and higher order terms neglected and substituting from Equation (2.2) yields,

$$\dot{\mathbf{X}} = \mathbf{A}\mathbf{\Delta}\mathbf{X} + \mathbf{B}\mathbf{\Delta}\mathbf{U} \tag{2.4}$$

where **A** is known as the state or plant matrix and **B** is known as the control or input matrix. The state space representation of the power system given in Equation (2.4) is the basis for its small signal stability analysis. Further details on the theory behind small signal stability analysis is given in [32].

2.2 Wind Power Plant Modeling

A schematic diagram of a Type 3 wind power plant is shown in Figure 2.1. The wind turbine-generator unit consists of a wind turbine connected to a doubly-fed induction generator (DFIG) via a shaft and a gear box. The rotor winding is connected to the external grid through a back to back voltage source converter unit and a transformer. The converter, whose ac side is connected to the rotor is commonly referred as the rotor side converter (RSC). The converter connected to the external grid via the transformer is known as the grid side converter (GSC). The RSC controls the DFIG so that it extract the maximum extractable wind energy while maintaining the system reactive power requirements. The function of the GSC is to maintain the dc link voltage while operating at unity power factor. The transformer filters out the harmonics produced by the grid side converter. In this section the modeling details of these components are discussed.

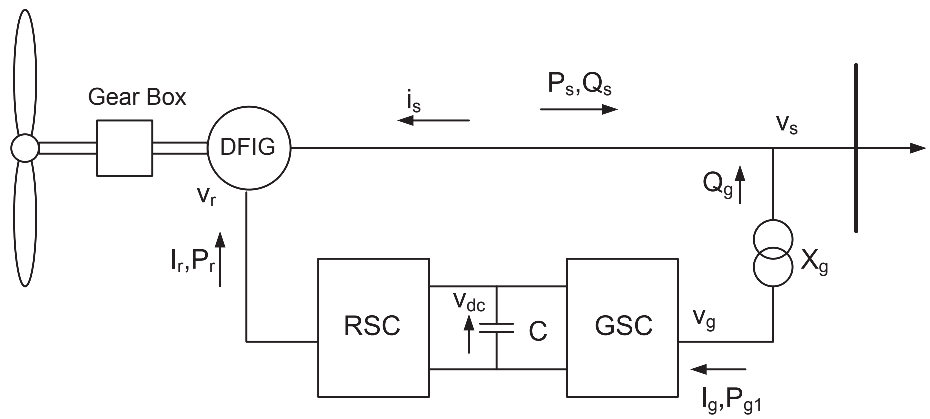

Figure 2.1: Schematic diagram of a Type 3 wind power plant

2.2.1 Wind Turbine Model

The power extracted from wind by a wind turbine is given by,

$$P_t = 0.5\pi\rho R^2 C_p(\lambda, \beta) v_w^3 \tag{2.5}$$

where, ρ is the air density [kg/m^3]; R is the turbine blade length [m]; C_p is the performance coefficient; and v_w is the wind velocity [m/s]. The performance coefficient is a function of tip speed ratio (TSR), λ, and pitch angle, β. The maximum theoretical value of the performance coefficient is 59.3%. This value is known as the Betz limit. However, commercial wind turbines typically have C_p in the range of $20-45\%$ [33]. The tip speed ratio is defined as the ratio between the turbine blade tip speed and the wind speed. Various empirical formulae are given in the literature to represent the performance coefficient. In [34], the generic equation

$$
\begin{aligned}
C_p(\lambda, \beta) &= c_1\left(\frac{c_2}{\alpha} - c_3\beta - c_4\right)\exp\left(\frac{-c_5}{\alpha}\right) + c_6\lambda \\
\text{with } \frac{1}{\alpha} &= \frac{1}{\lambda + 0.08\beta} - \frac{0.035}{\beta^3 + 1}
\end{aligned}
\tag{2.6}
$$

is used to model the performance coefficient. The coefficients c_1 to c_6 are: $c_1 = 0.5176$, $c_2 = 116$, $c_3 = 0.4$, $c_4 = 5$, $c_5 = 21$ and $c_6 = 0.0068$. The variation of C_p versus the tip speed ratio for several pitch angles is shown in Figure 2.2.

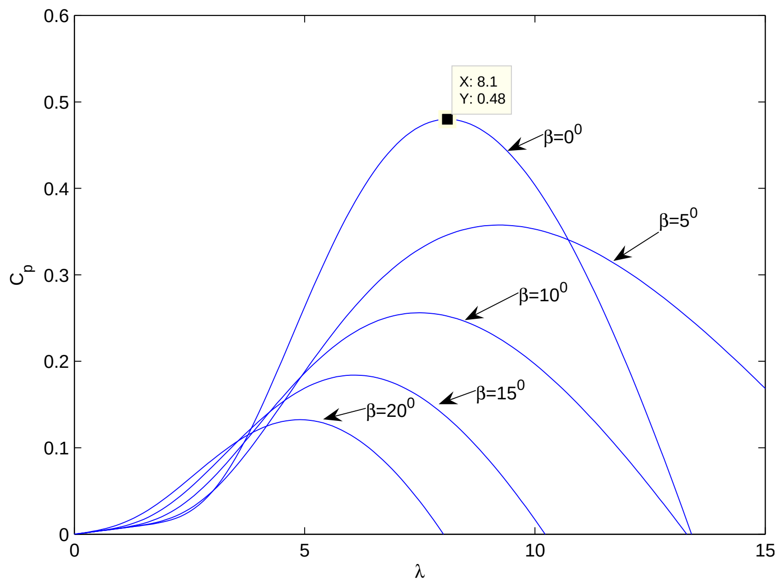

Figure 2.2: $C_p - \lambda$ characteristics

As shown in the figure, each pitch angle has an optimum value of λ where C_p is maximum. For example, for a zero degree pitch angle, the performance coefficient is maximum when $\lambda = 8.1$. From Equation (2.5) it can be seen that if the wind turbine is operated at this optimum tip speed ratio, the power extracted from the wind is maximum for a given wind speed. Therefore, often wind turbines are operated at this optimum tip speed ratio. This operating mode is commonly referred to as maximum power tracking mode. A typical wind turbine characteristic is shown in Figure 2.3. As the wind speed changes, the generator speed (i.e. turbine rotation speed) is changed by the speed controller in order to keep the TSR at its optimum value.

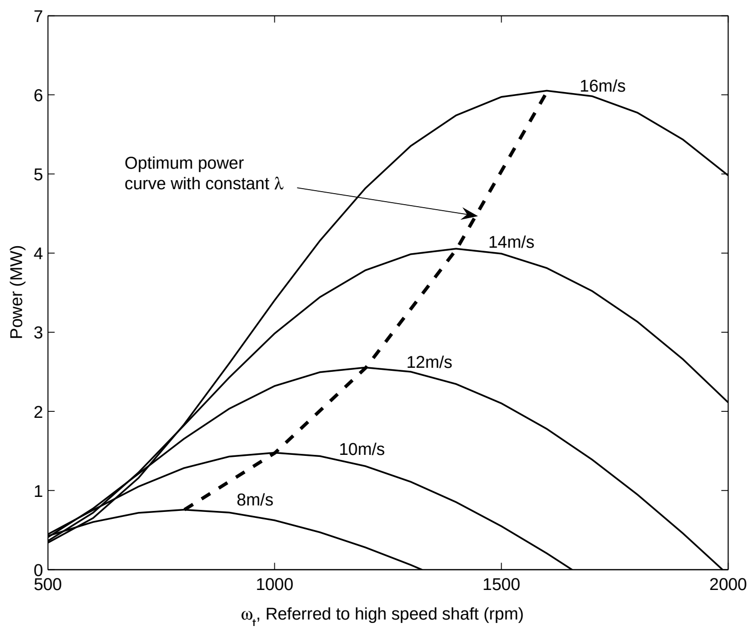

Figure 2.3: Wind turbine characteristics with $\beta = 0$

The wind speed at which the turbine is extracting its rated power is called the rated wind speed. If the wind speed increases beyond the rated speed, the machine is forced out of the optimal TSR operation. In such a case the pitch controller changes the pitch angle of the turbine blades so that the power extracted by the wind turbine is limited to the rated power. If ω_r is the generator rotor speed in per unit, ω_0 is the base angular speed and $N_g(> 1)$ is the gear ratio between the generator and the wind turbine, the TSR can be written as,

$$\lambda = \frac{R\omega_0\omega_r}{N_g v_w}. \tag{2.7}$$

For maximum power tracking operation, the relationship between the wind speed and the rotor speed can be obtained using Equation (2.7) as,

$$v_w = K_t \omega_r \tag{2.8}$$

where, $K_t = \dfrac{R\omega_0}{\lambda N_g}$.

If ω_t is the turbine speed, the mechanical torque T_m is given by, $T_m = P_t/\omega_t$. In per unit, $\omega_t = \omega_r$. Therefore, the mechanical torque input to the generator in per unit is given by,

$$T_m = \frac{P_t}{\omega_r} \tag{2.9}$$

Since the pitch controller is not active in maximum power tracking operation, the pitch angle is kept at a fixed value. Therefore, in such a case the performance coefficient is constant. Using Equations (2.5) and (2.9), the generator mechanical torque in maximum power tracking mode can be written as,

$$T_m = \frac{0.5\pi\rho R^2 C_p v_w^3}{\omega_r} \tag{2.10}$$

Linearizing Equation (2.10) yields,

$$\Delta T_m = \frac{1.5\pi\rho R^2 C_p v_{w0}^2}{\omega_{r0}} \Delta v_w - \frac{0.5\pi\rho R^2 C_p v_{w0}^3}{\omega_{r0}^2} \Delta\omega_r \tag{2.11}$$

Note that in the above equation as well as in equations through out this thesis, the subscript 0 denotes a steady state value.

2.2.2 Drive Train Model

The drive train model represents wind farm's main mechanical dynamics. There are various models of varying degrees of complexity available in the literature for drive train modeling. One-mass [35], [36], [37], two-mass [22], [24], [38] and three-mass [33], [39], [40] are the most common models used in previous works.

The one-mass model assumes generator inertia, the turbine hub and blades as a single lumped mass. Although simple, this model is not capable of showing torsional oscillations in the wind power plant. In the two-mass model, the wind turbine and the generator are modeled as two masses connected via a flexible shaft. The torsional oscillation between the wind turbine and the generator is observable with this model. The three-mass model has been derived so that the blade oscillations can be observed in studies. In this model the flexible portion of the blade is considered as one mass, the rigid part of the blades and turbine hub as another mass and the generator as the third mass. These three masses are connected with each other via two flexible shafts as shown in Figure 2.4.

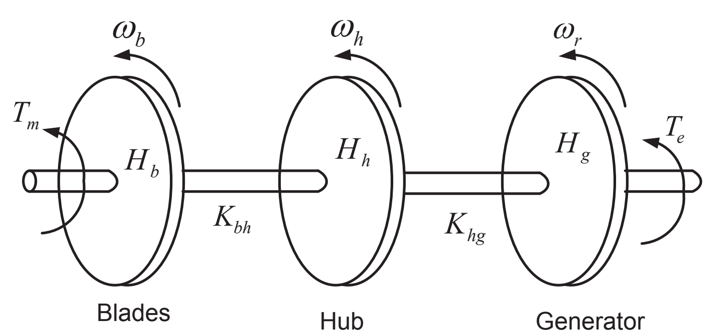

Figure 2.4: Three mass drive train model

In this research, the fifth order model in [39] is used to model the three-mass drive train. Note that the three-mass model used in this thesis neglects the mechanical damping of the system as this represents the worst case scenario. The mechanical damping is neglected to consider the worst case damping. If, H_b, H_h, and H_g are inertia constants (in seconds) of the masses representing the blades, the hub, and the generator, K_1 is the stiffness coefficient (in pu torque/electrical radian) of the shaft connecting the blade and the hub, K_2 is the stiffness coefficient (in pu torque/electrical radian) of the shaft connecting the hub and the generator, ω_b, ω_h are the pu rotating speeds of blades and the hub, θ_{bh}, θ_{hg} are the angles between the blades and the hub and between the hub and the generator, the dynamic model of the three-mass drive train model can be written as,

$$\begin{aligned}
\dot{\omega}_b &= \frac{1}{2H_b}(T_m - K_1\theta_{bh}) \\
\dot{\omega}_h &= \frac{1}{2H_h}(K_1\theta_{bh} - K_2\theta_{hg}) \\
\dot{\omega}_g &= \frac{1}{2H_g}(K_2\theta_{hg} - T_e) \\
\dot{\theta}_{bh} &= \omega_0(\omega_b - \omega_h) \\
\dot{\theta}_{hg} &= \omega_0(\omega_h - \omega_r)
\end{aligned} \tag{2.12}$$

In Equation (2.12), T_e represents the electromagnetic torque produced by the generator. The linearized model of the drive train is given in Equation (2.13). It is obtained by linearizing Equation (2.12) and substituting for T_m from Equation (2.11).

$$\Delta\dot{\mathbf{X}}_{3M} = \mathbf{A}_{3M}\Delta\mathbf{X}_{3M} + \mathbf{B}_{3M}\Delta\mathbf{U}_{3M} \tag{2.13}$$

where,

$$\begin{aligned}
\Delta\mathbf{X}_{3M} &= [\Delta\omega_b, \Delta\omega_h, \Delta\omega_r, \Delta\theta_{bh}, \Delta\theta_{hg}]^T \\
\Delta\mathbf{U}_{3M} &= [\Delta v_w, \Delta T_e]^T \\
\mathbf{A}_{3M} &= \begin{bmatrix} 0 & 0 & -\frac{\pi\rho R^2 C_p v_{w0}^3}{4H_b\omega_{r0}^2} & -\frac{K1}{2H_b} & 0 \\ 0 & 0 & 0 & \frac{K1}{2H_h} & -\frac{K2}{2H_h} \\ 0 & 0 & 0 & 0 & \frac{K2}{2H_g} \\ \omega_0 & -\omega_0 & 0 & 0 & 0 \\ 0 & \omega_0 & -\omega_0 & 0 & 0 \end{bmatrix} \\
\mathbf{B}_{3M} &= \begin{bmatrix} \frac{3\pi\rho R^2 C_p v_{w0}^2}{4H_b\omega_{r0}} & 0 \\ 0 & 0 \\ 0 & -\frac{1}{2H_g} \\ 0 & 0 \\ 0 & 0 \end{bmatrix}
\end{aligned}$$

2.2.3 Generator Model

The stator and rotor windings of the induction generator are represented by two sets of fictitious coils placed on a rotating orthogonal two axis frame R-I. The frame is rotating at synchronous speed. The following convention is used when developing the generalized machine model.

1. The stator and rotor currents are considered to be positive when flowing into the machine. i.e. motor convention.

2. The imaginary axis (I) is leading the real (R) axis.

3. The machine is modeled in the common reference frame where the real axis is

along the reference voltage vector.

In this research, the linearized model of the nonlinear wound rotor induction generator given in [35] is used. The nonlinear stator and rotor differential equations in per unit are written as,

$$\begin{aligned}
\dot{\psi}_{Rs} &= \omega_0(\omega_s\psi_{Is} - R_sI_{Rs} + V_{Rs}) && (2.14)\\
\dot{\psi}_{Is} &= \omega_0(-\omega_s\psi_{Rs} - R_sI_{Is} + V_{Is}) && (2.15)\\
\dot{\psi}_{Rr} &= \omega_0[(\omega_s - \omega_r)\psi_{Ir} - R_rI_{Rr} + V_{Rr}] && (2.16)\\
\dot{\psi}_{Ir} &= \omega_0[-(\omega_s - \omega_r)\psi_{Rr} - R_rI_{Ir} + V_{Ir}] && (2.17)
\end{aligned}$$

where, R_s and R_r are the stator winding resistance and rotor winding resistance referred to the stator, respectively, and ω_0 is the base angular speed. In Equations (2.7-2.10) and in the equations to follow, the subscripts in voltages (V), currents (I) and flux (ψ) denote the axis and the circuit (stator s or rotor r) that they belongs to. For example, V_{Rs} denotes the R axis stator voltage.

The R and I axis stator and rotor flux (ψ_{Rs}, ψ_{Is} and ψ_{Rr}, ψ_{Ir}) can be expressed in terms of the R and I axis stator and rotor currents (I_{Rs}, I_{Is} and I_{Rr}, I_{Ir}) as,

$$\begin{aligned}
\psi_{Rs} &= L_{ss}I_{Rs} + L_mI_{Rr} && (2.18)\\
\psi_{Is} &= L_{ss}I_{Is} + L_mI_{Ir} && (2.19)\\
\psi_{Rr} &= L_mI_{Rs} + L_{rr}I_{Rr} && (2.20)\\
\psi_{Ir} &= L_mI_{Is} + L_{rr}I_{Ir} && (2.21)
\end{aligned}$$

where, $L_{ss} = L_s + L_m$ and $L_{rr} = L_r + L_m$ with L_m, L_s and L_r are magnetizing inductance, stator winding inductance, and rotor winding inductance referred to stator, respectively.

Linearizing Equations (2.14) - (2.21) and substituting for currents from Equations (2.18) - (2.21) results in the small signal model of the generator as,

$$\Delta\dot{\mathbf{X}}_g = \mathbf{A}_g\Delta\mathbf{X}_g + \mathbf{B}_g\Delta\mathbf{U}_g + \mathbf{E}_g\Delta\mathbf{V} \tag{2.22}$$

where,

$$\begin{aligned}
\Delta\mathbf{X}_g &= [\Delta\psi_{Rs}, \Delta\psi_{Is}, \Delta\psi_{Rr}, \Delta\psi_{Ir}]^T \\
\Delta\mathbf{U}_g &= [\Delta\omega_r, \Delta V_{Rr}, \Delta V_{Ir}]^T \\
\Delta\mathbf{V} &= [\Delta V_{Rs}, \Delta V_{Is}]^T \\
\mathbf{A}_g &= \begin{bmatrix} -\frac{\omega_0 R_s L_{rr}}{\sigma} & \omega_0\omega_s & \frac{\omega_0 R_s L_m}{\sigma} & 0 \\ -\omega_0\omega_s & -\frac{\omega_0 R_s L_{rr}}{\sigma} & 0 & \frac{\omega_0 R_s L_m}{\sigma} \\ -\frac{\omega_0 R_r L_m}{\sigma} & 0 & \frac{\omega_0 R_r L_{ss}}{\sigma} & \omega_0\omega_s \\ 0 & -\frac{\omega_0 R_r L_m}{\sigma} & -\omega_0\omega_s & \frac{\omega_0 R_r L_{ss}}{\sigma} \end{bmatrix} \\
\mathbf{B}_g &= \begin{bmatrix} 0 & 0 & 0 \\ 0 & 0 & 0 \\ -\omega_0\psi_{Ir} & \omega_0 & 0 \\ \omega_0\psi_{Rr} & \omega_0 & \end{bmatrix} \\
\mathbf{E}_g &= \begin{bmatrix} \omega_0 & 0 \\ 0 & \omega_0 \\ 0 & 0 \\ 0 & 0 \end{bmatrix}
\end{aligned}$$

with, $\sigma = L_{rr}L_{ss} - L_m^2$.

The electromagnetic torque produced by the generator can be written as

$$T_e = \psi_{Ir} I_{Rr} - \psi_{Rr} I_{Ir} \tag{2.23}$$

Substituting the current terms in the above equation using Equations (2.16-2.19), the electromagnetic torque can be expressed using only the generator states as,

$$T_e = \frac{L_m}{\sigma}(\psi_{Is}\psi_{Rr} - \psi_{Rs}\psi_{Ir}) \tag{2.24}$$

Therefore, the linearized model of the electromagnetic torque is,

$$\Delta T_e = \mathbf{C}_T \Delta \mathbf{X}_g \tag{2.25}$$

where,

$$\mathbf{C}_T = \begin{bmatrix} -\frac{L_m \psi_{Ir0}}{\sigma} & \frac{L_m \psi_{Rr0}}{\sigma} & \frac{L_m \psi_{Is0}}{\sigma} & -\frac{L_m \psi_{Rs0}}{\sigma} \end{bmatrix}$$

Equation (2.25) is used to combine the drive train model with the generator model. When combining it is important to note that the drive train model is expressed as a generator whereas the generator is modelled as a motor.

2.2.4 Rotor and Grid Side Converter Models

Both rotor side converter and the grid side converter are pulse width modulated (PWM) voltage source converters. Their power electronic switches are switched at a very rapid rate, typically about 1-3kHz, well above the synchronous frequency. Because of their higher frequency, these switching transients can be easily filtered out from the system. The converter transformer inductance and point of common coupling transformer inductances block these high frequency switching transients.

Therefore, their impact on the power system beyond the point of common coupling is negligible. Furthermore, PWM switching frequencies are well above the frequency range of interest. Therefore, power electronic device switching is not modeled.

Using Equation (2.23) and Equations (2.18-2.21), the electromagnetic torque produced by the generator can be expressed in terms of the R-I components of the stator flux and rotor currents as

$$T_e = \frac{L_m}{L_s}(\psi_{Is} I_{Rr} - \psi_{Rs} I_{Ir}) \tag{2.26}$$

If $\psi_{Is} = 0$ in Equation (2.26), the electromagnetic torque depends only on ψ_{Rs} and I_{Ir}. In such a case I_{Ir} can be used to control the electromagnetic torque produced by the machine. Since the mechanical torque is inversely proportional to the turbine speed and the electromagnetic torque is equal to the mechanical torque at steady state, controlling I_{Ir} when $\psi_{Is} = 0$ enables the speed control of the doubly-fed induction generator. Therefore, the rotor side converter is controlled in a rotating frame where its direct axis (D-axis) is along the direction of the stator flux and its quadrature axis (Q-axis) is leading the direct axis. With this selection of the rotating frame $\psi_{Is} = 0$ condition is always satisfied. The relationship between the two reference frames will be given in sub-section 2.2.7.

The reactive power injected by the stator can be expressed in stator flux reference frame as,

$$Q_s = -(V_{Qs} I_{Ds} - V_{Ds} I_{Qs}) \tag{2.27}$$

Under most operating conditions the generator terminal voltage and the stator flux are almost orthogonal to each other. Therefore, $V_{Ds} \approx 0$ and

$$Q_s = -V_{Qs} I_{Ds} \tag{2.28}$$

Substituting I_{Ds} using Equation (2.16) expressed in D-Q frame gives

$$Q_s = -\frac{V_{Qs}}{L_{ss}}(\psi_{Ds} - L_m I_{Dr}) \tag{2.29}$$

Equation (2.29) implies that stator reactive power is controllable through I_{Dr}. Therefore, the rotor side converter controllers are designed such that its direct axis controller controls the stator reactive power whereas its quadrature axis controller controls the rotor speed.

Normally a cascaded controller i.e. a controller with a slower outer loop determining the reference values for the fast inner loop controller is used for the converter controllers in Type 3 wind power plants [41]. The main advantage of using the cascaded control is that it facilitates independent control of active and reactive power. The rotor side converter controller used in this research is shown in Figure 2.5.

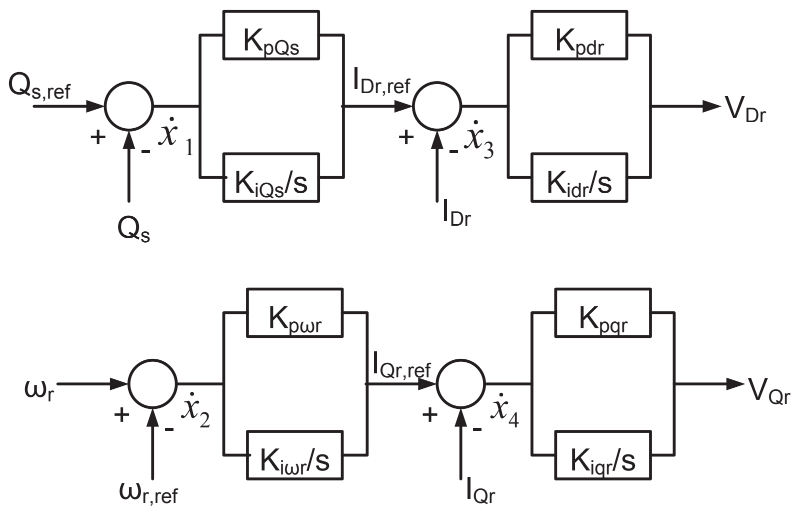

Figure 2.5: Rotor side converter controller

The faster inner-loop current controller regulates the direct and quadrature axis rotor currents according to the reference signals produced by the slower outer-loop reactive power and speed controllers. The rotor side converter controller is represented by the following differential and algebraic equations.

$$\begin{aligned}
\dot{x}_1 &= Q_{s,ref} - Q_s \\
\dot{x}_2 &= \omega_r - \omega_{ref} \\
\dot{x}_3 &= I_{Dr,ref} - I_{Dr} \\
\dot{x}_4 &= I_{Qr,ref} - I_{Qr}
\end{aligned} \tag{2.30}$$

$$
\begin{aligned}
I_{Dr,ref} &= K_{pQs} * (Q_{s,ref} - Q_s) + K_{iQs} x_1 \\
I_{Qr,ref} &= K_{p\omega r} * (\omega_r - \omega_{ref}) + K_{i\omega r} x_2 \\
V_{Dr} &= K_{pdr}(I_{Dr,ref} - I_{Dr}) + K_{idr} x_3 \\
V_{Qr} &= K_{pqr}(I_{Qr,ref} - I_{Qr}) + K_{iqr} x_4
\end{aligned} \tag{2.31}
$$

Note that for maximum power tracking operation, ω_{ref} can be derived from Equation (2.8) such that

$$
\omega_{ref} = \frac{v_w}{K_t} \tag{2.32}
$$

The state space model of the rotor side converter controller can be obtained by linearizing Equations (2.30) and (2.31) and expressing stator reactive power in $R-I$ frame as,

$$
\Delta \dot{\mathbf{X}}_{cr} = \mathbf{A}_{cr} \Delta \mathbf{X}_{cr} + \mathbf{B}_{cr} \Delta \mathbf{U}_{cr} + \mathbf{E}_{cr} \Delta \mathbf{V} \tag{2.33}
$$

$$
\Delta \mathbf{Y}_{cr} = \mathbf{C}_{cr} \Delta \mathbf{X}_{cr} + \mathbf{D}_{cr} \Delta \mathbf{U}_{cr} + \mathbf{F}_{cr} \Delta \mathbf{V} \tag{2.34}
$$

where,

$$
\begin{aligned}
\Delta \mathbf{X}_{cr} &= [\Delta x_1, \Delta x_2, \Delta x_3, \Delta x_4]^T \\
\Delta \mathbf{U}_{cr} &= [\Delta v_w, \Delta Q_{s,ref}, \Delta I_{Dr}, \Delta I_{Qr}, \Delta \psi_{Rs}, \Delta \psi_{Is}, \Delta \psi_{Rr}, \Delta \psi_{Ir}, \Delta \omega_r]^T \\
\Delta \mathbf{Y}_{cr} &= [\Delta V_{Dr}, \Delta V_{Qr}]^T
\end{aligned}
$$

$$\mathbf{A}_{cr} = \begin{bmatrix} 0 & 0 & 0 & 0 \\ 0 & 0 & 0 & 0 \\ K_{iQs} & 0 & 0 & 0 \\ 0 & K_{i\omega r} & 0 & 0 \end{bmatrix}$$

$$\mathbf{B}_{cr} = \begin{bmatrix} 0 & b_{12} & 0 & 0 & b_{15} & b_{16} & b_{17} & b_{18} & 0 \\ b_{21} & 0 & 0 & 0 & 0 & 0 & 0 & 0 & b_{29} \\ 0 & K_{pQs}b_{12} & -1 & 0 & K_{pQs}b_{15} & K_{pQs}b_{16} & K_{pQs}b_{17} & K_{pQs}b_{18} & 0 \\ K_{p\omega r}b_{21} & 0 & 0 & -1 & 0 & 0 & 0 & 0 & K_{p\omega r}b_{29} \end{bmatrix}$$

$$\mathbf{E}_{cr} = \begin{bmatrix} e_{11} & e_{11} \\ 0 & 0 \\ K_{pQs}e_{11} & K_{pQs}e_{11} \\ 0 & 0 \end{bmatrix}$$

$$\mathbf{C}_{cr} = \begin{bmatrix} K_{pdr}K_{iQs} & 0 & K_{idr} & 0 \\ 0 & K_{pqr}K_{i\omega r} & 0 & K_{iqr} \end{bmatrix}$$

$$\mathbf{D}_{cr} = \begin{bmatrix} d_{11} & d_{12} & d_{13} & d_{14} & d_{15} & d_{16} & d_{17} & d_{18} & d_{19} \\ d_{21} & d_{22} & d_{23} & d_{24} & d_{25} & d_{26} & d_{27} & d_{28} & d_{29} \end{bmatrix}$$

$$\mathbf{F}_{cr} = \begin{bmatrix} K_{pdr}e_{31} & K_{pdr}e_{32} \\ 0 & 0 \end{bmatrix}$$

with,

$$b_{12} = 1, \qquad b_{15} = \frac{L_{rr}V_{Is0}}{\sigma}, \quad b_{16} = -\frac{L_{rr}V_{Rs0}}{\sigma}, \quad b_{17} = -\frac{L_{m}V_{Is0}}{\sigma}, \quad b_{18} = \frac{L_{m}V_{Rs0}}{\sigma}$$

$$b_{21} = -\frac{1}{K_t}, \quad b_{29} = 1,$$

$$e_{11} = -\frac{L_{rr}\psi_{Is0} - L_m\psi_{Ir0}}{\sigma}, \qquad e_{12} = \frac{L_{rr}\psi_{Rs0} - L_m\psi_{Rr0}}{\sigma}$$

$$d_{1i} = K_{pdr}b_{3i}, \qquad d_{2i} = K_{pqr}b_{4i} \qquad i = 1, 2, \ldots, 9$$

The control concept for the grid side converter is similar to the rotor side converter except the fact that it is controlled in the terminal voltage reference frame. The direct axis (d axis) of this reference frame is selected to be along the terminal voltage vector while its quadrature axis (q axis) is leading the direct axis. Since $Q_g = v_{ds}I_{qg}$ in the terminal voltage reference frame, the quadrature axis grid side converter current can be used to control the reactive power injection (Q_g) by the grid side converter. The direct axis component of the grid side converter current is used to control the dc capacitor voltage (V_{dc}) [41]. As in the rotor side converter, the grid side converter controller shown in Figure 2.6 also is a cascaded controller and consists of a faster inner loop and a slower outer loop.

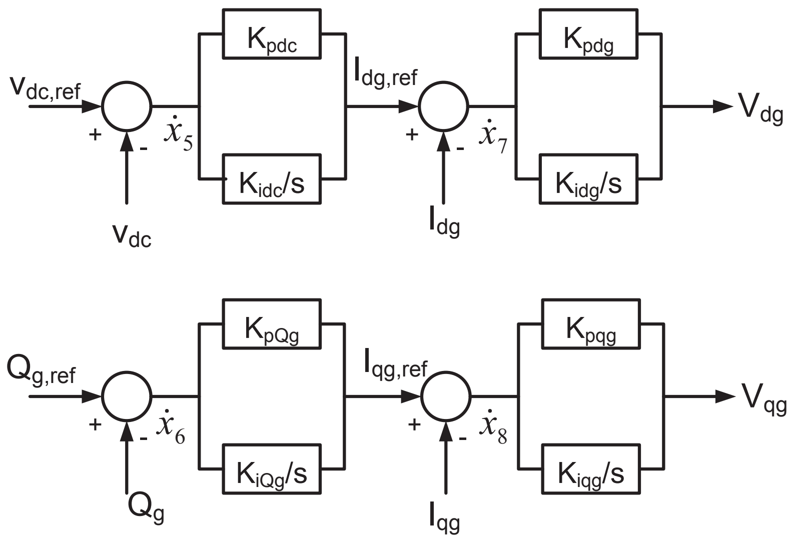

Figure 2.6: Grid side converter controller

The grid side converter controller is represented by the following differential and algebraic equations.

$$
\begin{aligned}
\dot{x}_5 &= V_{dc,ref} - V_{dc} \\
\dot{x}_6 &= Q_{g,ref} - Q_g \\
\dot{x}_7 &= I_{dg,ref} - I_{dg} \\
\dot{x}_8 &= I_{qg,ref} - I_{qg}
\end{aligned}
\tag{2.35}
$$

$$
\begin{aligned}
I_{dg,ref} &= K_{pdc} * (V_{dc,ref} - V_{dc}) + K_{idc} x_5 \\
I_{qg,ref} &= K_{pQg} * (Q_{g,ref} - Q_g) + K_{iQg} x_6 \\
V_{dg} &= K_{pdg}(I_{dg,ref} - I_{dg}) + K_{idg} x_7 \\
V_{qg} &= K_{pqg}(I_{qg,ref} - I_{qg}) + K_{iqg} x_8
\end{aligned}
\tag{2.36}
$$

As in the case of the rotor side converter controller, the grid side converter controller can be expressed in state space form as,

$$\Delta\dot{\mathbf{X}}_{cg} = \mathbf{A}_{cg}\Delta\mathbf{X}_{cg} + \mathbf{B}_{cg}\Delta\mathbf{U}_{cg} \tag{2.37}$$

$$\Delta\mathbf{Y}_{cg} = \mathbf{C}_{cg}\Delta\mathbf{X}_{cg} + \mathbf{D}_{cg}\Delta\mathbf{U}_{cg} \tag{2.38}$$

where,

$$\begin{aligned}
\Delta\mathbf{X}_{cg} &= [\Delta x_5, \Delta x_6, \Delta x_7, \Delta x_8]^T \\
\Delta\mathbf{U}_{cg} &= [\Delta V_{dc,ref}, \Delta Q_{g,ref}, \Delta V_{dc}, \Delta I_{dg}, \Delta I_{qg}, V_{ds}, V_{qs}]^T \\
\Delta\mathbf{Y}_{cg} &= [\Delta V_{dg}, \Delta V_{qg}]^T
\end{aligned}$$

$$\begin{aligned}
\mathbf{A}_{cg} &= \begin{bmatrix} 0 & 0 & 0 & 0 \\ 0 & 0 & 0 & 0 \\ K_{idc} & 0 & 0 & 0 \\ 0 & K_{iQg} & 0 & 0 \end{bmatrix} \\
\mathbf{B}_{cg} &= \begin{bmatrix} 1 & 0 & -1 & 0 & 0 & 0 & 0 \\ 0 & 1 & 0 & v_{qs0} & -v_{ds0} & -I_{qg0} & I_{dg0} \\ K_{pdc} & 0 & -K_{pdc} & -1 & 0 & 0 & 0 \\ 0 & K_{pQg} & 0 & K_{pQg}v_{qs0} & -K_{pQg}v_{ds0} - 1 & -K_{pQg}I_{qg0} & K_{pQg}I_{dg0} \end{bmatrix} \\
\mathbf{C}_{cg} &= \begin{bmatrix} K_{pdg}K_{idc} & 0 & K_{idg} & 0 \\ 0 & K_{pqg}K_{iQg} & 0 & K_{iqg} \end{bmatrix} \\
\mathbf{D}_{cg} &= \begin{bmatrix} d_{11} & d_{12} & d_{13} & d_{14} & d_{15} & d_{16} & d_{17} \\ d_{21} & d_{22} & d_{23} & d_{24} & d_{25} & d_{26} & d_{17} \end{bmatrix}
\end{aligned}$$

$$d_{1i} = K_{pdg} b_{3i}, \qquad d_{2i} = K_{pqg} b_{4i} \qquad i = 1, 2, \ldots, 7$$

2.2.5 DC Capacitor and the Converter Transformer Models

The rotor and grid side converters exchange power via the dc link coupling them. This primarily consists of a capacitor and, therefore, the dynamics of the dc link is mainly governed by the dynamics of the capacitor. The power loss in the converter is small (2-3%) [42] compared to the power transfer through the converter. Therefore, assuming no active power loss in the converters, the power balance in the dc capacitor gives,

$$\dot{V}_{dc} = \frac{V_{Rr} I_{Rr} + V_{Ir} I_{Ir} - V_{Rg} I_{Rg} - V_{Ig} I_{Ig}}{C Z_{base} V_{dc}} \tag{2.39}$$

where Z_{base} is the base impedance expressed with respect to the wind power plant base. Linearizing Equation (2.39) gives the small signal model for the dc capacitor as,

$$\Delta \dot{X}_{dc} \;=\; \mathbf{B}_{dc} \Delta \mathbf{U}_{cg} \tag{2.40}$$

where,

$$\begin{aligned} \Delta X_{dc} &= V_{dc} \\ \Delta \mathbf{U}_{dc} &= [\Delta V_{Rr}, \Delta V_{Ir}, \Delta I_{Rr}, \Delta I_{Ir}, \Delta V_{Rg}, \Delta V_{Ig}, \Delta I_{Rg}, \Delta I_{Ig}]^T \end{aligned}$$

$$\mathbf{B}_{dc} \;=\; \begin{bmatrix} b_{11} & b_{12} & b_{13} & b_{14} & b_{15} & b_{16} & b_{17} & b_{18} \end{bmatrix}$$

$$
b_{11} = \frac{I_{Rr0}}{CZ_{base}V_{dc0}}, \quad b_{12} = \frac{I_{Ir0}}{CZ_{base}V_{dc0}}, \quad b_{13} = \frac{V_{Rr0}}{CZ_{base}V_{dc0}}, \quad b_{14} = \frac{V_{Ir0}}{CZ_{base}V_{dc0}},
$$
$$
b_{11} = -\frac{I_{Rg0}}{CZ_{base}V_{dc0}}, \quad b_{12} = -\frac{I_{Ig0}}{CZ_{base}V_{dc0}}, \quad b_{13} = -\frac{V_{Rg0}}{CZ_{base}V_{dc0}}, \quad b_{14} = -\frac{V_{Ig0}}{CZ_{base}V_{dc0}}
$$

When modeling the wind power plant it is necessary to include the converter transformer dynamics in the model. If X_g is the transformer positive sequence leakage reactance in per unit and R_g is the transformer winding resistance in per unit, the transformer dynamics are given by,

$$
\begin{aligned}
\dot{I}_{Rg} &= \omega_0\omega_s\left(-\frac{R_g}{X_g}I_{Rg} + I_{Ig} + \frac{V_{Rs}-V_{Rg}}{X_g}\right) \\
\dot{I}_{Ig} &= \omega_0\omega_s\left(-I_{Rg} - \frac{R_g}{X_g}I_{Ig} + \frac{V_{Is}-V_{Ig}}{X_g}\right)
\end{aligned} \tag{2.41}
$$

The linearized model for the converter transformer can be written in the form,

$$
\Delta\dot{\mathbf{X}}_{tf} = \mathbf{A}_{tf}\Delta\mathbf{X}_{tf} + \mathbf{B}_{tf}\Delta\mathbf{U}_{tf} + \mathbf{E}_{tf}\Delta\mathbf{V} \tag{2.42}
$$

where,

$$
\Delta\mathbf{X}_{tf} = [\Delta I_{Rg}, \Delta I_{Ig}]^T, \qquad \Delta\mathbf{U}_{tf} = [\Delta V_{Rg}, \Delta V_{Ig}]^T
$$

$$
\mathbf{A}_{tf} = \begin{bmatrix} -\frac{\omega_0\omega_s R_g}{X_g} & \omega_0\omega_s \\ -\omega_0\omega_s & -\frac{\omega_0\omega_s R_g}{X_g} \end{bmatrix}, \quad \mathbf{B}_{tf} = \begin{bmatrix} -\frac{\omega_0\omega_s}{X_g} & 0 \\ 0 & -\frac{\omega_0\omega_s R_g}{X_g} \end{bmatrix}, \quad \mathbf{E}_{tf} = \begin{bmatrix} \frac{\omega_0\omega_s}{X_g} & 0 \\ 0 & \frac{\omega_0\omega_s R_g}{X_g} \end{bmatrix}
$$

2.2.6 Pitch Controller

If the maximum power tracking operation is allowed to continue for higher than rated wind speeds, the turbine will produce power higher than its rated value. To avoid this undesirable operating condition, the pitch angle of the blades is varied at higher wind speeds to limit the turbine power to its rated value. The control block diagram of a generic pitch controller is shown in Figure 2.7.

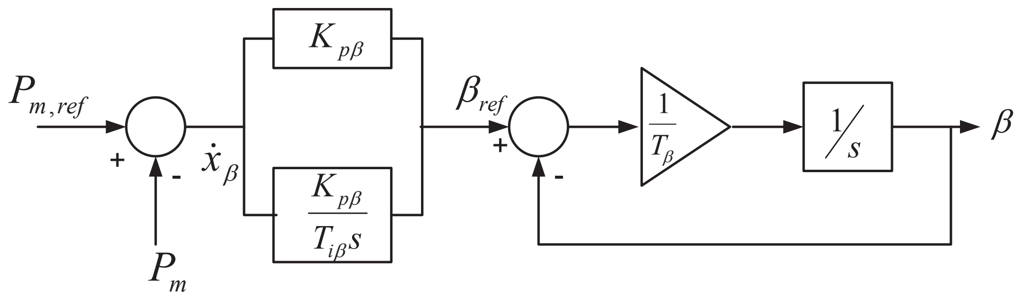

Figure 2.7: Generic pitch controller

The turbine power error is used to derive the pitch angle set point [43]. When the pitch controller is in operation there will be a time lag between the set point and the actual value of the pitch angle due to the slowness of the hydraulic actuators and large blade inertias [38]. Therefore, the actuator time constant T_β is relatively large (≈0.5 s) when compared with the pitch controller time constant $T_{i\beta}$ (≈5 ms). The pitch controller dynamic model is,

$$\begin{aligned} \dot{x}_\beta &= P_{m,ref} - P_m \\ \dot{\beta} &= \frac{1}{T_\beta}(\beta_{ref} - \beta) \\ \beta_{ref} &= K_{p\beta}(P_{m,ref} - P_m) + K_{i\beta}x_\beta \end{aligned} \tag{2.43}$$

with, $K_{i\beta} = K_{p\beta}/T_{i\beta}$. The power reference ($P_{m,ref}$) is set at 1 per unit. The linearized model of the pitch controller can be written in the state space form as,

$$\Delta\dot{\mathbf{X}}_p = \mathbf{A}_p\Delta\mathbf{X}_p + \mathbf{B}_p\Delta\mathbf{U}_p \tag{2.44}$$

where,

$$\Delta\mathbf{X}_p = [\Delta x_\beta, \Delta\beta]^T, \qquad \Delta\mathbf{U}_p = [\Delta P_{m,ref}, \Delta P_m]^T$$

$$\mathbf{A}_p = \begin{bmatrix} 0 & 0 \\ \frac{K_{i\beta}}{T_\beta} & -\frac{1}{T_\beta} \end{bmatrix}, \qquad \mathbf{B}_p = \begin{bmatrix} 1 & -1 \\ \frac{K_{p\beta}}{T_\beta} & -\frac{K_{p\beta}}{T_\beta} \end{bmatrix}$$

Note that, the active power measuring time constant was neglected when deriving the pitch controller model as it is small ($\approx$ 20 ms) compared to the actuator time constant ($\approx$ 0.5 s).

2.2.7 Relationship between Reference Frames

As mentioned earlier in this section, three different rotating frames are used to model the wind power plant. The generator is modeled in the common reference frame, the rotor side converter controls in the stator flux reference frame and the grid side converter in the generator terminal voltage reference frame. Therefore, when forming the final state space model of the wind power plant by combining individual components, the relationship between these reference frames needs to be taken into account. The relationship between the reference frames is explained using the two arbitrary orthogonal reference frames shown in Figure 2.8a.

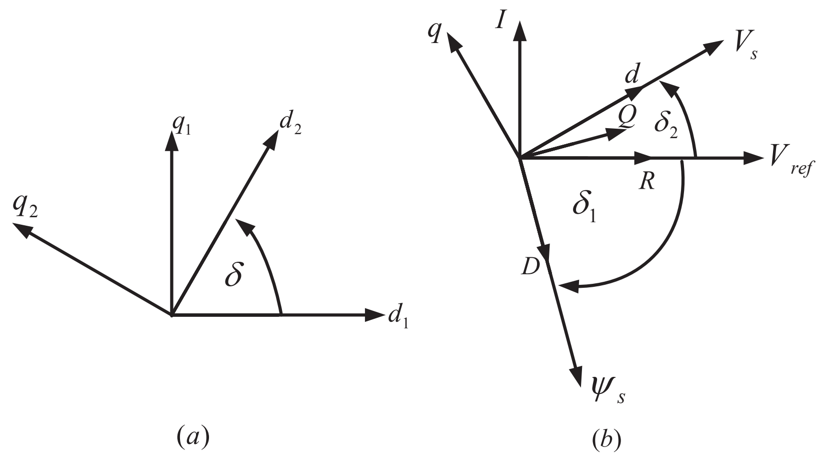

Figure 2.8: Phasor diagrams: (a) General example (b) Selection of the three reference frames used for the DFIG, RSC and GSC

Let δ be the angle between the two direct axes of reference frames and $\Delta\xi$ be a small change in any electrical variable, i.e. current, voltage or flux. Then the transformation of $\Delta\xi$ expressed in reference frame 1 to reference frame 2 is given by,

$$\begin{bmatrix} \Delta\xi_{d_2} \\ \Delta\xi_{q_2} \end{bmatrix} = \begin{bmatrix} \cos\delta_0 & \sin\delta_0 \\ -\sin\delta_0 & \cos\delta_0 \end{bmatrix} \begin{bmatrix} \Delta\xi_{d_1} \\ \Delta\xi_{q_1} \end{bmatrix} + \begin{bmatrix} -\sin\delta_0 & \cos\delta_0 \\ -\cos\delta_0 & -\sin\delta_0 \end{bmatrix} \begin{bmatrix} \xi_{d_{10}} \\ \xi_{q_{10}} \end{bmatrix} \Delta\delta \tag{2.45}$$

Figure 2.8b is a phasor diagram showing the three reference frames used in modeling the wind power plant. Table 2.1 can be used to select the parameters to be used in the transformation in Equation (2.45) when transforming between the three reference frames.

Table 2.1: Equation (2.45) parameters for various reference frame transformations

Transformation	d_1	q_1	d_2	q_2	δ
RI to DQ	R	I	D	Q	δ_1
RI to dq	R	I	d	q	δ_2

In most cases, $\delta_1 < 0$ and $\delta_2 > 0$.

2.2.8 Wind Power Plant Layout and Model Aggregation

In a typical large-scale wind power plant (several hundreds of Mega Watts), the power generated by the individual wind turbines are collected by a medium voltage (typically 25-33 kV) collector network. Often the collector system network consists of groups of wind turbines being connected to several feeders and the feeders are collected together and connected to the external network via a MV/HV transformer [44],[45].

Wind power plants consist of a large number of individual wind turbine-generator units spanned across a wide area. The amount of wind received by these units is different and, therefore, the power generated by them is not equal. An accurate study requires simulating each unit in the wind power plant in detail. However, this type of elaborate simulation is computationally expensive and would take a long time to complete. Since a detailed analysis of the power plant is required only to study the wind power plant itself, one solution to this problem is to aggregate all the wind turbine-generator units into an equivalent turbine and generator and use it in the system simulation [45], [46], [47]. In the simplest form of aggregation, it is assumed that all the units receive almost the same wind speed. The aggregation of individual wind turbine generator units under this assumption is called full aggregation [47]. Reference [47] suggests that the full aggregated model of a wind power plant is adequate for initial planning studies and transient stability studies. More recently, the full aggregated model has been used in sub-synchronous interaction studies as well [24].

When aggregating the units, the inertia of an individual unit is scaled up by the total number of units in the wind power plant while scaling down the winding resistances and the inductances by the same amount. The MVA rating of a unit is also scaled up. Therefore, the per unit inertia, resistance and the inductance of the aggregated wind power plant are equal to the corresponding quantities of an individual unit. Also, the converters and the converter transformer ratings are scaled up in the aggregated wind power plant. For example if a wind power plant consist of 100 2 MVA wind turbine-generator units with a 0.6 MVA converter transformer, the size of the aggregated wind power plant would be 200 MVA with a 60 MVA converter transformer. (Note that, the wind power plant collector system was neglected in this derivation. However, a model including the wind power plant collector system is used in Chapter 5).

The complete state space model of the wind power plant is obtained by combining the building blocks of the wind power plant explained in Section 2.2. The state space model of the wind power plant is of the form

$$\Delta\dot{\mathbf{X}}_w = \mathbf{A}_w\Delta\mathbf{X}_w + \mathbf{B}_w\Delta\mathbf{U}_w + \mathbf{E}_w\Delta\mathbf{V} \tag{2.46}$$

where,

$$\begin{aligned}
\Delta\mathbf{X}_w &= [\Delta\mathbf{X}_g, \Delta\mathbf{X}_{cr}, \Delta\mathbf{X}_{cg}, \Delta\mathbf{X}_{dc}, \Delta\mathbf{X}_{tf}, \Delta\mathbf{X}_{3M}, \Delta\mathbf{X}_p]^T, \\
\Delta\mathbf{U}_w &= [\Delta v_w, \Delta Q_{s,ref}, \Delta V_{dc,ref}, \Delta Q_{g,ref}, \Delta\beta_{ref}]^T, \\
\Delta\mathbf{V} &= [\Delta V_{Rs}, \Delta V_{Is}]^T
\end{aligned}$$

Note that $\Delta \mathbf{X}_p = 0$ and $\Delta\beta_{ref} = 0$ when pitch controller is not active.

The R and I components of the total current flowing out from the aggregated wind power plant (I_w) is used as the outputs in the state space model of the wind power plant. The total current is the addition of the current injected by the stator I_s and the current injected through the converter transformer I_g. Since I_{Rg} and I_{Ig} are states and I_{Rs} and I_{Is} can be written as combinations of states using Equations (2.18)-(2.21), the current injection equation can be written as

$$\Delta \mathbf{I}_w = \mathbf{C}_w \Delta \mathbf{X}_w \tag{2.47}$$

where, $\Delta \mathbf{I}_w = [\Delta I_{Rw}, \Delta I_{Iw}]^T$, $c_{1,1} = -\frac{L_{rr}}{\sigma}$, $c_{1,3} = \frac{L_m}{\sigma}$, $c_{1,14} = -1$, $c_{2,2} = -\frac{L_{rr}}{\sigma}$, $c_{2,4} = \frac{L_m}{\sigma}$ and $c_{4,15} = -1$. Note that $c_{i,j}$ denotes the element in the ith row and jth column of matrix $\mathbf{C}_w$.

2.3 Network Modeling

Conventional small signal stability analysis tools are meant to study low frequency electromechanical oscillations. Therefore, the fast network dynamics as well as stator flux dynamics are neglected in these programs. The ac network is modelled using constant admittances. However, these fast network transients are needed to be included when studying sub-synchronous interactions. In such studies, the fast network dynamics are modelled using dynamic phasors [48]. The following subsections describe the ac network modelling details with constant admittance method and the dynamic phasor method. The constant admittance method is presented for the sake of completeness.

2.3.1 Constant Admittance Method

In this method, all the passive elements in the network such as transformers, transmission lines, series capacitors, static loads etc. are modelled by neglecting their voltage and current dynamics [35]. Thus the voltage and current relationship for the ac network can be written in matrix form as,

$$[\mathbf{I_N}] = [\mathbf{Y_N}][\mathbf{V_N}] \tag{2.48}$$

The matrix $\mathbf{I_N}$ consist of the current injections at the network nodes in the system. If there is no current injection at node k then $I_k = 0$. The node voltages are in the matrix $\mathbf{V_N}$. The matrix $\mathbf{Y_N}$ is called the bus admittance matrix. The bus admittance matrix is a n by n matrix where n is the number of buses in the system. The bus admittance matrix can be formulated systematically by looking at the network configuration [35].

2.3.2 Dynamic Phasor Method

The basic building blocks of the dynamic phasor ac network model are the series RL circuit and the parallel RC circuit. The aforementioned passive network elements can be synthesized into series combinations of RL components and parallel combinations of RC components. Then each synthesized component can be easily represented using dynamic phasors as follows.

Dynamic phasor representation of a series RL circuit

Consider a series RL component connected between nodes 1 and 2. Then the instantaneous voltage between those nodes is give by,

$$v_{12} = Ri_{12} + L\frac{di_{12}}{dt} \tag{2.49}$$

Let $v_{12} = V_{12}\angle\phi_1 e^{j\omega_s t}$ and $i_{12} = I_{12}\angle\phi_2 e^{j\omega_s t}$, with $V_{12}\angle\phi_1$ and $I_{12}\angle\phi_2$ being the voltage phasor and the current phasor, respectively. Then, substituting these into Equation (2.49) and simplifying yields,

$$V_{12}\angle\phi_1 = RI_{12}\angle\phi_2 + j\omega_s LI_{12}\angle\phi_2 + L\frac{d(I_{12}\angle\phi_2)}{dt} \tag{2.50}$$

Note that in constant admittance modelling the time dependency of the current magnitude and phase is neglected. However, in dynamic phasor representation, the time dependency of the voltage and currents are taken in to account and hence the current derivative term was not neglected in Equation (2.50).

Expressing the per unit voltage and the current phasors in R-I reference frame and linearizing gives the state space model for the series RL component in the form,

$$\begin{bmatrix} \Delta\dot{I}_{R12} \\ \Delta\dot{I}_{I12} \end{bmatrix} = \begin{bmatrix} -\dfrac{R\omega_0}{L} & \omega_0\omega_s \\ -\omega_0\omega_s & -\dfrac{R\omega_0}{L} \end{bmatrix} \begin{bmatrix} \Delta I_{R12} \\ \Delta I_{I12} \end{bmatrix} + \begin{bmatrix} \dfrac{\omega_0}{L} & 0 \\ 0 & \dfrac{\omega_0}{L} \end{bmatrix} \begin{bmatrix} \Delta V_{R12} \\ \Delta V_{I12} \end{bmatrix} \tag{2.51}$$

Dynamic phasor representation of a parallel RC circuit

If g is the admittance of the parallel RC branch connected between nodes 1, and 2, the instantaneous current injected into the circuit at node 1 is given by,

$$i_1 = g v_{12} + C \frac{d v_{12}}{dt} \tag{2.52}$$

Following a similar procedure as in the case of a series RL circuit, the state space model of the parallel RC circuit can be easily obtained.

$$\begin{bmatrix} \Delta \dot{V}_{R12} \\ \Delta \dot{V}_{I12} \end{bmatrix} = \begin{bmatrix} -\frac{g\omega_0}{C} & \omega_0 \omega_s \\ -\omega_0 \omega_s & -\frac{g\omega_0}{C} \end{bmatrix} \begin{bmatrix} \Delta V_{R12} \\ \Delta V_{I12} \end{bmatrix} + \begin{bmatrix} \frac{\omega_0}{C} & 0 \\ 0 & \frac{\omega_0}{C} \end{bmatrix} \begin{bmatrix} \Delta I_{R1} \\ \Delta I_{I1} \end{bmatrix} \tag{2.53}$$

The complete dynamic model of the ac network in state space form as in Equation (2.54) is obtained by combining these RLC components using Kirchhoff's laws.

$$\Delta \dot{\mathbf{X}}_N = \mathbf{A}_N \Delta \mathbf{X}_N + \mathbf{B}_N \Delta \mathbf{U}_N + \mathbf{E}_N \Delta \mathbf{V}_N \tag{2.54}$$

$$\Delta \mathbf{I}_N = \mathbf{C}_N \Delta \mathbf{X}_N + \mathbf{D}_N \Delta \mathbf{U}_N + \mathbf{F}_N \Delta \mathbf{V}_N \tag{2.55}$$

where, $\mathbf{X}_N$ are the network state variables, $\mathbf{V}_N$ are unknown network voltages, $\mathbf{I}_N$ are nodal current injections and $\mathbf{U}_N$ are network inputs (if any). The current injections into the network in general can be written in terms of the network states, voltages and inputs as shown in Equation (2.55).

2.4 Interfacing the Wind Power Plant Model with the Network Model

To obtain the complete state space model of the system, the wind power plant model given in Equation (2.46) needs to be combined with the ac network model. The combination of a dynamic device model with the constant admittance ac network model is well-known and the details can be found in [35].

The wind power plant is connected to the external ac network through the point of common coupling transformer. At the interface two dynamic models, i.e. wind power plant model and the PCC transformer model are connected to each other. Electromagnetic transient (EMT) type programs use currents and voltages from the previous time step to calculate the new current to inject into the network model. Then the network model uses the new current injection to produce the new voltage to be used in the dynamic model to calculate the current for the next time step. Because of this time step delay, a sudden increase in the voltage would cause a large mismatch in the new current and the old current. To avoid this numerical instability, EMT type programs usually use a large fictitious resistor connected from the interface node to ground [49]. Following the same approach, a large fictitious resistor is used as shown in Figure 2.9 to interface the dynamic model of the wind power plant to the external ac network model.

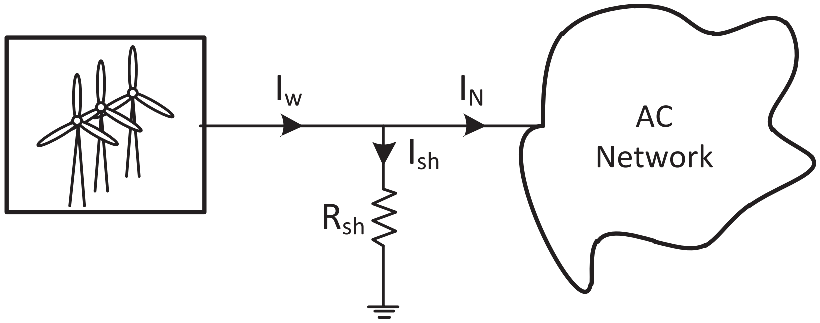

Figure 2.9: Interfacing wind power plant with the ac network

By applying Kirchhoff's current law at the wind farm terminal, the wind farm terminal voltage can be written as,

$$V = R_{sh}(I_w - I_N) \tag{2.56}$$

Substituting from Equations (2.47) and (2.55) into Equation (2.56) yields V in terms of states and inputs as,

$$\Delta\mathbf{V} = \mathbf{A}_v\Delta\mathbf{X} + \mathbf{B}_v\Delta\mathbf{U} \tag{2.57}$$

where, $\Delta\mathbf{X} = [\Delta\mathbf{X}_w, \Delta\mathbf{X}_N]^T$ and $\Delta\mathbf{U} = [\Delta\mathbf{U}_w, \Delta\mathbf{U}_N]^T$. Then Equation (2.57) is used to eliminate the wind power plant terminal voltages in the combined state space models of the wind power plant and the ac network to obtain the state space model of the complete system in the form,

$$\Delta\dot{\mathbf{X}} = \mathbf{A}\Delta\mathbf{X} + \mathbf{B}\Delta\mathbf{U} \tag{2.58}$$

The other dynamic devices in the system can be similarly added to the state space model.

2.5 Conclusions

Modelling of wind integrated power systems for small signal stability analysis was presented in the chapter. The derivation of the linearized model of the wind power plant was described in detail. The wind power plant model included the generator, drive train, rotor and grid side converter controllers, dc capacitor, converter transformer and the pitch controller models. To take the effects of the blade oscillations into account, a three-mass model was used for the drive train. An aggregated model was used in this work to represent the hundreds of wind turbines in the wind power plant. The ac network was modelled using dynamic phasors to accurately capture the effects of sub-synchronous interactions. Inclusion of the three-mass model of the drive-train is a unique feature in the model presented in this chapter, which was developed to study sub-synchronous interactions. Also, the inclusion of the interface resistor to combine the small signal current injection model with the small signal dynamic phasor network model is another novelty in the model.

Chapter 3

Model Validation

This chapter presents the validation of the linearized model developed in Chapter 2. In power system studies, Electromagnetic Transient (EMT) simulations use detailed models of the power system components. Therefore, EMT simulations produce the closest responses to the actual system. The time responses obtained with linearized models are compared with the EMT simulations. The linearized models cannot be used to simulate the response of the system for large disturbances such as faults because the linearization is valid only for small perturbations around the operating point. Therefore, the linearized models are validated by applying a small disturbance to one of the inputs in the system. Since the wind power plant model and the complete system model are obtained by adding their building blocks together, a step wise approach is followed to validate models.

3.1 Wind Power Plant Model Validation

As the first step, the dynamic behavior of a wind power plant connected to a strong network is studied. Since the wind power plant is directly connected to an infinite bus, the terminal voltage remains constant regardless of the system conditions. In general, the current injection models of dynamic devices receive feedback from the network via their terminal voltage. Since the terminal voltage remains constant, this case can be considered as studying the open loop behavior of a wind power plant.

3.1.1 Model without the Grid Side Converter

The rotor side converter produces the rotor voltage required to drive the induction generator at a desired operating point. If the dc capacitor voltage is assumed to be constant, the effects of the grid side converter (GSC) cannot be seen at the rotor side converter (RSC) terminals. Under this assumption, the RSC can be seen as a controlled three phase voltage source feeding the rotor circuit; there is no connection of the rotor circuit to the DFIG terminal. Therefore, this configuration is used to test the drive train model, generator model and the rotor voltage controllers. In this case, the RSC is modelled as an average model (i.e. as a controlled voltage source). The wind power plant is assumed to be operating in maximum power tracking mode and therefore, the pitch controller action is neglected.

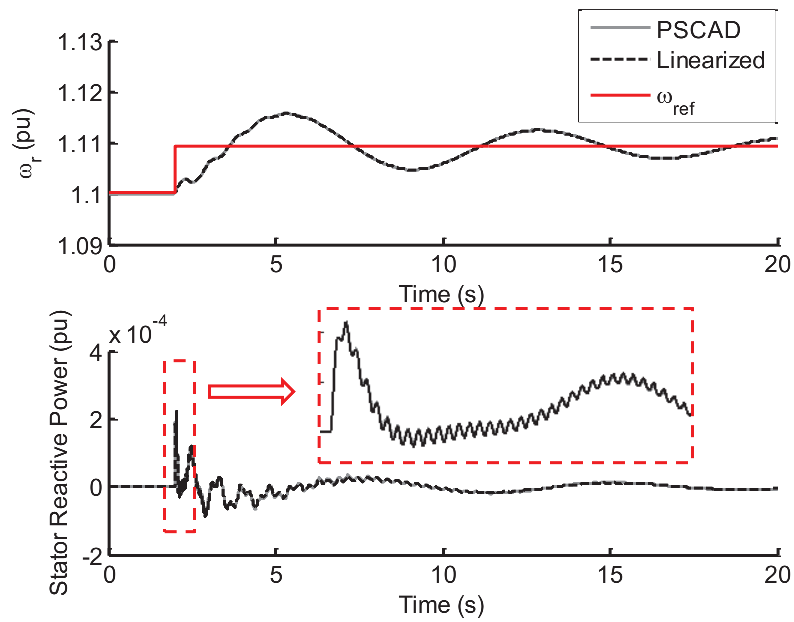

Figure 3.1: Rotor speed and stator reactive power for 1% increase in wind velocity

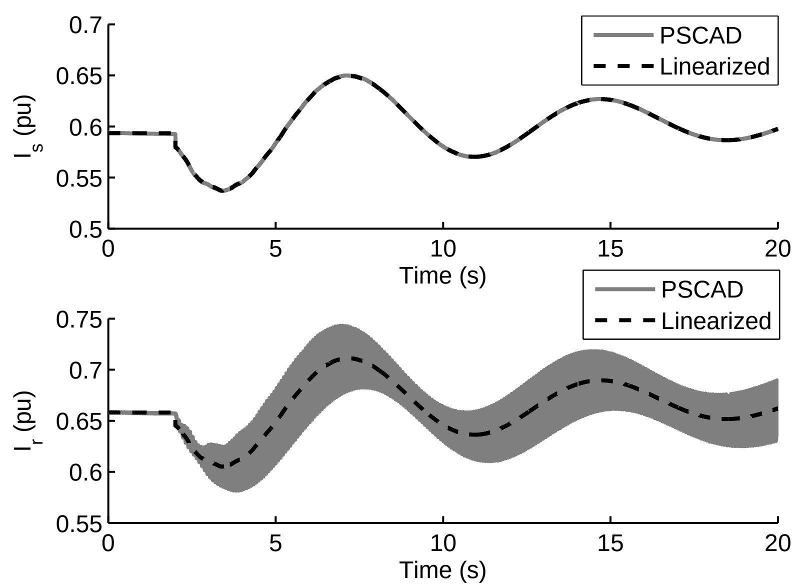

Figure 3.2: Rotor current and stator current for 1% increase in wind velocity

The responses of the generator for a 1% change in wind speed are shown in Figures 3.1 and 3.2. The wind turbine drive train is modeled as a three-mass model and the complete set of data for the generator and the drive train are given in Appendix A. The RSC controller parameters given in Table 3.1 are selected by trial and error. The initial wind speed is 12 m/s and the reactive power injected to the system by the stator is set to 0 pu.

Table 3.1: RSC converter controller parameters

K_{pQs}	K_{iQs}	$K_{p\omega s}$	$K_{i\omega s}$	K_{pdr}	K_{idr}	K_{pqr}	K_{iqr}
0.5	2.5	1.5	7.5	0.5	10	0.5	10

In the electromagnetic transient simulation case, a digital filter tuned to the fundamental frequency of the initial rotor current is used to measure its RMS value. Since the frequency of the rotor current depends on the machine slip, the rotor current frequency changes with the change of the wind speed. Therefore, when the wind speed changes, the rotor current measurement filter is not capable of properly filtering the fundamental component and hence produce an oscillating measurement (high frequency oscillations) as shown in Figure 3.2. However, when plotted with the EMT simulation result, the rotor current produced by the linearized model passes through the middle of the EMT simulation waveform. This confirms the fact that if not for the oscillations due to the inadequate filtering, the linearized model rotor current matches well with the detailed model result.

Also note that the sub-synchronous frequency-range oscillations observed during the initial transient of the stator reactive power also match well with the PSCAD simulation result. Therefore, as evident from the figures, all the quantities obtained with the linearized model match well with the results obtained with the detailed model.

3.1.2 Grid Side Converter Dynamics

The dynamics of the grid side converter controllers, the dc capacitor and the converter transformer are added to the model used in Section 3.1.1. Therefore, this section presents the validation results for the complete open-loop wind power plant model. The rotor side and grid side converters are modelled in PSCAD as average models [50]. As in the previous case, the pitch controller operation is neglected assuming maximum power tracking operation.

The initial wind speed is selected to be 12 m/s and the stator reactive power controller is set to operate so that the DFIG stator is injecting 0.25 pu reactive power into the system. The GSC is operated at unity power factor, i.e. the reactive power required by the GSC and the converter transformer is provided by the induction machine rotor circuit. The dc capacitor voltage controller in the GSC is set to 1000 V. The GSC controller parameters given in Table 3.2are selected by trial and error.

Table 3.2: GSC converter controller parameters

K_{pdc}	K_{idc}	K_{pQg}	K_{iQg}	K_{pdg}	K_{idg}	K_{pqg}	K_{iqg}
5	250	10	100	0.5	100	1	100

A comparison between linearized and PSCAD model responses of the generator speed, stator current, rotor current and wind power plant active power for a 1% step change in wind speed are shown in Figure 3.3. As the figure suggests, the linearized model results agree well with the detailed model results. The large oscillations observed in the PSCAD rotor current plot are due to the difficulty in extracting the fundamental component of the rotor current as explained in Section 3.1.1.

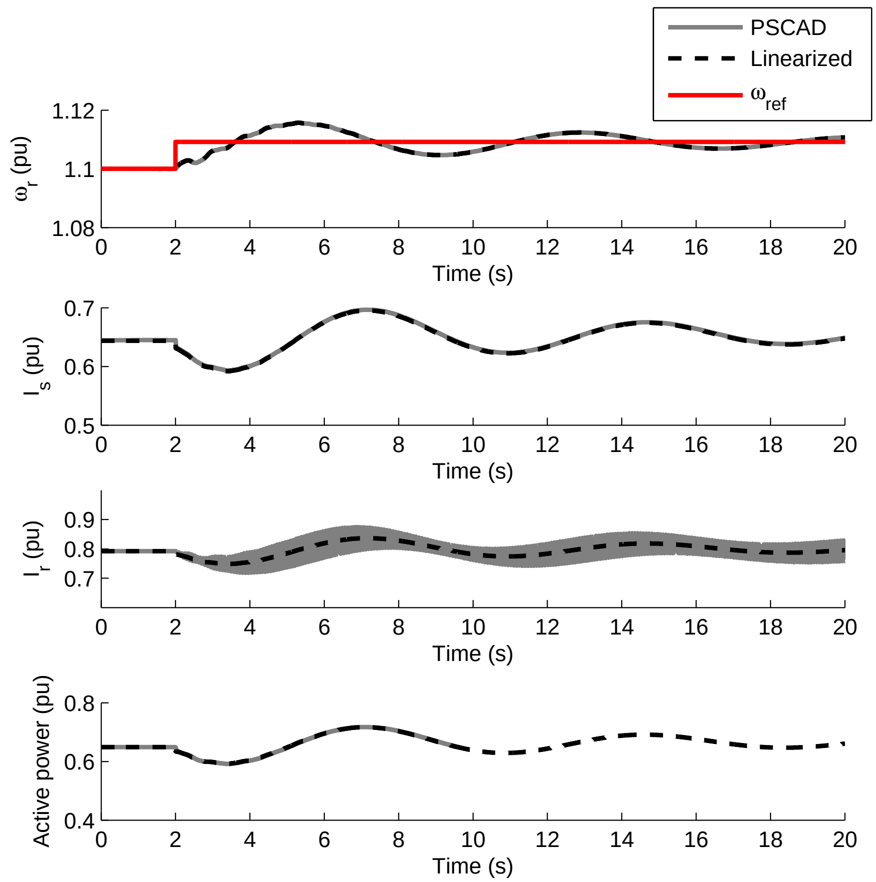

Figure 3.3: Response of the complete wind power plant model for a 1% step change in wind speed: From top to bottom - Generator speed; Stator current; rotor current; Wind power plant active power

3.2 Validating the Wind Power Plant and Network Models

Often wind power plants are located at remote locations and they are connected to the external power system via a long transmission line. Sometimes these lines are series compensated to maximize the power transfer. The results presented in this chapter are obtained with the system shown in Figure 3.4. It is derived from the IEEE first benchmark model for sub-synchronous resonance studies [19] and the network parameters are given in Appendix A. This system represents a wind power plant connected to a power system via a long series compensated transmission line. The power system is assumed to be strong at the node where the transmission line is connected. Therefore, the external ac network is represented by an infinite bus.

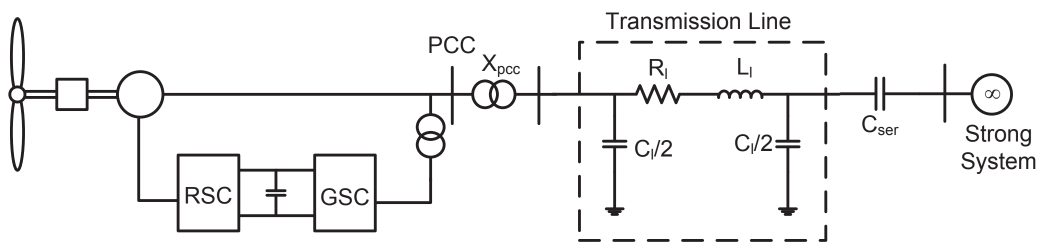

Figure 3.4: Wind power plant connected to a series compensated transmission line

In this case, the wind power plant terminal voltage changes according to the system conditions. Therefore, the wind power plant current injection model receives the feedback of the external system conditions and this case can be considered as studying the closed loop behavior.

Depending on the location of the wind power plant, the length of the transmission line connecting the wind power plant to the external system varies. The results presented in this section are obtained with a 400 km, 230 kV, 50% series compensated transmission line. The wind power plant model is obtained by aggregating one hundred 2 MW wind turbine-generator units whose parameters are given in Appendix A. The initial wind speed is selected to be 12 m/s and the stator reactive power controller is set to operate so that the DFIG is operating at the unity power factor. The reactive power required by the GSC and the converter transformer is provided by the induction machine rotor circuit. The dc capacitor voltage controller in the GSC is set to 1000 V. The controller parameters are given in Table 3.3 are selected by trial and error.

Table 3.3: Converter controller parameters

RSC Controller Parameters							
K_{pQs}	K_{iQs}	$K_{p\omega s}$	$K_{i\omega s}$	K_{pdr}	K_{idr}	K_{pqr}	K_{iqr}
0.5	2.5	30	37.5	0.025	0.5	0.025	0.5
GSC Controller Parameters							
K_{pdc}	K_{idc}	K_{pQg}	K_{iQg}	K_{pdg}	K_{idg}	K_{pqg}	K_{iqg}
5	250	10	50	1	200	1	100

The traces of the response of the wind power plant for a 1% step change in wind speed obtained from the linearized model and from a PSCAD simulation are compared. Figure 3.5 shows the response of the generator speed, wind power plant active power, series compensated line current and the generator terminal voltage for the applied disturbance. As shown in the figure, the responses obtained with the linearized model matches well with EMT simulation results in both low frequency and sub-synchronous frequency range.

The response of the generator speed, wind power plant active power, wind power plant reactive power and the generator terminal voltage obtained from the linearized model matches well with the EMT simulation responses for a 0.1 pu step increase in generator stator reactive power as shown in Figure 3.6 .

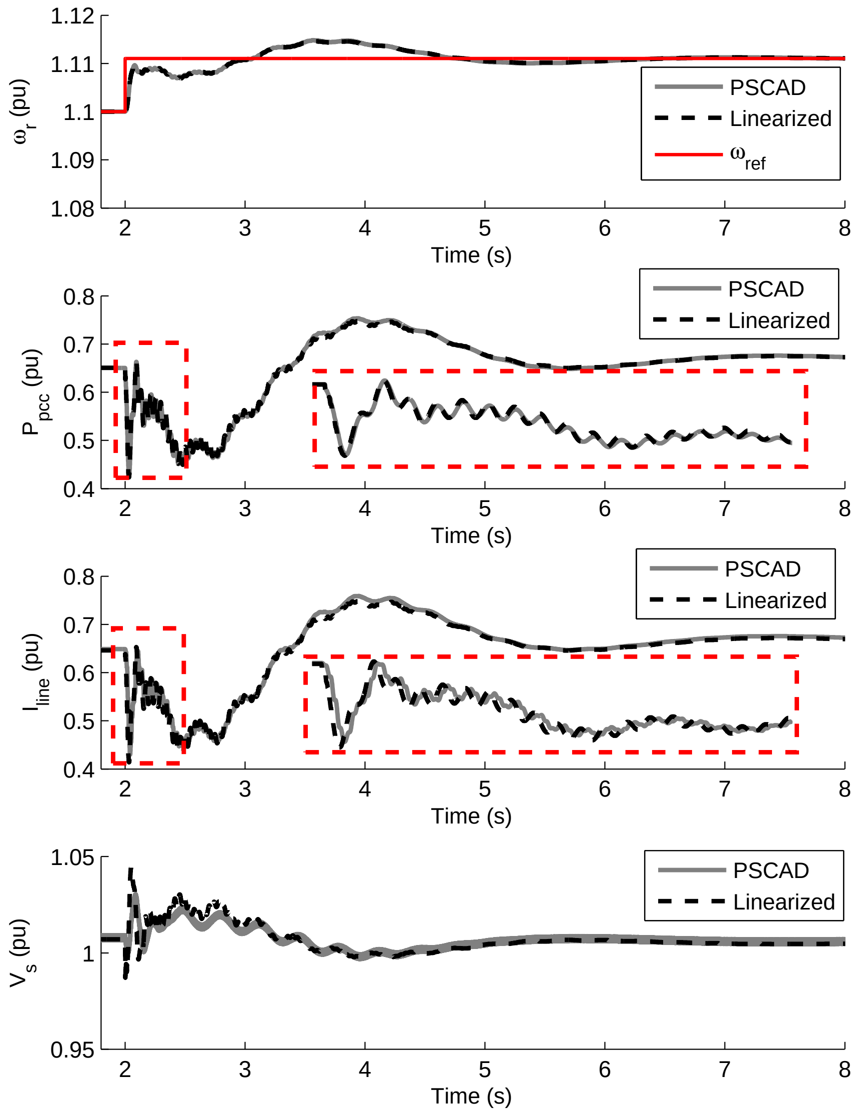

Figure 3.5: Response of wind power plant when connected to an external network with 1% step change in wind speed: From top to bottom - Generator speed; WPP active power; Line current; Terminal voltage

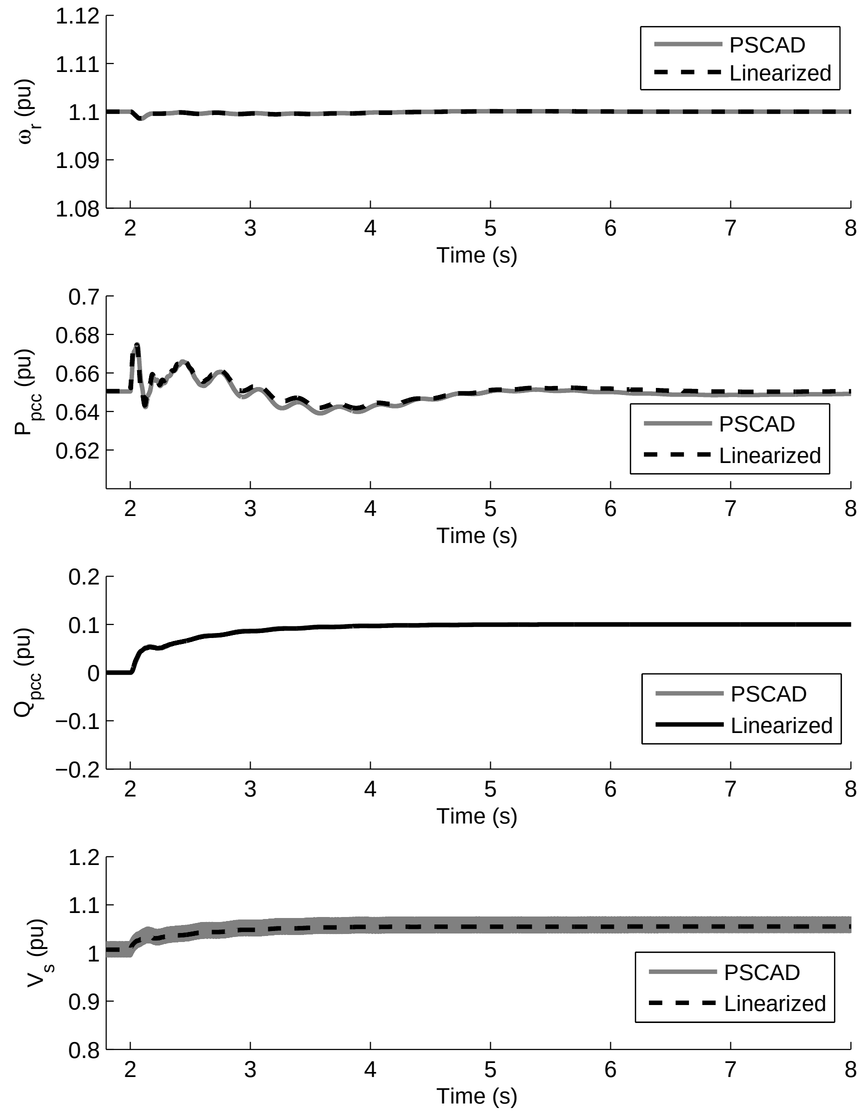

Figure 3.6: Response of wind power plant when connected to an external network with 0.1 pu step change in generator stator reactive power: From top to bottom - Generator speed; WPP active power; Stator reactive power; Terminal voltage

Although the small signal stability analysis is not meant to perform time domain simulations, this chapter presented comparisons between time domain simulations obtained with the linearized models and electromagnetic transient simulations. As mentioned at the beginning of this chapter, small signal models are valid only for small disturbances around the steady state operating point. To demonstrate this fact time domain simulations are performed with larger disturbances applied to the inputs. Figures 3.7 and 3.8 show the response of the wind power plant to a 6% step increase of the wind speed and 0.5 pu increase in stator reactive power, respectively. Note that for these disturbances the response of the wind power plant obtained with the linearized model deviates from the electromagnetic transient simulation result.

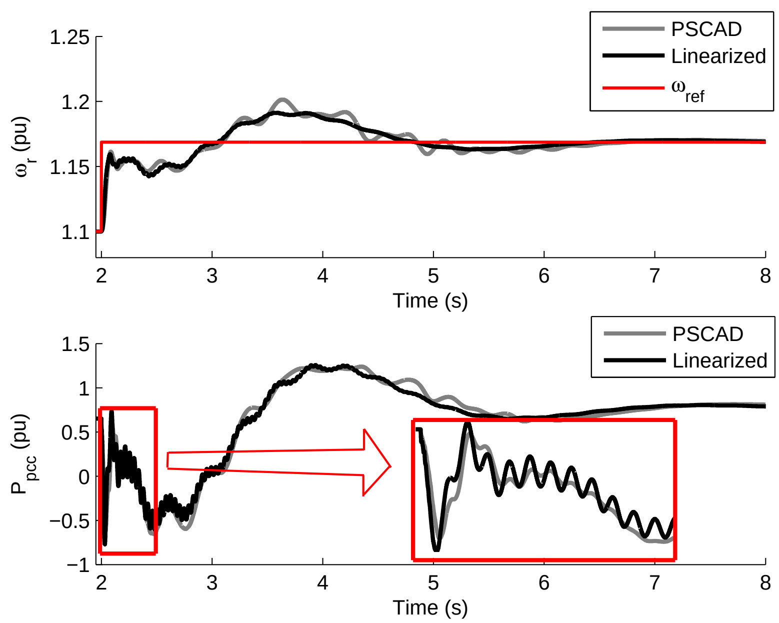

Figure 3.7: Response of wind power plant when connected to an external network with 6% step change in wind speed: Top - Generator speed; Bottom - Active power

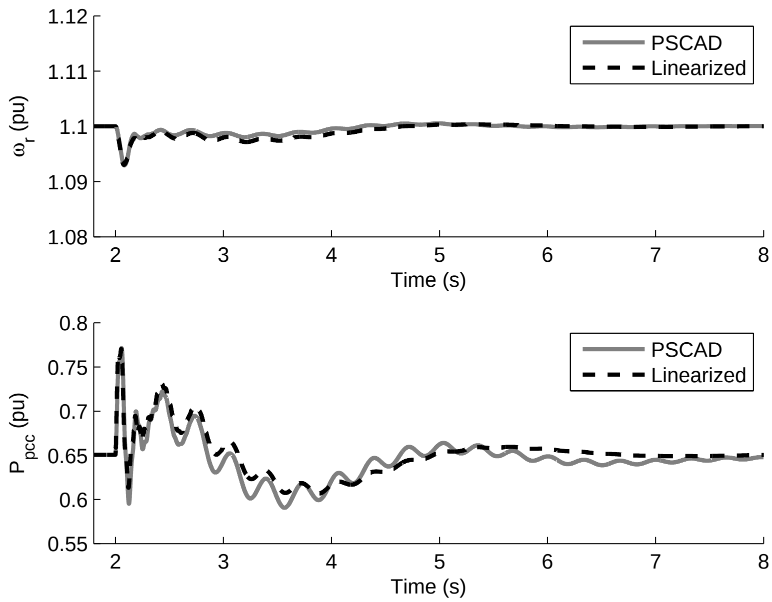

Figure 3.8: Response of wind power plant when connected to an external network with 0.5 pu step change in stator reactive power: Top - Generator speed; Bottom - Active power

3.3 Conclusions

The linearized models derived in Chapter 2 were validated by comparing with the electromagnetic transient simulations performed using PSCAD/EMTDC. From the results presented in this chapter, it is evident that when subjected to a small disturbance the linearized model is capable of producing results similar to the results produced by the detailed electromagnetic transient models. This concludes that the nonlinear system equations can be linearized around a steady state operating point without affecting the accuracy of the simulation. However, the results obtained using the linearized model are valid only for small perturbations around that operating point. Therefore, linearized models can be used to obtain information about the oscillatory stability such as modal frequency and damping, eigenvectors, mode shapes, etc., of the system close to the initial steady state operating point. The linearized system equations should not be used to perform time domain simulations of a system under a large disturbance such as a fault.

Chapter 4

Analysis of Sub-synchronous Interactions in a Wind Power Plant

4.1 Introduction

Several methods have been used to analyze sub-synchronous interactions in power systems. Frequency scan, time domain simulations, eigenvalue analysis, damping torque analysis are some of those methods that have been used in the past. Each of those methods have their merits and demerits. Often one of the aforementioned methods has been used for sub-synchronous interactions studies. The problem with such a study is that it can sometimes lead to conflicting conclusions. Such an example can be found in the literature related to sub-synchronous interactions in Type 3 wind power plants where one reference claims it is due to self excitation [24] whereas another claims it is due to controller interactions [25]. To avoid such conflicting conclusions, a comprehensive procedure to study sub-synchronous interactions in wind integrated power system is proposed in this chapter. This procedure is based on a combination of frequency scan and eigenvalue analysis. Also, this chapter includes a sensitivity analysis of the identified sub-synchronous interaction with various wind power plant and network parameters.

4.2 Study Methods

4.2.1 Frequency Scanning

Frequency scanning is a method widely used to screen thermal generators for sub-synchronous resonances. An induction generator equivalent of the synchronous generator [16], [17] is used in these studies where the driving point impedance over the interested frequency range is calculated as seen from the generator neutral as shown in Figure 4.1 .

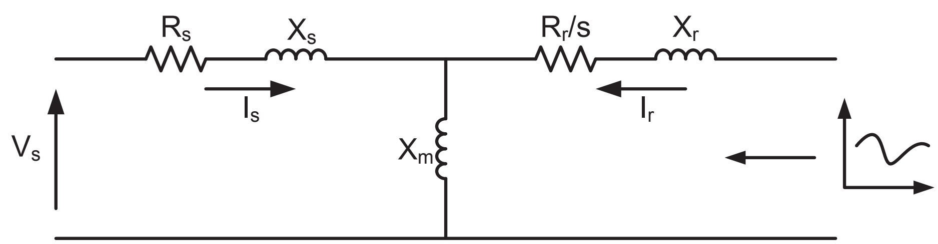

Figure 4.1: Frequency scan equivalent of a synchronous generator (Model I)

Note that this equivalent circuit is same as the steady state equivalent of a fixed speed induction generator when viewed from the generator neutral. Therefore, the circuit shown in Figure 4.1 can be used directly to screen Type 1 wind power plants for sub-synchronous interactions.

However, in case of a doubly fed induction generator, the generator is operated at the desired operating point by controlling its rotor voltage. For the purpose of frequency scanning, this voltage source can be replaced with an equivalent impedance so that the current flowing through the rotor circuit remains unchanged. Therefore, the doubly fed induction generator equivalent circuit for frequency scanning is obtained by replacing the rotor voltage source with an equivalent impedance Z_{rv} such that,

$$Z_{rv} = -\frac{V_r}{sI_r} \tag{4.1}$$

where, V_r, I_r and s are steady state values of rotor voltage, rotor current, and slip, respectively. The modified equivalent circuit is shown in Figure 4.2. Since these quantities depend on the system frequency, the value of Z_{rv} is updated for every frequency in the range of interest.

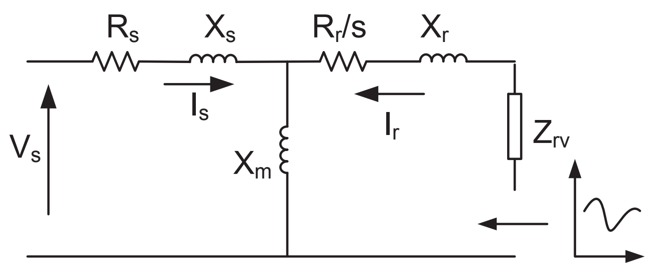

Figure 4.2: Frequency scan equivalent of a doubly fed induction generator (Model II)

For the remainder of this chapter, the two induction generator frequency scan models are identified as follows.

- Model I - Modified induction generator equivalent circuit.
- Model II - Conventional induction generator equivalent circuit.

4.2.2 Eigenvalue Analysis

The traditional small signal stability assessment programs and transient stability programs are valid for studying low frequency electromechanical oscillations. The machine stator dynamics as well as the ac network dynamics are ignored in these programs as they produce fast transients that do not affect the low frequency electromechanical oscillations. However, the stator and ac network dynamics must be modelled for studies on sub-synchronous oscillations [48], [12], [51]. The small signal model of the wind power plant is derived as described in Chapter 2. The derived wind power plant model includes the following features.

- The doubly-fed induction generator is modelled with differential equations for stator flux, rotor flux and slip.
- The wind farm drive train is modelled using the three-mass model.
- The converter transformer dynamics and the dc capacitor dynamics are included in the wind turbine-generator model
- The rotor side converter is controlled in the stator flux reference frame whereas the grid side converter is controlled in the generator terminal voltage reference frame. For both converters, a cascaded controller scheme with a fast inner current control loop and a slower outer-loop is used. The rotor side converter controller outer-loop regulates the stator reactive power and the generator speed whereas its grid side converter counterpart regulates the dc capacitor voltage and the reactive power absorbed from the grid by the grid side converter transformer.
- The full aggregation method in [47] is used to model the large number of wind-turbine generators in the wind power plant.
- Dynamic phasors are used to model the ac network.

The linearized dynamic model of the wind power plant is combined with the dynamic network model and the models of the other dynamic devices as described in Chapter 2. An eigenvalue analysis performed on the state space model of the entire system reveal the information about the oscillatory behaviour of the system as described in the following sections.

4.3 The Proposed Procedure to Study Sub-synchronous Interactions in Wind Integrated Power Systems

The simple test system shown in Figure 4.3 is used to demonstrate the application of the proposed procedure to study sub-synchronous interactions in wind integrated power systems. This system represents a Type 3 wind power plant connected to a strong power system with a long series compensated transmission line. The wind power plant and the transmission line parameters are given in Appendix A. The proposed study procedure involves,

1. screening for potential problems, and
2. detailed eigenvalue analysis.

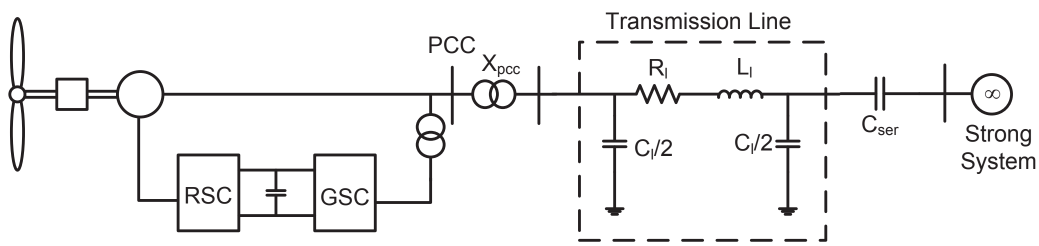

Figure 4.3: Simple test system

4.3.1 Step 1 - System preparation for frequency scan:

The potential wind power plant locations that are vulnerable to sub-synchronous interactions are identified by inspection of the single line diagram of the network. If the wind power plants are located close to the devices that are known to cause sub-synchronous interactions such as series compensated transmission lines, and HVdc converter terminals, they are selected as the candidates for the frequency scan study.

All the selected wind power plants are replaced with their frequency scan equivalent circuits (either Model I or Model II). The aggregated model of the wind power plant is used for the frequency scan study as well. The synchronous generators are replaced with their sub-transient reactances. All the static loads are represented by the corresponding load models [52].

4.3.2 Step 2 - Frequency scan study:

If the wind power plants are represented by Model I, the impedance Z_{rv} is calculated using steady state equations of the system for each frequency under investigation. The steady state equations of the wind power plant are obtained by setting the time derivatives of the differential equations given in Chapter 2 to zero. The driving point impedance when looking into the system from the rotor terminals is calculated for all the scanning frequencies. The magnitude, resistive component and the phase of the impedance obtained from the frequency scan is plotted against the scanning frequency. A change in the sign of the phase and a dip in the impedance magnitude corresponds to a series resonance seen by the wind farm under study. The frequency f_n at which this is observed is the network resonant frequency.

If a disturbance excites the network resonance, there will be sub-synchronous currents induced in the stator at the complementary frequency $f_0 - f_n$ with f_0 being the system frequency. If a constant rotor speed is assumed, the rotor will be rotating faster than the magnetic field produced by the induced sub-synchronous current. Therefore, the resistance to the induced sub-synchronous currents is negative when viewed from the rotor terminal. If the rotor resistance of the stator and the network is less than this negative resistance, the generator will be self-excited [9]. Therefore, a negative resistance at the network resonant frequency yielding from the frequency scan results represent a self-excitation of the wind power plant generators.

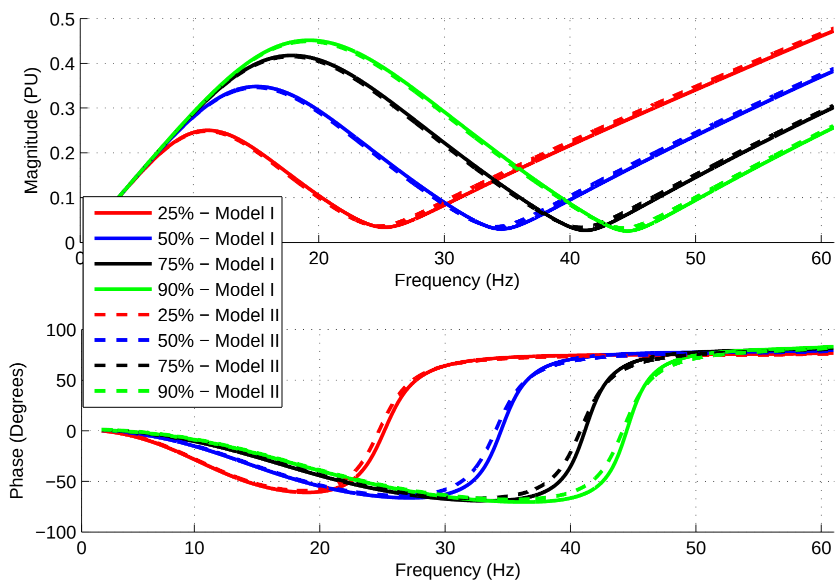

Figure 4.4: Frequency scan results for the small test system - Impedance magnitude and phase

For the small test system of Figure 4.3, the frequency scan results for different levels of series compensation are shown in Figure 4.4. The solid lines represent the results obtained when the wind power plant is represented by using Model I. The frequency scan results indicate an existence of resonance conditions at 25.34 Hz, 35.09 Hz, 42.11 Hz and 45.63 Hz for 25%, 50%, 75% and 90% compensation levels, respectively. If a disturbance excites the network resonance there will be sub-synchronous currents induced in the stator at frequencies complementary to the nominal frequency of 60 Hz; i.e. at 34.66 Hz, 24.91 Hz, 17.89 Hz, and 14.37 Hz, respectively.

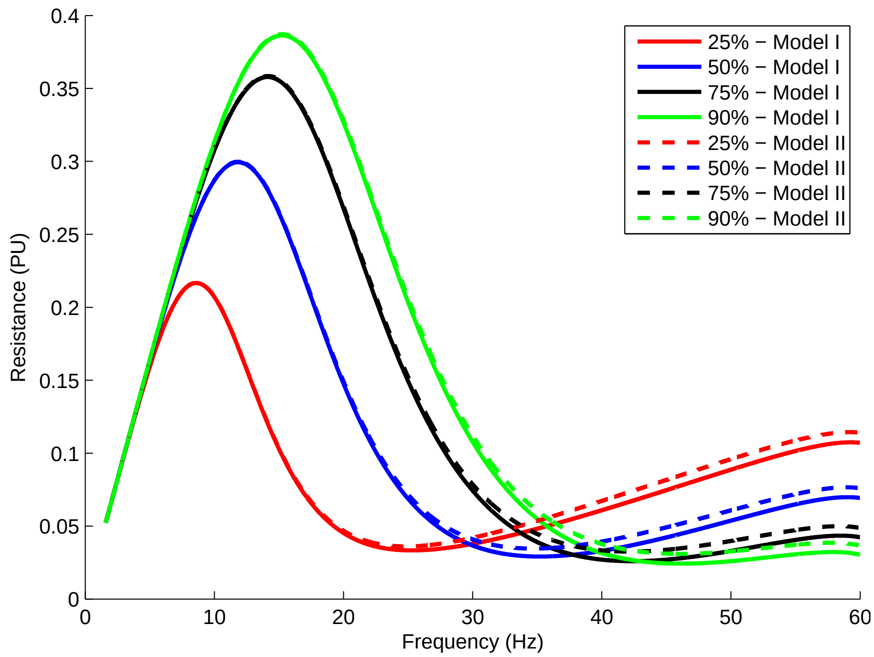

Figure 4.5: Frequency scan results for the small test system - Resistance

Figure 4.5 shows the resistance of the network seen from the rotor terminal for the aforementioned compensation levels. The equivalent resistance is positive for the tested cases indicating no self-excitation issues for the generator.

Note that Model I requires the calculation of the equivalent impedance Z_{rv} for all frequencies in the scanning range. This requires solving steady state wind power plant and network equations at all the frequencies in the scanning range. Although the solution of the steady state equations is possible for a small test system, as the system becomes larger it becomes computationally demanding.

The dotted lines in Figures 4.4 and 4.5 represent the frequency scan results with the conventional induction generator model (Model II). As seen in the figures, the results from the conventional model closely follow those from the modified induction generator mode. However, Model II does not require simultaneous steady state equation solutions. Based on these observations Model II is proposed for the frequency scan.

4.3.3 Step 3 - Detailed Analysis:

If no network resonances are found during the screening phase, the sub-synchronous interaction study procedure can stop after step 2. However, if a network resonance is found during step 2, even if the net resistance seen by the generator is positive there can still be sub-synchronous interactions between the wind power plant and the rest of the system as will be shown later in this section. It is proposed in this thesis that a detailed eigenvalue analysis be performed to obtain the information about the oscillatory modes such as their frequency, damping, and participation factors.

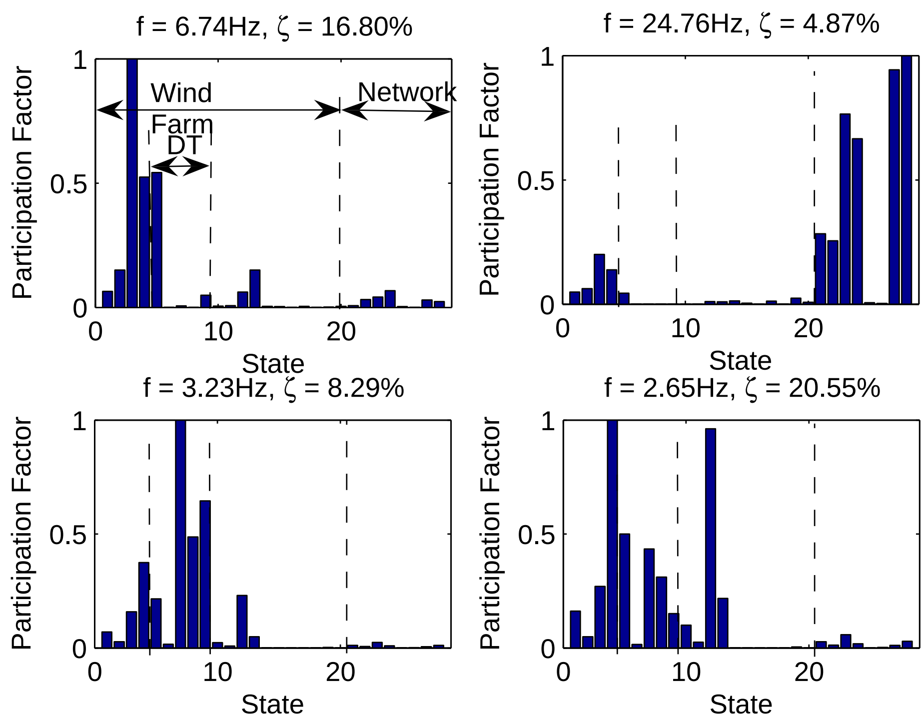

Figure 4.6: Participation factors of sub-synchronous modes with 50% compensation: States 1-4: Generator; 5-9: Drive train; 10-13: RSC controller 14: DC capacitor; 15-18: GSC controller; 19-20: Converter transformer; 21-28: network

Figure 4.6 show the participation factors of the poorly damped sub-synchronous oscillatory modes together with their frequency and damping for the test system presented. These results are obtained for 50% series compensation. In the figure, the system states are grouped so that states 1 to 4 represent the generator, 5 to 9 represent the drive train, 10 to 13 represent the rotor side converter controllers, 14 represents the dc capacitor, 15 to 18 represent the grid side converter controllers, 19 and 20 represent the converter transformer. States from 21 onwards are network states. Note that in Fig. 4.6, the network states are participating heavily in the 24.76 Hz oscillatory mode. Therefore, it can be identified as a network mode. Since the drive train states are participating heavily in the 3.23 Hz mode it can be identified as a torsional mode. Similarly, the other two modes at 6.74 Hz and 2.65 Hz are identified as an electromechanical mode and a controller mode, respectively. Apart from the network states, the generator electrical system states have some participation in the network mode (24.76 Hz), indicating a sub-synchronous interaction between the generator and the series compensated transmission line. Also, no participation of the network states in the torsional mode reveals that there is no torsional interaction present in this case. The participation of the controller states in the network mode is small compared to the generator electrical states and the states related to the series compensated transmission line.

Table 4.1: Comparison of frequency scan and small signal analysis results

Compensation Level (%)	Network Mode Frequency (Hz)			Damping (%) (Small Signal Analysis)
	Frequency Scan		Small Signal Analysis	
	Model I	Model II		
25	34.66	35.14	34.80	5.13
50	24.91	25.38	24.76	4.87
75	17.89	18.27	17.11	2.53
90	14.37	14.70	12.66	-4.49

Table 4.1 shows a comparison of the screening study results obtained with Model I, Model II and detailed analysis. Both frequency scan models can closely predict the network mode frequency discovered from the detailed analysis. For example, at 50% series compensation frequency scans performed using Models I and II indicate a network mode at 24.91 Hz and 25.38 Hz, respectively whereas the network mode frequency obtained from the small signal analysis is 24.76 Hz. Since Model II does not involve steady state calculations at each frequency, it is recommended to use Model II when screening large networks.

4.4 Sensitivity of SSI to Wind Power Plant and Network Parameters

The previous analysis was performed using a set of generic wind power plant and system parameters. In reality the wind power plant parameters and system conditions may be different from the values used. Therefore, it is important to perform a sensitivity analysis of the sub-synchronous interaction to wind power plant and network parameters. The sensitivity analysis presented in this section is concentrated on the impact of various network and wind power plant parameters on the frequency and damping of the network mode. The network mode is selected because the sub-synchronous interaction occurs between the wind power plant and the series compensated line at the network mode frequency as shown in the previous section.

First, the sensitivity of the network mode to the rotor side converter controller gains and the grid side converter controller gains are presented. The sensitivity studies presented in this section are performed on the simple test system shown in Figure 4.3. The base case used consist of a 200 MW wind power plant connected to a strong system via a 230 kV, 400 km, 50% series compensated line.

As shown in Figure 4.7 the rotor side converter controller gains do not have a significant impact on the network mode frequency. However, the inner current loop gains have a significant impact on the network mode damping. As the gain increases the network mode damping reduces. Also, higher reactive power controller gain decreases the network mode damping. However, the rotor speed controller gain does not have a significant impact on both frequency and damping of the network mode. In this study the rotor speed controller gain was increased from 5 to 45, but the change in the damping was less than 0.25%.

Figure 4.8 show the impact of grid side converter controller gains on the network

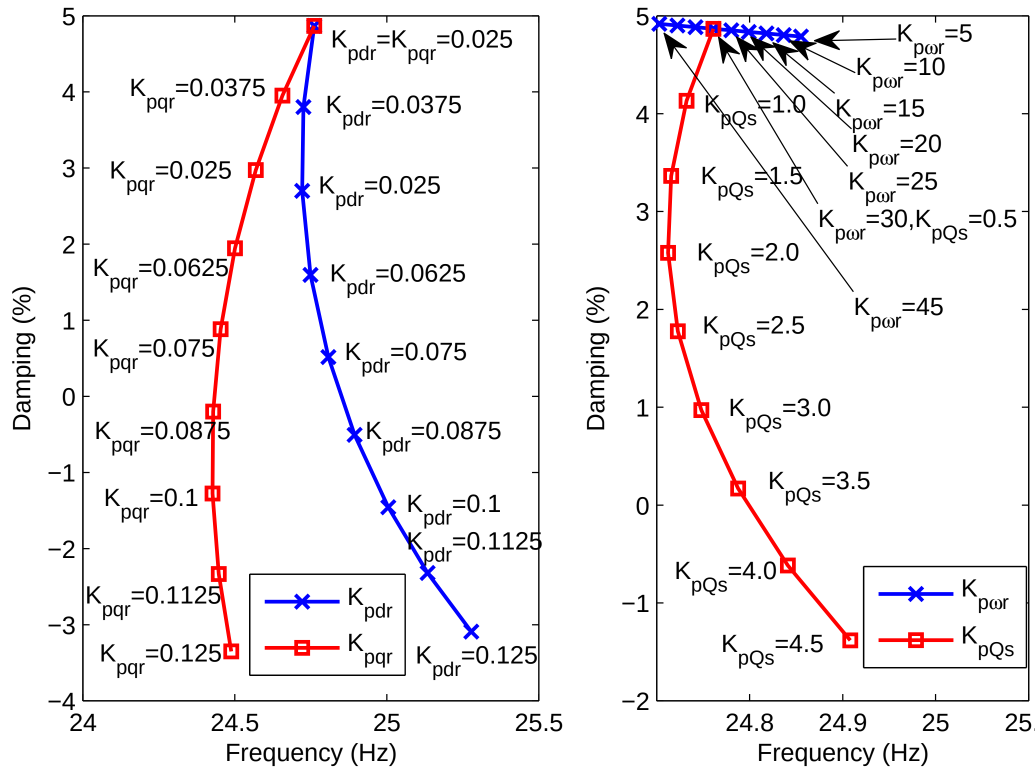

Figure 4.7: Sensitivity of the network mode to RSC controller gains: Right - outer loop; Left - inner loop

mode frequency and damping. In the base case the outer loop gains were set at $K_{pdc} = 5$ and $K_{pQg} = 10$, respectively. The inner loop gains are $K_{pdg} = K_{pqg} = 1$. As shown in the figure, the change in grid side converter controller gains do not have a significant impact on either the frequency or the damping of the network mode.

When investigating the sensitivity to the line length, compensation level and wind speed the base case consist of a 200 MW wind power plant connected to a 400 km 50% series compensated line operating under a 12 m/s wind. However, the line length was reduced to 250 km during the sensitivity analysis of the wind power plant capacity to preserve the voltage stability at wind power plant capacities greater than

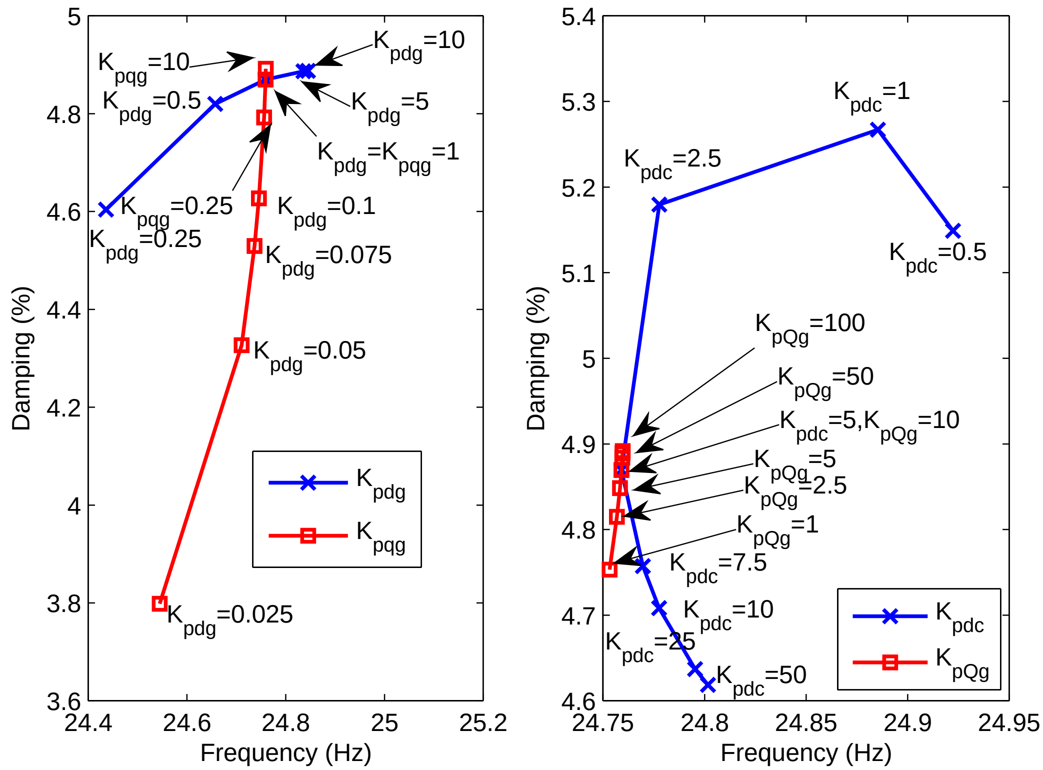

Figure 4.8: Sensitivity of the network mode to GSC controller gains: Right - Outer loop; Left - Inner loop

350 MW. Series compensated line length, compensation level and wind power plant capacity have a significant impact on both network mode frequency and damping as shown in Figure 4.9. The network mode frequency decreases with increased line length, compensation level and wind power plant capacity. However higher series compensated line lengths and wind power plant capacities improves the network mode damping whereas higher compensation levels reduce damping. The wind speed does not have a significant impact on the network mode frequency, but higher wind speeds improve the network mode damping.

The results of the sensitivity analysis of the network mode to the wind power

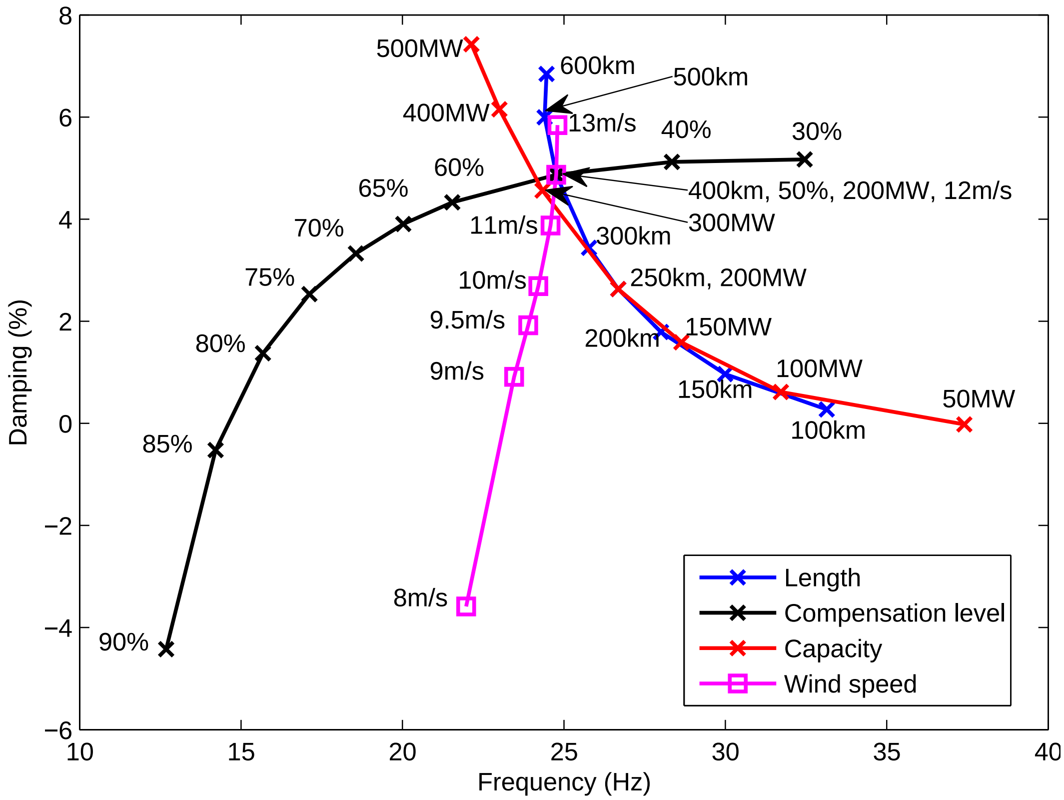

Figure 4.9: Sensitivity of the network mode to series compensated line length, compensation level, wind power plant capacity and wind speed

plant and network parameters are summarized below.

- **Higher RSC controller current loop gains** reduce the damping of the network mode. They do not have a significant impact on the frequency of the network mode.

- **Higher stator reactive power controller gains** reduce the damping of the network mode. No significant impact on the frequency of the network mode.

- **Rotor speed controller gains** do not have a significant impact on either the network mode frequency or damping.

- **Both inner and outer loop GSC gains** do not have a significant impact on either the network mode frequency or damping.
- **Increased line length, compensation level and wind power plant size** decreases the network mode frequency.
- **Increased line length, and wind power plant size** improves the network mode damping.
- **Increased compensation level** decreases the network mode damping.
- **Increased wind speed** improves the network mode damping. No significant impact on the network mode frequency.

Some of the sensitivity analysis results can be explained as follows. As the long lines have a higher resistance, the damping of the network mode increases. Higher wind speeds increase the generator slip. Thus, the generator negative resistance decreases. Therefore, higher wind speeds improve the network mode damping. Note that the sensitivity analysis with respect to the line length was performed while keeping the compensation level at 50% for all line lengths. However, in reality the shorter lines may not require that much series compensation or may not require series compensation. The damping of the SSI mode may be higher in case of a short line with low series compensation or there won't be any sub-synchronous interaction issues in the absence of series compensation.

4.5 Sub-synchronous Torsional Interactions (SSTI)

Torsional interactions occur when the torsional mode and network mode frequencies are close to each other [9]. The three-mass drive train parameters presented in [39] were used to obtain the results presented in the previous sections. Two torsional modes were observed when using the three-mass model; a low frequency oscillatory mode at 0.28 Hz related to the oscillations in the blade and a higher frequency oscillatory mode at 3.23 Hz related to the oscillations in the hub. The sensitivity study results presented in the previous sections reveal that higher capacity, higher transmission line length, and higher compensation level reduce the network mode frequency. However, even when a 400 MW wind power plant is connected to a 90% series compensated 400 km long transmission line the network mode frequency of 8.9 Hz is still significantly higher than the highest torsional mode frequency for the drive train system.

Simulations were performed with two other sets of drive train parameters [40],[33]. Even with the higher inertia constants and shaft stiffness constants in [40], the highest torsional mode frequency still remained close to 3 Hz.

A sensitivity analysis performed on the drive train parameters revealed that the stiffness of the shaft between the generator and the hub (K_2) has the highest impact on the highest torsional mode frequency. Also this parameter has a significant impact on the electromechanical mode (6.74 Hz mode on Figure 4.6). When the stiffness of the shaft between the generator and the hub increases the electromechanical mode frequency increases while decreasing its damping. Also, as K_2 increases the participation of other drive train states in this mode increase.

The top row of Figure 4.10, shows the participation factors of the network mode and the electromechanical mode for a 200 MW wind power plant connected to a 80% series compensated 400 km 230 kV transmission line. The three-mass model parameters given in [39] are used to model the drive train. The bottom row shows the participation factors of the same modes with same parameters except K_2, which has been increased to 7.0 pu/elect.rad. The increased K_2 causes the drive train parameters to participate heavily in the network mode and vice versa, characterizing a sub-synchronous torsional interaction between the wind power plant and the series compensated transmission line.

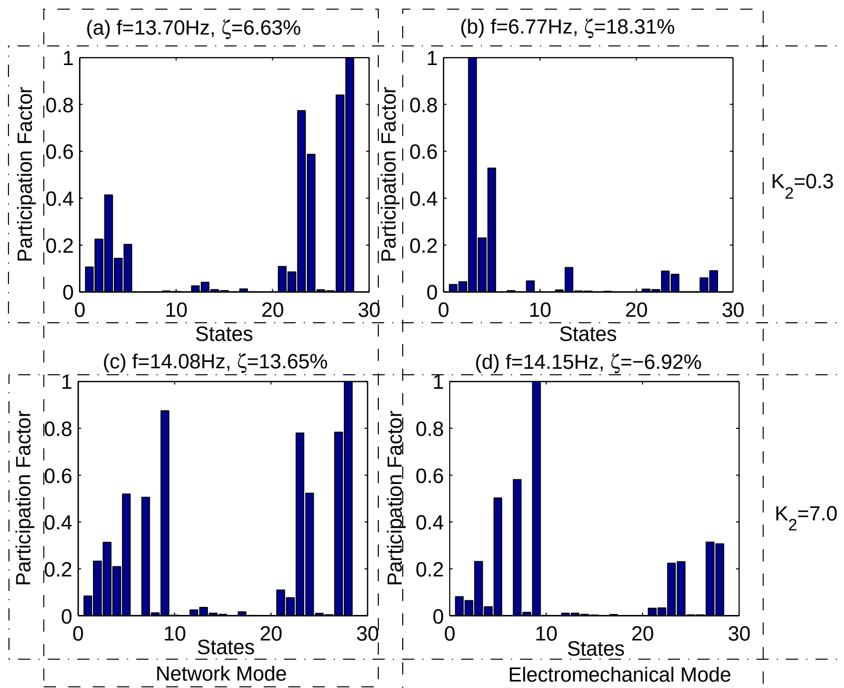

Figure 4.10: Participation factors of the network and high frequency electromechanical modes - (a). Network mode,K_2=0.3 pu/elect.rad; (b). Electromechanical mode,K_2=0.3 pu/elect.rad; (c). Network mode,K_2=7.0 pu/elect.rad; (d). Electromechanical mode,K_2=7.1 pu/elect.rad

It is worth noting that SSTI was observed only when the generator-hub shaft stiffness is much higher than the values presented in [33],[39],[40]. The second row of the Table 4.2 shows the value of K_2 given in each of the aforementioned references. The values of K_2 when the torsional interactions are observed in a 200 MW wind power plant connected to a 80% series compensated 400 km, 230 kV transmission line are given in the third row.

Table 4.2: Values of K_2 when sub-synchronous resonance due to torsional interactions observed

Drive train parameters from	[39]	[40]	[33]
Original value	0.3	6.4	0.75
When SSTI observed	7.0	38.4	6.71

Since the shaft stiffnesses at which the SSTI can occur are much higher than the available practical values, SSTI is not expected in Type 3 wind power plants.

4.6 Cause for the Generator - Series Compensated Line Interaction

The screening study presented in sub section 4.3.2 revealed that there is a network mode in the test system at sub-synchronous frequency range. The detailed small signal analysis results revealed presence of a low damped interaction between the generator and the network.

Figure 4.11(a) shows the sensitivity of the damping of network mode to the rotor side converter controller current loop input gains. As the input gains increase the damping of the network mode decreases. This indicates the rotor side converter controller has an adverse effect on the network mode damping. To further strengthen this argument the system was studied with the rotor controller being disabled. Participation factors of the network mode when the converter controllers are disabled are shown in Fig. 4.11(b). In this case the generator participation in the network mode is not as high as with the controllers. Furthermore, disabling of controllers has increased the network mode damping to 9.74%.

Fig. 4.11(c) shows the controllability of the network mode using the five available

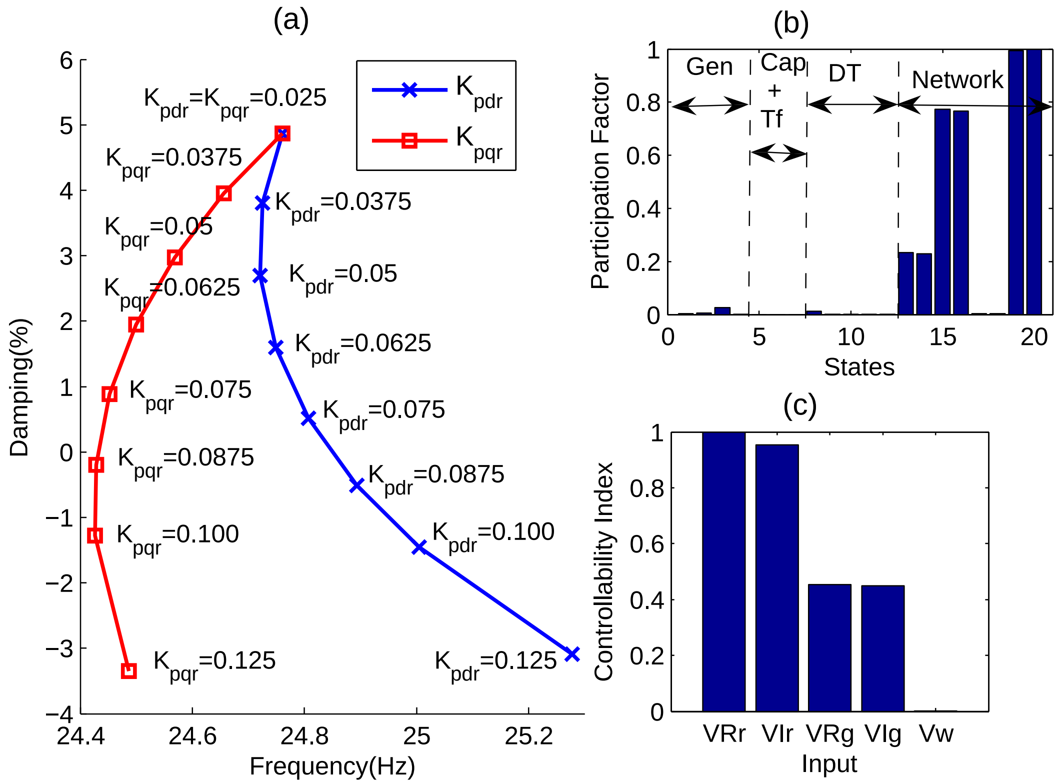

Figure 4.11: (a). Sensitivity of damping to the rotor side converter controller current loop gains; (b). Participation factors of the network mode without the converter controllers: States 1-4: Generator; 5-7: DC capacitor and the converter transformer 8-12: Drive train; 13-20: Network; (c). Controllability indices

inputs while the rotor side converter controller is disabled. As shown in the figure, the network mode is highly controllable with the two orthogonal rotor voltages. In general, if a mode can be controlled by a certain input, the controller can influence that mode either favorably or adversely. In this case the controllers have an adverse effect on the network mode. Further, the analysis of observability of this mode revealed that this mode has poor observability in controller state variables. Since the participation factor indicates the combined influence of controllability and observability, the poor observability leads to a poor participation.

The following conclusions can be drawn based on the above analysis.

- The main participants of the sub-synchronous oscillation mode are the state variables associated with the network and the generator electrical system.
- The participation of state variables associated with the controllers is relatively small.
- State variables associated with the drive train do not participate in this mode.
- This mode is highly controllable through the rotor voltage control. Therefore, the damping of the sub-synchronous mode is sensitive to the gains of the controllers.
- The sub-synchronous oscillation mode is not a torsional oscillation mode.
- This mode represents an electrical resonance between the network and the generator which is controllable through the rotor controllers.

Note that the frequency scan is performed using a steady state equivalent of the doubly-fed induction generator. Although the steady state voltage injected by the rotor side converter is included in Model I, the frequency scan results do not take into account the dynamic effect of the converter controllers. As shown in the previous analysis, the network mode becomes unstable for some values of rotor side converter current controller gains. Since the sub-synchronous oscillatory mode is caused by an electrical resonance between the network and the generator it can be concluded that for certain values of rotor side converter controller gains the dynamics of the controller makes the net resistance seen by the generator becomes negative and hence self-excites the machine. It should be emphasized that unlike the results presented in [24], the dynamics of the controller cause the machine to self-excite.

The analysis presented above clearly eliminates the fact that the sub-synchronous interaction between a Type 3 wind power plant and a series compensated transmission line is due to a controller interaction. If it is due to a controller interaction there should be a controller mode and a network mode with similar frequencies. Also, in such a case the controller states can be seen in the network mode and vice versa. However, both these conditions were not seen in the interaction between the Type 3 wind power plant and the series compensated transmission line. Recall that in the case presented, the controller mode frequency was 2.65Hz and the network mode frequency was 24.76Hz. However, if electromagnetic transient simulations were used for the analysis, one might interpret the controllability of the SSI mode with rotor side converter current controllers as a controller interaction as presented in [25].

4.6.1 Studies Required to Investigate Sub-synchronous Interactions in Wind Integrated Power systems

The objective of this section is to summarize the proposed sub-synchronous interaction study procedure elaborately described above. The proposed procedure consists of three parts, namely, screening, detailed analysis and EMT simulations.

- In the screening part, the potential wind power plants that are vulnerable to sub-synchronous interactions are first identified by inspection of the single line diagram of the network. If the wind power plants are located close to known problematic devices such as series compensated transmission lines, HVdc terminals, etc., frequency scanning is performed to identify any network resonances in the sub-synchronous frequency range. If no sub-synchronous network resonances are found during the frequency scan the procedure can stop at this stage.

- If sub-synchronous network resonances are found during the frequency scan, a detailed eigenvalue analysis is required to properly identify the sub-synchronous interaction present in the system. Eigenvalue analysis is proposed instead of electromagnetic transient simulation because the eigenvalue analysis gives an insight into the oscillatory behaviour of the system. The information such as oscillatory mode frequencies and damping, and their participation factors help to understand the root cause of the oscillatory problem in the system. Also the eigenvalue analysis results helps to effectively and systematically design sub-synchronous interaction mitigation measures.

- Once the detailed eigenvalue analysis is performed, an electromagnetic transient simulation is performed to verify the findings. Also, an electromagnetic transient simulation is necessary to investigate the impact of large system disturbances such as faults on the system and on the designed sub-synchronous interaction mitigation measures.

The next section demonstrates the application of the proposed procedure to a multi-machine power system.

4.7 An Example with a Multi-machine Power System

The test system shown in Figure 4.12 is used as the multi-machine power system. It is derived from the test system to validate HVdc and FACTS models [53]. Following modifications were made to the original test system.

- The generator connected to bus 12 was replaced with a 200 MW Type 3 wind power plant.

- The transmission line between buses 6 and 4 was 75% series compensated at the middle of the line. Two additional buses (bus 61 and 41) were introduced to connect the series capacitor.

- The bus shunts at buses 4 and 5 were removed to obtain reasonable steady state bus voltages.

- The wind farm data used in this study is the same as used in Section 4.3 except the rotor converter controller gains K_{pdr} and K_{pqr} were increased to 0.075. The controller gains was increased in order to get negative damping when the line 1-6 was tripped.

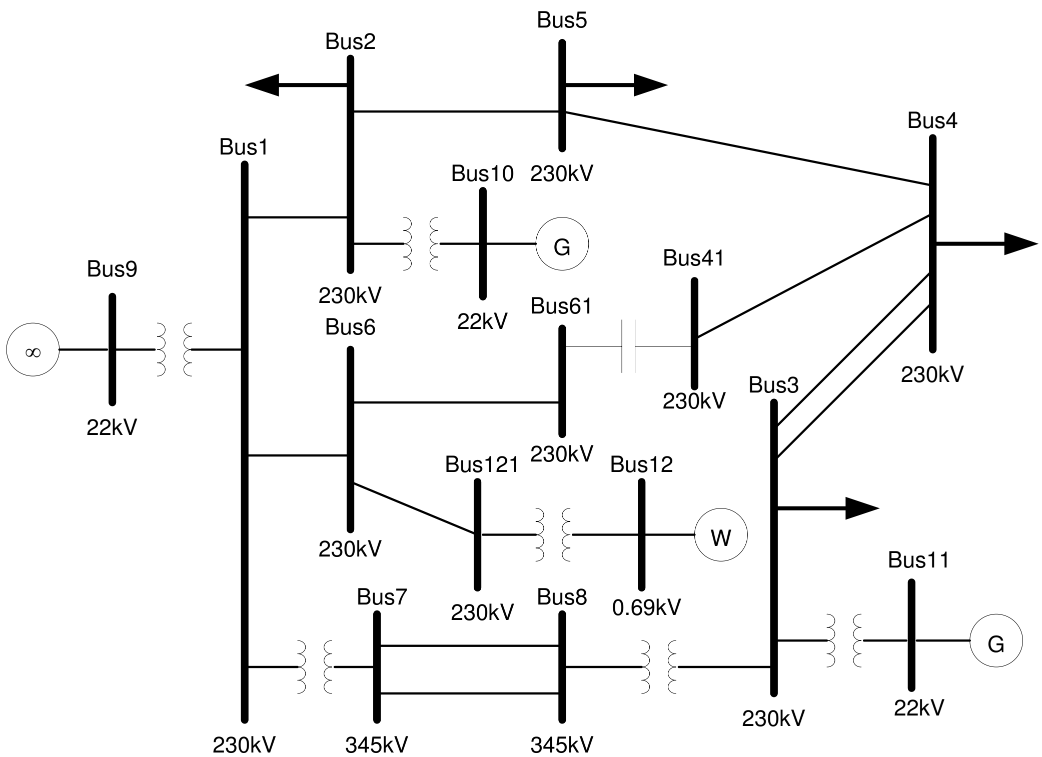

Figure 4.12: Multi-machine test system

A sub-synchronous screening was performed for the system intact condition and for the system with transmission line between bus 1 and 6 out of service. The frequency scans were conducted at the wind power plant terminal as well as at the rotor terminal using Model II. For all the cases tested a dip in the impedance magnitude was observed, indicating the presence of a network resonance. The frequency of the network resonance is given in Table 4.3. For both cases the screening results did not exhibit net negative resistance.

Table 4.3: Frequency scan results for the multi machine test system

	System Intact		Line 1-6 Out	
	At Terminal	Model II	At Terminal	Model II
Frequency (Hz)	12.8	19.7	12.1	20.3

The detailed analysis performed on the system reveals a network mode at 18.79 Hz with 2.89% damping and at 20.16 Hz with -8.51% damping for the system intact condition and the tested contingency, respectively. Figs. 4.13a and 4.13b show the participation factors for the network mode. The states related to the series capacitor and the series compensated line participate heavily in the network mode. Also, the wind power plant states, especially the generator stator flux participate in the network mode. This indicates a sub-synchronous interaction between the generator and the network further confirming the conclusions made in Section 4.6.

Fig. 4.14 shows the active power flow through the series compensated line obtained from an electromagnetic transient simulation using PSCAD/EMTDC. A three phase solid short circuit was applied on the transmission line between buses 1 and 6 at 2 s and it was cleared after 100 ms. For the system-intact case, the fault was cleared without tripping the line. As shown in the figure, a sub-synchronous oscillation can be observed in the power flow through the series compensated line as predicted by the detailed analysis. Also, as predicted the system is unstable under the contingency.

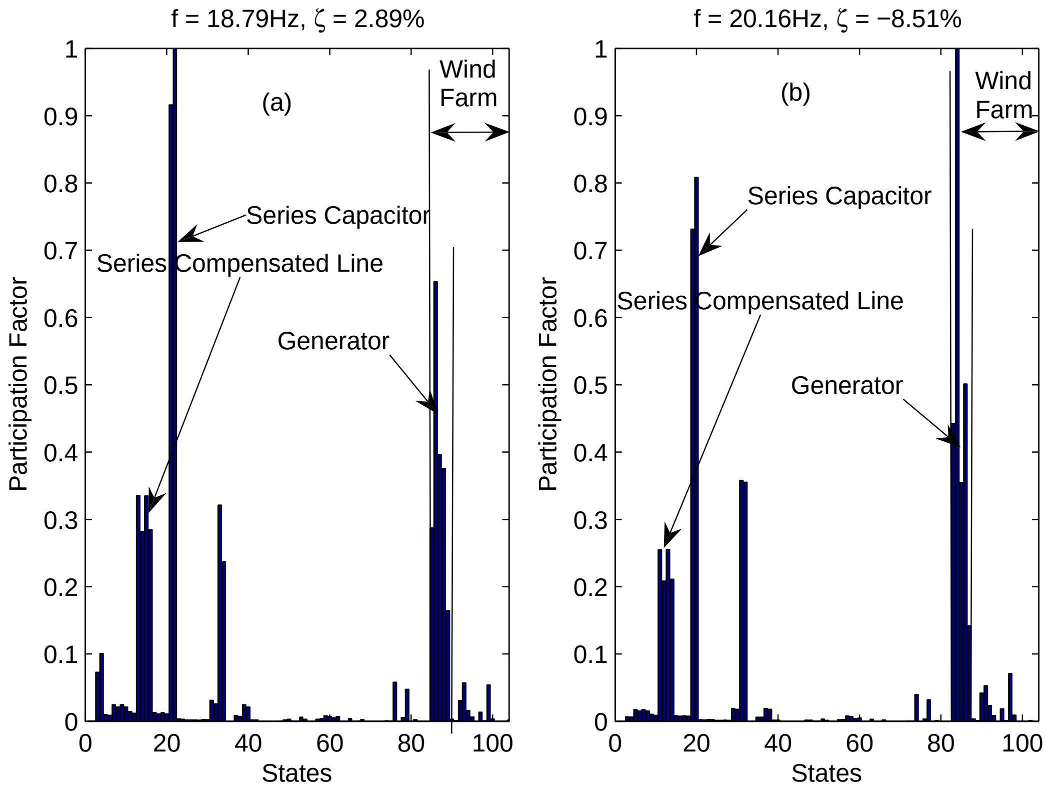

Figure 4.13: Participation factors of the network mode: (a). System intact condition; (b). Outage of the line between buses 1 and 6.

The frequency of the oscillation during the contingency is 20.4 Hz which is very close to the frequency given by the detailed analysis. For the system intact case, the frequency of the initial transient is approximately 19.6 Hz.

The procedure presented in this chapter was successfully applied to screen and study sub-synchronous interactions in a large heavily meshed power system consisting of 59 buses, six wind power plants with Type 3 generators and 5 series compensated transmission lines. The wind power plants were located in close electrical proximity of the series capacitors. When frequency scans were performed using Model II, a resonance was observed only at one wind power plant when the system was under an

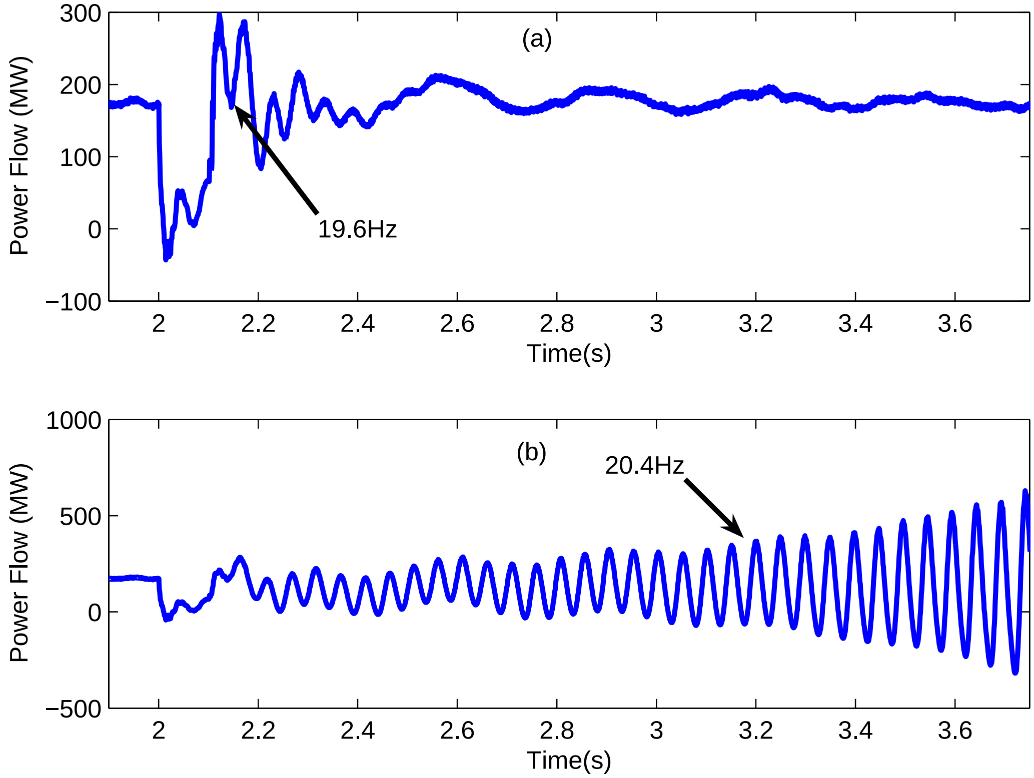

Figure 4.14: Electromagnetic transient simulation results for active power flow in the series compensated line; (a). System intact; (b). Outage of the line between buses 1 and 6.

N-2 contingency. For this contingency, although the wind power plant is not radially connected to the series compensated line, a large portion of its power transfers through those lines. Also, no self-excitation (net negative resistance) of the wind power plant generators was observed from the screening study. A detailed analysis performed on the system for the system intact and the aforementioned contingency exhibited a sub-synchronous interaction between the wind power plant generator and the series compensated line only for the N-2 contingency. The oscillatory mode frequency was 39.4 Hz and its damping was 1.9%. These observations were confirmed by comparison with electromagnetic transient simulations.

In summary, the detailed analysis performed on multi-machine power systems confirm that the sub-synchronous oscillations associated with wind power plants with Type 3 turbine-generators and series compensated networks are due to an electrical resonance between the network and the generator.

4.8 Conclusions

A comprehensive procedure to study sub-synchronous oscillations in power systems with Type 3 wind power plants and series compensated transmission lines has been proposed in this chapter. As the first step, frequency scanning is performed to identify the presence of network resonances. The use of a conventional induction generator equivalent circuit was compared against a more accurate equivalent circuit and it was shown that the conventional equivalent circuit is adequate. It has been shown that, if a network resonance is revealed in the first step, it is essential to perform a detailed eigenvalue analysis regardless of whether the net resistance seen by the generator rotor is negative or positive. The proposed detailed analysis clearly identifies the participating state variables, and the controllability of the sub-synchronous oscillation mode.

The sensitivity studies performed resulted in the following conclusions.

- Higher RSC controller current loop gains reduce the damping of the network mode. They do not have a significant impact on the frequency of the network mode.
- Higher stator reactive power controller gains reduce the damping of the network mode. No significant impact on the frequency of the network mode.
- Rotor speed controller gains do not have a significant impact on either the

network mode frequency or damping.

- Both inner and outer loop GSC gains do not have a significant impact on either the network mode frequency or damping.
- Increased line length, compensation level and wind power plant size decreases the network mode frequency.
- Increased line length, wind power plant size improves the network mode damping.
- Increased compensation level decreases the network mode damping.
- Increased wind speed improves the network mode damping. No significant impact on the network mode frequency.

The aforementioned conclusions on the sub-synchronous interactions have been further verified using multi-machine case studies. The results have been verified using electromagnetic transient simulations.

Chapter 5

Sub-synchronous Interaction Mitigation Methods

5.1 Introduction

As explained in previous chapters, eigenvalue analysis gives an insight into the oscillatory behavior of a system. The eigenstructure of the system can be utilized to derive detailed information regarding the oscillatory modes in the system. This detailed information helps in designing measures to improve the damping of any under damped oscillatory modes present in the system. One of the commonly used measures to improve damping is to add a supplemental damping controller to an existing device. An example for such application is a power system stabilizer (PSS). Eigenvalue analysis based design is widely used in tuning PSS [54]. Recently, these methods has been used to design sub-synchronous interaction damping controllers in wind power plants as well. In [31], this method has been used to systematically select an input signal for a supplementary damping controller to be included in the grid side converter of a Type 3 wind power plant. Eigenvalue analysis based damping controller design also enables the designer to optimally place the damping controller as well as precisely calculate the damping controller parameters. This chapter presents a detailed description on fully utilizing the advantages eigenvalue analysis based damping design in developing SSI mitigation measures.

5.2 Design of Sub-synchronous Interaction Mitigation Methods using Eigenvalue Analysis

Consider the state space system given in Equation (5.1) and (5.2).

$$\dot{\mathbf{X}} = \mathbf{AX} + \mathbf{BU} \tag{5.1}$$

$$\mathbf{Y} = \mathbf{CX} + \mathbf{DU} \tag{5.2}$$

The matrices $\mathbf{A}$, $\mathbf{B}$, $\mathbf{C}$, and $\mathbf{D}$ are referred to as the state matrix or the system matrix, the input matrix, the output matrix, and the feed through or feed forward matrix, respectively. For most cases $\mathbf{D}$ is zero.

The eigenvalues of the system, λ, are obtained by solving the following equation.

$$|\mathbf{A} - \lambda\mathbf{I}| = \mathbf{0} \tag{5.3}$$

Equation (5.3) is know as the characteristic equation. Let ϕ_i be the right eigenvector associated with the i^{th} eigenvalue λ_i. The right eigenvector is a vector that satisfies the following equation.

$$\mathbf{A}\boldsymbol{\phi}_i = \lambda_i\boldsymbol{\phi}_i \tag{5.4}$$

Note that $\boldsymbol{\phi}_i$ is an $(n \times 1)$ vector , where n is the number of states in the system.

Similarly, a left eigenvector $\boldsymbol{\psi}_i$, satisfies

$$\boldsymbol{\psi}_i^T \mathbf{A} = \boldsymbol{\psi}_i^T \lambda_i \tag{5.5}$$

An important property of eigenvectors is that right and left eigenvectors corresponding to different eigenvalues are orthogonal. i.e. $\boldsymbol{\psi}_j^T \boldsymbol{\phi}_i = 0$ for $i \neq j$. Also, the eigenvectors can be normalized such that $\boldsymbol{\psi}_i^T \boldsymbol{\phi}_i = 1, \forall i$.

The modal matrices $\boldsymbol{\Phi}$ and $\boldsymbol{\Psi}$ for the right and left eigenvectors are defined as,

$$\boldsymbol{\Psi} = \begin{bmatrix} \boldsymbol{\psi}_1, & \boldsymbol{\psi}_2, & \cdots, & \boldsymbol{\psi}_n \end{bmatrix}^T, \qquad \boldsymbol{\Phi} = \begin{bmatrix} \boldsymbol{\phi}_1, & \boldsymbol{\phi}_2, & \cdots, & \boldsymbol{\phi}_n \end{bmatrix} \tag{5.6}$$

Using Equation (5.4) and aforementioned eigenvector properties it can be shown that the right eigenvector matrix satisfy the relationship given in Equation (5.7).

$$\mathbf{A}\boldsymbol{\Phi} = \boldsymbol{\Phi}\boldsymbol{\Lambda} \tag{5.7}$$

where, $\boldsymbol{\Lambda}$ is a diagonal matrix of eigenvalues. Since $\boldsymbol{\Psi}\boldsymbol{\Phi} = \mathbf{I}$, by pre-multiplying Equation (5.7) with $\boldsymbol{\Psi}$ it can be easily shown that,

$$\boldsymbol{\Psi}\mathbf{A}\boldsymbol{\Phi} = \boldsymbol{\Lambda} \tag{5.8}$$

5.2.1 Controllability and Observability

Consider the transform $\mathbf{X} = \boldsymbol{\Phi}\mathbf{Z}$. If this transform is applied to Equations (5.1) and (5.2) with $\mathbf{D} = \mathbf{0}$ and pre-multiplying the resulting equation from Equation (5.1) with $\mathbf{\Psi}$, the following equations will result in.

$$\dot{\mathbf{Z}} = \mathbf{\Lambda Z} + \mathbf{\Upsilon U} \quad (5.9)$$

$$\mathbf{Y} = \mathbf{\Gamma Z} \quad (5.10)$$

where, $\mathbf{\Upsilon} = \mathbf{\Psi B}$ and $\mathbf{\Gamma} = \mathbf{C\Phi}$. The matrix $\mathbf{\Upsilon}$ is referred as the controllability matrix whereas the matrix $\mathbf{\Gamma}|$ is referred to as the observability matrix. For a MIMO system with m inputs and p outputs, the controllability matrix is a $(n \times m)$ matrix and the controllability matrix has the dimension of $(p \times n)$.

Note that each element $\dot{z}_i$ in the vector $\dot{\mathbf{Z}}$ depends only on $\dot{z}_i$ (independent of $\dot{z}_j$ for $j \neq i$). The modal transform $\mathbf{X} = \mathbf{\Phi Z}$ has in fact decoupled the modes and the variables in the vector $\mathbf{Z}$ are called modal variables. Each modal variable represent one mode in the system. The influence of the k^{th} input on the i^{th} mode is governed by the element γ_{ik} in the controllability matrix. Therefore, $\gamma_{ik} = 0$ implies that the i^{th} mode is uncontrollable through the input k.

Similarly, the weight of appearance of mode i in the k^{th} input is governed by the element υ_{ki} in the observability matrix. Therefore, $\upsilon_{ki} = 0$ means that the i^{th} mode is unobservable in the k^{th} state.

The observability indices are used to select candidate signals as input signals to the damping controllers and controllability indices are used to select potential locations to install the damping controller.

5.2.2 Participation Factors

By considering the free motion of the dynamic system given in Equation (5.9), the dynamic equation for the i^{th} modal variable can be written as,

$$\dot{z}_i = \lambda_i z_i \tag{5.11}$$

The solution of the Equation (5.11) is in the form,

$$z_i(t) = z_i(0)e^{\lambda_i t} \tag{5.12}$$

where, $z_i(0)$ is the initial value of the modal variable which can be expressed in terms of the initial values of the state variables using the inverse modal transform as,

$$z_i(t) = \boldsymbol{\psi}_i^T \mathbf{X}(0)e^{\lambda_i t} \tag{5.13}$$

Since $\mathbf{X} = \mathbf{\Phi Z}$, the time variation of the state variables can be written as a weighted sum of the modal variable time variations as shown in Equation (5.14).

$$\mathbf{X}(t) = \sum_{i=1}^{n} \boldsymbol{\phi}_i z_i(t) = \sum_{i=1}^{n} \boldsymbol{\psi}_i^T \mathbf{X}(0)e^{\lambda_i t}\boldsymbol{\phi}_i \tag{5.14}$$

Assume only the k^{th} state is excited and its initial value is unity. Then $\mathbf{X}(0) = [0, 0, \cdots, 1, \cdots, 0]$ and the time variation of $\mathbf{X}$ is given by,

$$\mathbf{X}(t) = \sum_{i=1}^{n} \psi_{ki} e^{\lambda_i t}\boldsymbol{\phi}_i \tag{5.15}$$

The time variation of the k^{th} state is given by,

$$x_k(t) = \sum_{i=1}^{n} \psi_{ki}\phi_{ki}e^{\lambda_i t} = \sum_{i=1}^{n} p_{ki}e^{\lambda_i t} \tag{5.16}$$

The factor p_{ki} is called the participation factor between k^{th} state and i^{th} mode. Therefore, the participation factor is a measure of participation of i^{th} mode in the k^{th} state in the time response.

If the initial values for the states are selected such that only the i^{th} mode is excited (i.e. $\mathbf{X}(0) = \boldsymbol{\phi}_i$), then from Equation (5.14),

$$z_i(t) = (\boldsymbol{\psi}_i^T \boldsymbol{\phi}_i)\boldsymbol{\phi}_i e^{\lambda_i t} \tag{5.17}$$

$$z_i(t) = \left[\sum_{k=1}^{n} (\psi_{ki}\phi_{ki})\right] \boldsymbol{\phi}_i e^{\lambda_i t} \tag{5.18}$$

From Equation (5.18), it can be concluded that the participation factor also represents the measure of participation of k^{th} state in shaping the time response of mode i. An important property of a participation factor is that it is a dimensionless quantity and sum of participation factors of a mode is unity.

Participation factors have been used in the past to select the best location to install a power system stabilizer to damp electromechanical oscillations [55]. In such cases, the generator whose speed is the highest participating state in the electromechanical mode is normally selected as the best location to install the PSS.

5.2.3 Residues

Mathematically, when a partial fraction term has an unrepeated binomial in the denominator, the numerator is called the residue. The residues for the power system models are calculated as follows. Consider the state space model given in Equations (5.9) and (5.10). The two equations expressed in the time domain can be transfered to the s-domain by taking the Laplace transform as shown in Equations (5.19) and (5.20).

$$s\mathbf{Z}(s) = \mathbf{\Lambda Z}(s) + \mathbf{\Psi B U}(s) \tag{5.19}$$

$$\mathbf{Y}(s) = \mathbf{C\Phi Z}(s) \tag{5.20}$$

The transfer function representation of the system is obtained by eliminating $Z(s)$ as,

$$G(s) = \frac{\mathbf{Y}(s)}{\mathbf{U}(s)} = \mathbf{C\Phi}[s\mathbf{I} - \mathbf{\Lambda}]^{-1}\mathbf{\Psi B} \tag{5.21}$$

Since $\mathbf{\Lambda}$ is a diagonal matrix,

$$[s\mathbf{I} - \mathbf{\Lambda}]^{-1} = \begin{bmatrix} \frac{1}{s-\lambda_1} & 0 & \cdots & 0 \\ 0 & \frac{1}{s-\lambda_2} & \cdots & 0 \\ \vdots & \vdots & \ddots & \vdots \\ 0 & 0 & \cdots & \frac{1}{s-\lambda_n} \end{bmatrix} \tag{5.22}$$

Substituting Equation (5.22) into Equation (5.21) and expanding the resulting equation using partial fractions yields,

$$G(s) = \sum_{i=1}^{n} \frac{R_i}{s - \lambda_i} \tag{5.23}$$

where, $R_i = \mathbf{C}\boldsymbol{\phi}_i\boldsymbol{\psi}_i^T\mathbf{B}$ is called the residue of the model i. From Equation (5.23) it can be seen that the residue quantify the influence of the input to the output through mode i. Let $F(s,k)$ be the transfer function of a feedback loop added to the system represented by the Equations (5.1) and (5.2), where k is the feed back gain. Then the eigenvalue sensitivity of a specific eigenvalue to the feedback gain is given by [56],

$$\frac{\partial \lambda_i}{\partial k} = \left(\frac{\partial \ F(\lambda_i, k)}{\partial k} \right) R_i \tag{5.24}$$

If the feedback transfer function is assumed to be a product of the static gain k and the dynamic component $F_d(\lambda)$ then, the eigenvalue sensitivity to the feedback gain can be written as,

$$\frac{\partial \lambda_i}{\partial k} = F_d(\lambda_i) R_i \tag{5.25}$$

From Equation (5.25), it can be seen that the angle of $F_d(\lambda_i)R_i$ determines the direction of the movement of the eigenvalue λ_i for a small change in the gain. Therefore, the eigenvalue can be moved in a pre-determined direction by properly selecting the angle of the dynamic component of the feedback loop. Considering the magnitude of Equation (5.25), it can be shown that the necessary gain required to move an eigenvalue by a specific distance is given by,

$$k = \frac{|\Delta \lambda_i|}{|F_d(\lambda_{i0})||R|}. \tag{5.26}$$

Note that, λ_{i0} represents the eigenvalue before it was moved.

5.3 Overview of the Test Systems

Both a single machine to infinite bus system and also a 12-bus system are used to design the sub-synchronous interaction mitigation methods. Before proceeding to the details of the design, the SSI situation in the two cases will be discussed.

5.3.1 Single Machine to Infinite Bus Case

Consider the simple test system shown in Figure 5.1. The test system is a modified version of the simple test system shown in Figure 4.3. The wind power plant medium voltage collector system model is included in this model. The reason for including the collector system will be explained later in this chapter. All the parameters of the system are the same as the values used for the SMIB case in Chapter 4 except the rotor side converter d and q axis current controller gains. In order to clearly show the effect of the damping controller, the damping of the SSI mode was reduced by increasing the d and q axis rotor side converter current controller gains to 0.115. With these new current controller gains, the frequency and damping of the SSI mode is 25.90 Hz and -3.35%, respectively.

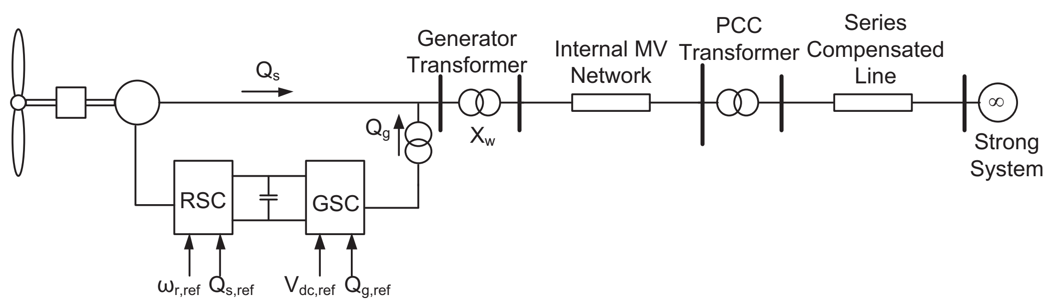

Figure 5.1: Small Test System with the Collector System

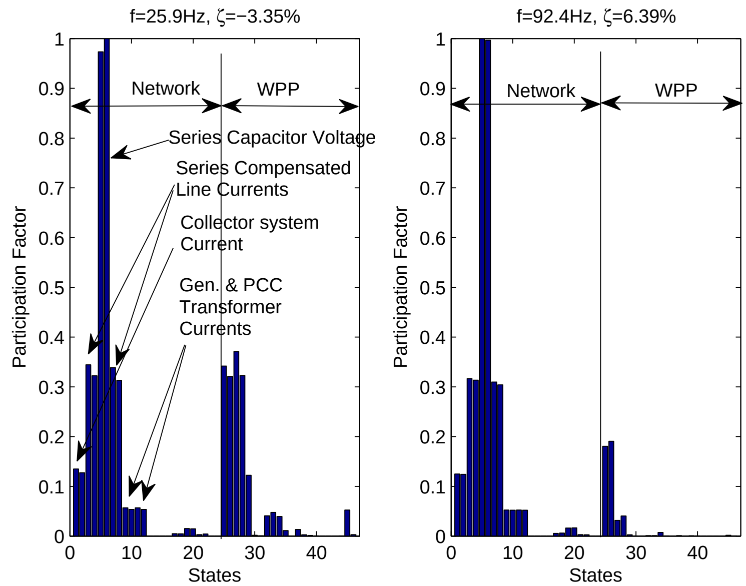

Figure 5.2: Participations of the sub-synchronous and super-synchronous modes

Figure 5.2, shows the participation factors for the sub-synchronous and super-synchronous interaction mode. As clearly seen in the figure, the major participants in the sub-synchronous interaction mode are the states related to the wind power plant generator, series capacitor voltage, series capacitor line current, PCC transformer current, generator transformer current and the internal network currents. These states are the major participants in the super-synchronous mode also.

5.3.2 Multi-machine Power System Case

The multi-machine power system used in this chapter is the modified 12 bus system used in Chapter 4. However, two switched shunts are added to Bus 4 and Bus 5 as shown in Figure 5.3. In order to maintain the system voltage between 1 and 1.1 pu two switched shunts of 80 MVAr and 120 MVAr were added to bus 4 and bus 5, respectively. Also, the wind power plant reactive power injection is set to 30 MVAr capacitive. As in the case of the simple test system presented above the rotor side current controller gains were increased to 0.09. Similar to the aforementioned simple test system, to facilitate the inclusion of the SVC/STATCOM, the wind power plant collector system is included in the model. The transformers between bus 6 and bus 121, and bus 122 and bus 12 represent the PCC transformer and the aggregated unit transformer, respectively. The medium voltage transmission line between bus 121 and bus 122 represents the aggregated collector system model.

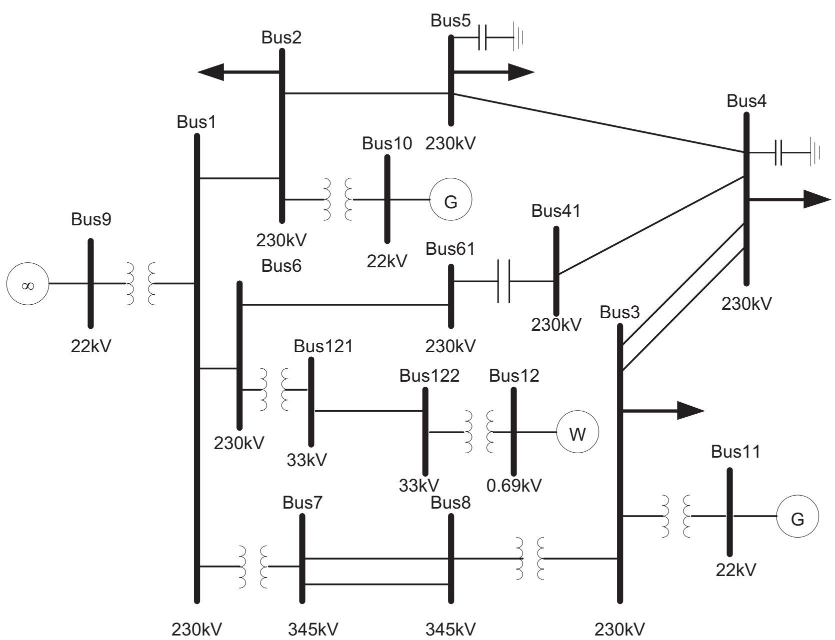

Figure 5.3: Participations of the sub-synchronous and super-synchronous modes

Two scenarios are considered in the multi-machine power system presented. The first scenario is the system intact case and the second scenario is the radial operation of the wind power plant with the series compensated transmission line following the tripping of line 1-6 due to a contingency.

As explained in Section 4.7, the series compensated line current, series capacitor voltage and the wind power plant generator stator and rotor flux are the main participants in the sub-synchronous mode. As in the simple test system presented in the previous sub-section, the major participants in the sub-synchronous mode are also the major participants in the super-synchronous mode. Table 5.1 shows the frequency and damping of the sub-synchronous and super-synchronous interaction mode for the system intact and the selected contingency. During normal operation the sub-synchronous interaction mode has almost 6% damping. However, when the wind power plant is made radial with the series compensated line following the tripping of Line 1-6 due to a fault, the damping of the sub-synchronous interaction mode is reduced to -2.61%.

Table 5.1: Frequency and damping of the sub-synchronous and super synchronous modes

Mode	System Intact		Line 1-6 Tripped	
	f (Hz)	ζ (%)	f (Hz)	ζ (%)
Sub-synchronous	19.90	5.90	22.53	-2.61
Super-synchronous	99.00	4.46	95.17	6.22

5.4 Damping of SSI using a Static Var Compensator (SVC)

As shown in Chapter 4, the rotor side converter current controller gains have a significant impact on the damping of the sub-synchronous interaction mode. It was shown that low current controller gains improves the damping of the SSI mode. However, as shown in Figure 5.4 the lower rotor current controller gains deteriorates the rate of recovery of the wind power plant voltage after a fault. Therefore, direct reduction of the rotor current controller gains is not desirable.

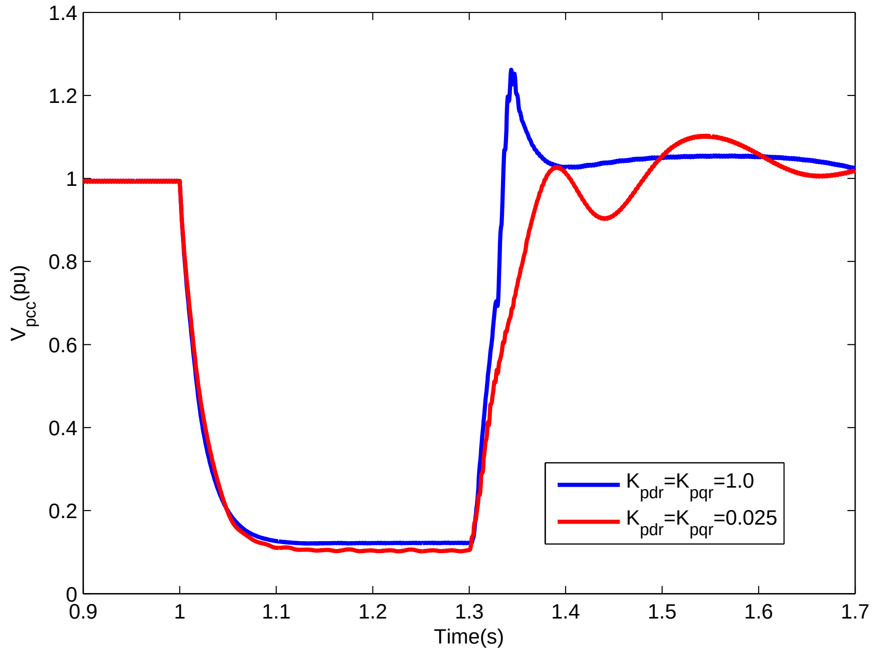

Figure 5.4: The effect of rotor current controller gains on the rate of recovery of point of common coupling bus voltage

The second option available to improve the damping of the SSI mode is to add a supplemental damping controller to the wind generator converter controllers. However, after the wind power plant is commissioned it is difficult to modify the generator controls.

Because of the drawbacks and difficulties associated with modifying wind power plant controllers, a network based SSI mitigation method is proposed in this chapter. Another benefit of a network based SSI mitigation method is that the wind development can be independent of the transmission network. This will enable the network operators to expand their transmission network so that appropriate SSI mitigation provisions are put in place even before the wind farm is connected.

In the proposed method a voltage controlling device is used as the SSI mitigation device. The performance of two devices are evaluated in this research, namely a SVC and a STATCOM. The first device evaluated is an SVC. The main advantage of a SVC over a STATCOM is its lower cost. The SVC is installed at the low voltage side of the PCC transformer as shown in Figure 5.5. The low voltage side is selected purely for the reduced cost of the equipment due to the low insulation levels. This also eliminates the need for an additional transformer as the SVC or the STATCOM can be designed to the wind power plant collector system voltage level (typically 33-66 kV). To facilitate the connection of the SVC on to the low voltage side of the PCC transformer, the wind power plant collector system is modelled and added. The parameters of the wind power plant collector system are given in Appendix A.

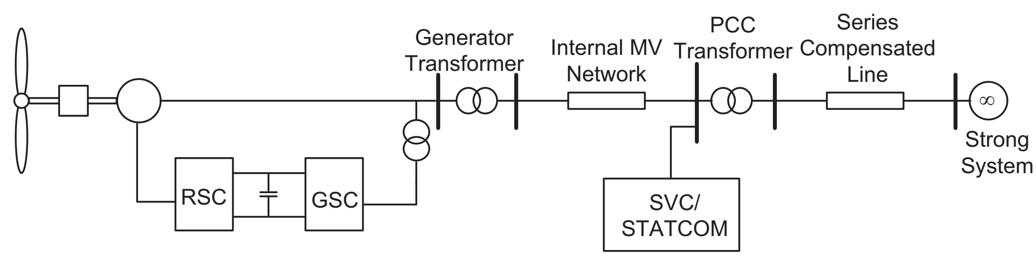

Figure 5.5: Location of the SVC

When the SVC is added to the system the damping of the SSI mode was improved from -3.35% to -1.53% without significantly affecting its frequency. With the SVC the frequency of the SSI mode is 25.65 Hz compared to 25.9 Hz without the SVC. However, when the SVC is included in the system, the damping of the super-synchronous mode reduced from 6.39% to 5.82% (well within the acceptable range of damping for the frequency).

For low frequency electromechanical oscillations, the rule of thumb is to have at least 5% damping [54]. Damping of a mode ζ is an indication of how fast the oscillations decays. In other words the amplitude of the oscillation decays to 37%

of the initial amplitude in $1/(2\pi\zeta)$ cycles. This means, the time taken to decay a high frequency oscillation to a certain magnitude is low compared to the time taken to decay a low frequency oscillation with the same amount of damping to the same amplitude. Figure 5.6 shows waveforms of two sinusoidal signals with frequencies of 1 Hz and 10 Hz. Both signals have 2% damping. The 1 Hz signal takes approximately 7.75 s to decay to 37% of the initial amplitude; whereas the 10 Hz signal only takes approximately 0.75 s to decay to 37% of its initial amplitude. Thus sub-synchronous oscillations does not require a 5% damping to be considered satisfactory. In this research 2% is considered as satisfactory.

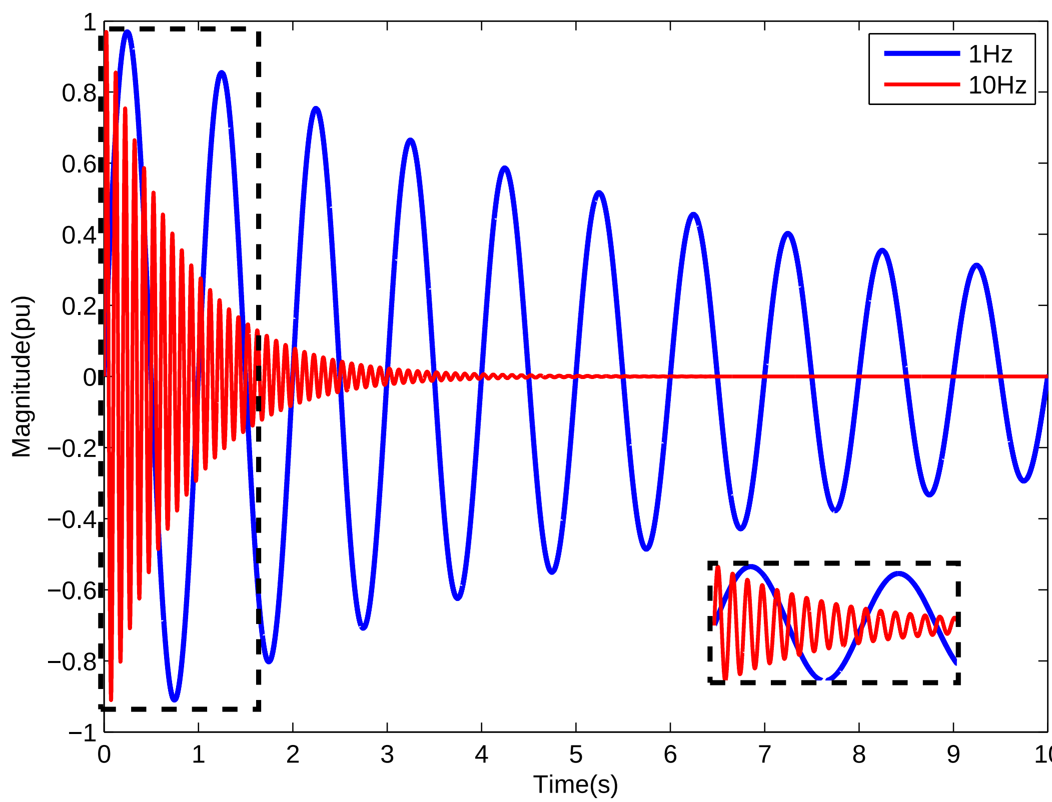

Figure 5.6: Waveforms of an 1 Hz and a 10 Hz sinusoidal signals with 2% damping

As explained above, addition of the SVC only improved the damping of the SSI mode to -1.53%. To further improve the damping to the desired level of 2% a supplemental damping controller is added to the SVC voltage controller.

5.4.1 Design of the Supplemental SSI Damping Controller

Selection of input signal to the damping controller

Recall that Figure 5.2, showed that the states related to the wind generator, series capacitor voltage, series capacitor line current, PCC transformer current, generator transformer current and the internal network currents participate heavily in the SSI mode . Note that, all these quantities appear as groups of two representing the R and I axis components. Unlike the generator speed in case of electromechanical oscillations, these quantities are not physical quantities and hence cannot be directly measured. When seeking candidate signals as the input to the damping controller, preference is given to measurable local quantities to avoid dependence on the communication. Therefore, active power injection at the point of common coupling by the wind power plant (P_{pcc}) and the current flowing through the PCC transformer (I_{pcc}) are selected as two possible candidates.

Table 5.2: Observability and Controllability of the sub-synchronous and super synchronous modes

Selected Signal	Observability	
	Sub-synchronous Mode	Super-synchronous Mode
PCC Current, (I_{pcc})	0.0747	0.0536
PCC Active Power, (P_{pcc})	0.0773	0.0545
Controllability	351.46	503.86

Table 5.2 shows the controllability of the sub-and super-synchronous modes with the voltage controller input of the SVC and the observability of the two modes with

the selected input signals. As shown in the Table 5.2 the sub-synchronous mode is observable with both candidate signals and it is controllable with the SVC voltage input. Therefore, a damping controller connected to the SVC voltage controller is capable of improving the damping of the SSI mode. However, note the non zero observability and controllability of the super-synchronous mode with the selected signals. Therefore, care must be taken when designing the damping controller as it can adversely affect the super-synchronous mode.

Table 5.3: Residues of the sub-synchronous and super-synchronous modes

Mode	Selected Signal	
	I_{pcc}	P_{pcc}
Sub-synchronous	$26.27\angle -0.71^0$	$27.16\angle -8.51^0$
Super-synchronous	$27.00\angle 0.02^0$	$27.46\angle -29.86^0$

Table 5.3 shows the residues of the sub-synchronous and super-synchronous modes obtained with the two candidate signals. Recall that the Equation (5.26) indicated that the magnitude of the residue is proportional to the the amount of distance an eigenvalue is moved for a given feedback gain. Also, the Equation (5.25) indicated that the angle of the residue gives the direction of movement of the eigenvalue for a small change in gain. Thus, when selecting an input signal and the location to inject the output of the damping controller, it is necessary to select them so that the residue magnitude of the sub-synchronous mode is high while its magnitude for the super-synchronous mode is low. Also, the residue angle for both modes should have the same sign. This will make sure that the damping controller will move both modes in the same direction while moving the sub-synchronous mode further than the super-synchronous mode. The residue magnitudes given in Table 5.3 suggests that both signals are equally good candidates for an input signal. However, the residue angle corresponding to P_{pcc} has same sign for both sub-synchronous and super-synchronous

modes while the residue angle corresponding to I_{pcc} has opposite signs for these two modes. Therefore, P_{pcc} is selected as the input signal to the damping controller.

Damping controller tuning

The damping ζ of the eigenvalue $\lambda = \sigma + j\omega$ is defined as [35],

$$\zeta = -\frac{\sigma}{\sqrt{\sigma^2 + \omega^2}} \tag{5.27}$$

The objective of the damping controller design is to move the critical eigenvalue further into the negative half of the s-plane without significantly affecting its frequency. The Figure 5.7 shows the location of the eigenvalue prior to (λ_{i0}) and after (λ_i) adding the damping controller.

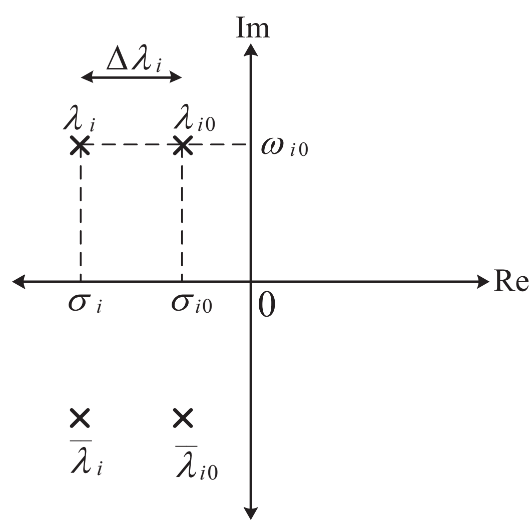

Figure 5.7: Location of the critical eigenvalue in s-plane

Assuming the frequency of the critical mode remains unchanged, the distance $\Delta\lambda_i$

at which the eigenvalue moved can be calculated from,

$$\Delta\lambda_i = \frac{\zeta_i \omega_{i0}}{\sqrt{1-\zeta_i^2}} + \sigma_{i0} \tag{5.28}$$

where ζ_i is the desired damping. Damping ratio determines the rate of decay of the oscillation.

The residue angle can be used to calculate the total phase compensation the damping controller is required to provide in order to move the critical eigenvalue further into the left-half of the s-place to improve the damping. When an eigenvalue is moved to the left without affecting its frequency, the phase is $\pm\pi$ radians. Since the eigenvalue have an inherent direction movement which is given by the residue angle, the additional phase compensation the damping controller need to provide can be calculated from,

$$\angle F_d(\lambda_i) = \pi - \angle R_i \tag{5.29}$$

If the residue angle is negative, the Equation (5.29) may result in a large phase lead. In such a case $-\pi - \angle R_i$ is used to obtain the phase lag required.

To improve the damping of the SSI mode from -1.53% to 2% in the SMIB case considered in this section, $\Delta\lambda_i = 5.6893$ and the required phase compensation is 188.52^0 leading or -171.48^0 lagging.

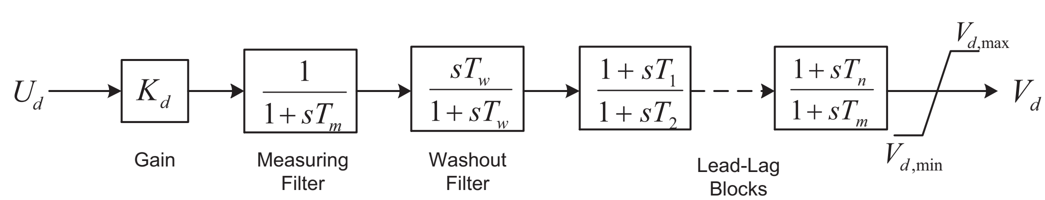

Figure 5.8: Damping Controller Block Diagram

The block diagram shown in Figure 5.8 presents a damping controller that can be used to improve the damping of the SSI in Type 3 wind power plants. It is derived from the power system stabilizer model "STAB1" in PSS/E [57]. The time constant of the measurement of the input signal is included in the model as a single pole. A washout filter is also included in the model to prevent the damping controller from affecting the steady state operation of the wind power plant control. Note that the measuring filter and the washout filter introduce a certain amount of phase compensation at the SSI frequency. If this phase compensation is not sufficient to achieve the required phase compensation, the deficit amount is provided by the lead-lag blocks. Depending on the amount of additional phase compensation to be provided, more than one lead-lag block may be required.

For the damping controller being designed a measuring time constant (T_m) of 0.01 s and a washout time constant (T_w) of 0.01 s are assumed. The washout filter time constant is selected such that it's gain is close to unity at the SSI mode frequency. Also the washout filter time constant needs to present a low gain to the low frequency oscillatory modes in the system. The measurement filter has a phase of -58.18^0 and the washout filter has a phase of 31.9^0 at the SSI mode frequency (25.65 Hz). Therefore, to achieve a phase lead of 188.52^0 the phase compensation blocks needs to provide 214.88^0. However, to achieve a phase lag of -171.48^0 phase compensation blocks need to provide only -145.12^0. Therefore, the damping controller is designed with 3 lag blocks each providing -48.37^0 at 25.65 Hz. The required time constants for the denominator and the numerator of the lag block are $T1 = 0.002$ s and $T2 = 0.014$ s, respectively. The Equation (5.26) is used to calculate the required gain. The gain required for the damping controller is 6.0567.

Linearized model of the damping controller

The linearized model of the damping controller is obtained by combining the individual linearized models of the components shown in Figure 5.8.

If U_{dm} is the input to the damping controller and V_{dm} is the measuring filter output, the linearized model of the measuring filter is given by,

$$\Delta\dot{V}_{dm} = \frac{1}{T_m}(K_d \Delta U_{dm} - \Delta V_{dm}) \tag{5.30}$$

The model of the washout filter is given by,

$$\begin{aligned} \Delta\dot{x}_w &= \frac{1}{T_w}(-\Delta x_w + \Delta U_w) & (5.31) \\ \Delta V_w &= -\Delta x_w + \Delta U_w & (5.32) \end{aligned}$$

where, U_w and V_w are washout filter input and output, respectively. x_w is a state selected such that $x_w = U_w - V_w$.

If U_l and V_l are the lead-lag block input and output, respectively, the linearized model of a lead-lag block is given by,

$$\begin{aligned} \Delta\dot{x}_l &= -\frac{1}{T_2}\Delta x_l + \left(1 - \frac{T_1}{T_2}\right)\Delta U_l & (5.33) \\ \Delta V_l &= \frac{1}{T_2}\Delta x_l + \frac{T_1}{T_2}\Delta U_l & (5.34) \end{aligned}$$

where x_l is a state selected such that $x_l = T_2 V_l - T_1 U_l$.

When the blocks are connected together in a linear daisy chain, an output of of block becomes an input to its neighbour. Therefore, the linearized model of the damping controller with a single lead-lag block is given by,

$$\Delta\dot{\mathbf{X}}_{damp} = \mathbf{A}_{damp}\Delta\mathbf{X}_{damp} + \mathbf{B}_{damp}\Delta\mathbf{U}_{damp} \tag{5.35}$$

$$\Delta\mathbf{Y}_{damp} = \mathbf{C}_{damp}\Delta\mathbf{X}_{damp} \tag{5.36}$$

where,

$$\Delta\mathbf{X}_{damp} = [\Delta V_{dm}, \Delta x_w, \Delta x_l]^T, \qquad \Delta\mathbf{U}_{damp} = \Delta U_{dm}, \qquad \Delta\mathbf{Y}_{damp} = \Delta V_l,$$

$$\mathbf{A}_{damp} = \begin{bmatrix} -\frac{1}{T_m} & 0 & 0 \\ \frac{1}{T_w} & -\frac{1}{T_w} & 0 \\ \left(1 - \frac{T_1}{T_2}\right) & -\left(1 - \frac{T_1}{T_2}\right) & -\frac{1}{T_2} \end{bmatrix}, \qquad \mathbf{B}_{damp} = \begin{bmatrix} \frac{K_d}{T_m} \\ 0 \\ 0 \end{bmatrix},$$

$$\mathbf{C}_{damp} = \left[\frac{T_1}{T_2}, -\frac{T_1}{T_2}, \frac{1}{T_2}\right].$$

If more that one lead-lag block is present it is simply added into the daisy chain. The damping controller is connected to the SVC voltage set point. A detailed description of the linearized model of the SVC is given in Appendix B.

Effect of the damping controller

Table 5.4 shows the effect of the designed damping controller on the sub-synchronous mode and the super-synchronous mode. The damping controller has improved the damping of the sub-synchronous mode to 2.05% without significantly affecting the super-synchronous mode. The phase angle of the damping controller at the super-synchronous frequency is -171.4^0. With a residue angle of -29.9^0 the eigenvalue corresponds to the super-synchronous mode should move at an angle of -202.3^0. However, the gain offered by the damping controller to the super-synchronous mode is very low (0.0066), Therefore, the movement of the eigenvalue corresponding to the super-synchronous mode is low. This is the reason for the damping controller not significantly affecting the super-synchronous mode. Also, the designed damping controller did not destabilize the other stable oscillatory modes present in the system.

Table 5.4: Effect of the damping controller on sub-synchronous and super-synchronous modes

Mode	Without Damping Controller		With Damping Controller	
	f(Hz)	ζ(%)	f(Hz)	ζ(%)
Sub-synchronous	25.65	-1.53	25.56	2.05
Super-synchronous	92.84	5.82	92.84	5.85

Figure 5.9 shows the root locus of the modes that has less than 10% damping after the damping controller is included in the SVC. Also, the figure shows the root locus of the electromechanical mode. The movements of the eigenvalues when the damping controller gain K_d is varied from $0.1K_d$ to K_d with P_{pcc} as the damping controller input and with I_{pcc} as the damping controller input are shown in the figure. As shown in the figure, the damping controller does not significantly move the eigenvalues except the ones corresponding to the sub-synchronous interaction mode and the electromechanical mode. With both inputs, the eigenvalue corresponding to the electromechanical mode moved towards the positive half of the s-plane while moving the eigenvalue corresponding to the sub-synchronous interaction mode to the left half of the s-plane. The reason for this movement is the large positive residue angle and large residue magnitude for the electromechanical mode ($17.57\angle 100.14^0$ with I_{pcc} and $10.67\angle 92.52^0$ with P_{pcc}). However, with either input the damping of the electromechanical mode remained well above the desired level. With P_{pcc} as the input the damping of the electromechanical mode is 18.47% and with I_{pcc} as the input it is

10.64%.

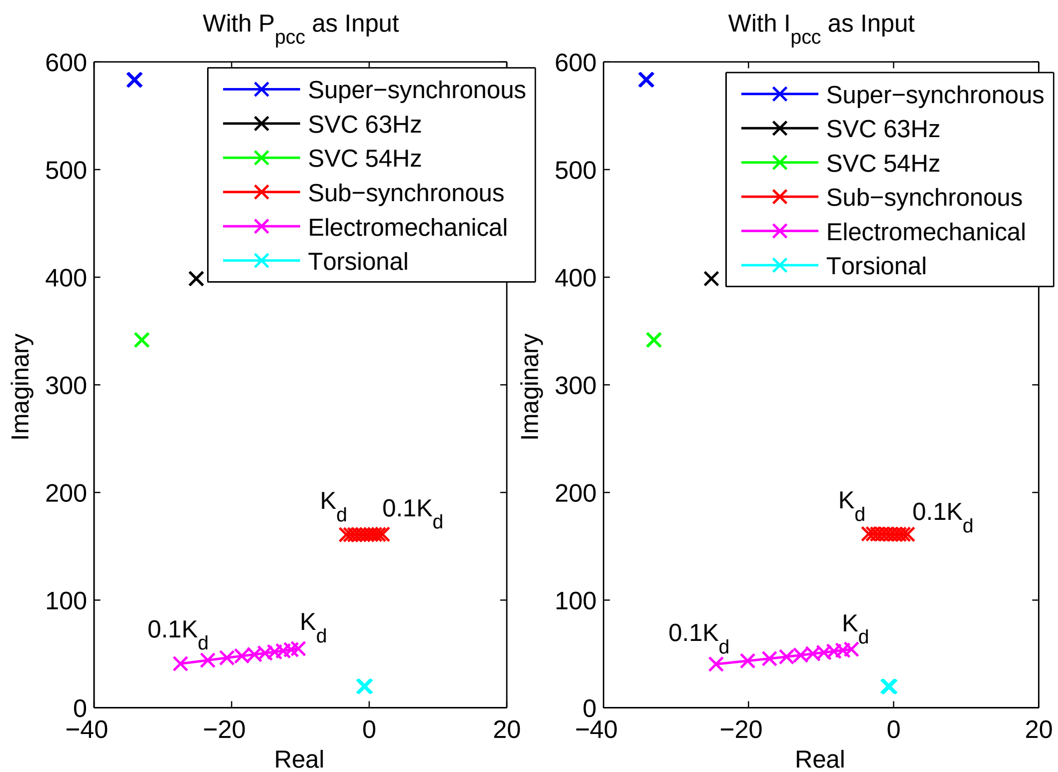

Figure 5.9: Root locus with damping controller: Left - P_{pcc} as Input; Right - I_{pcc} as Input

Performance of the Damping Controller

The performance of the designed damping controller is investigated using electromagnetic transient simulations. Figure 5.10 shows the response of the wind power plant for a 1% step increase in wind speed with and without the SVC damping controller. The system becomes unstable without the damping controller due to the sub-synchronous interaction of the wind power plant and the series compensated transmission line. As predicted from the small signal analysis, the frequency of the sub-synchronous interaction without the damping controller is is 25.6 Hz. However, when the damping controller is in service the damping of the sub-synchronous interaction improves significantly. Due to the damping controller the SVC absorbs 18 MVAr of reactive power during the transient.

To test the performance of the damping controller for a large disturbance, a high impedance three phase to ground fault is applied at the middle of the series compensated line. The fault impedance was selected such that, the point of common coupling bus has 70% residual voltage during the fault. The response of the wind power plant is shown is Figure 5.11. As shown in the figure, the SVC damping controller maintains the stability of the system after clearing the fault. If the damping controller is out of service the system becomes unstable due to the sub-synchronous interaction. In this case the SVC injects a maximum of 100 MVAr into the system during the recovery from the fault. The participation factor analysis of the low frequency oscillation observed in the SVC reactive power reveled that it was an SVC mode.

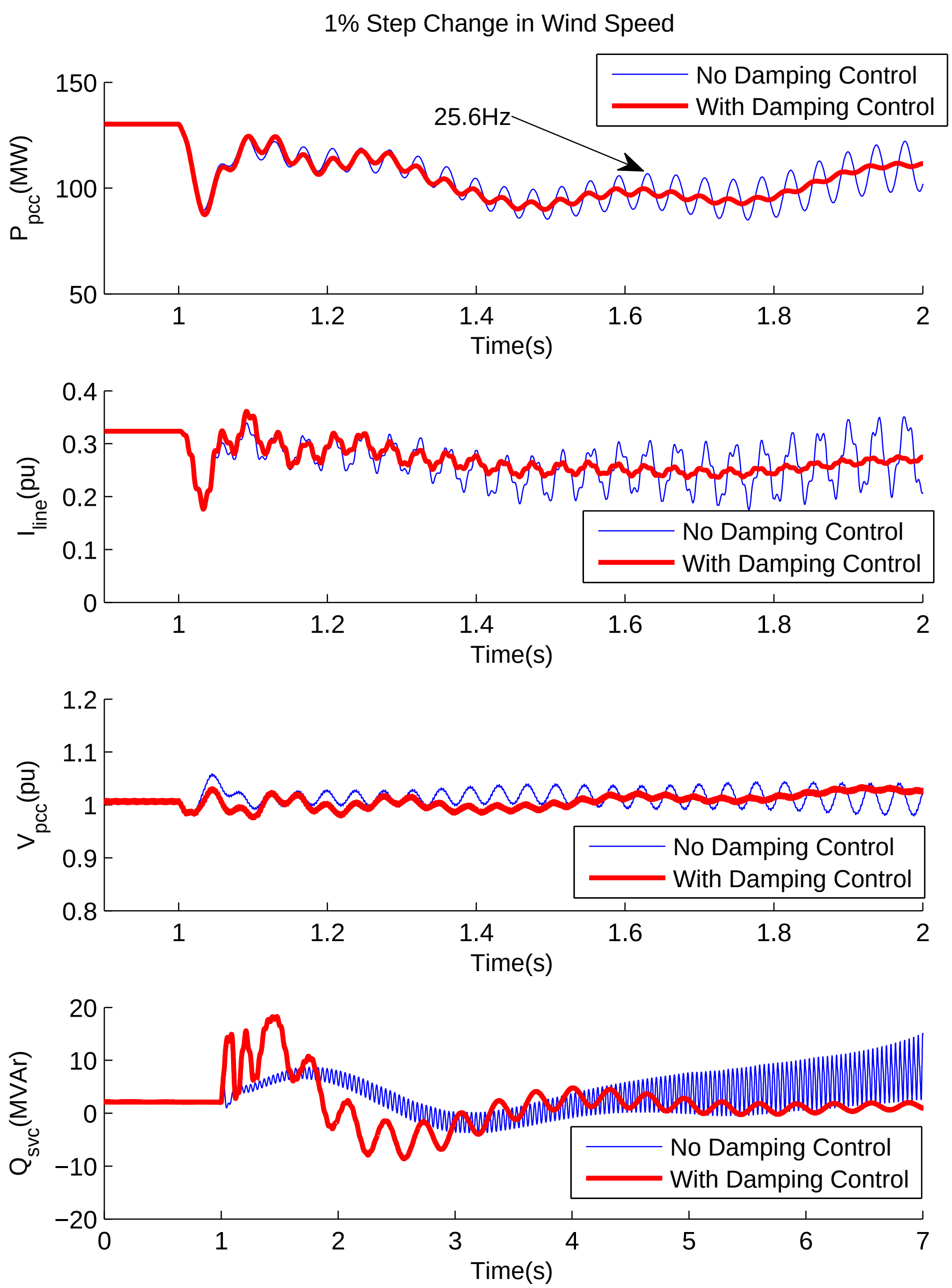

Figure 5.10: Response of the wind power plant for a 1% step change in wind speed

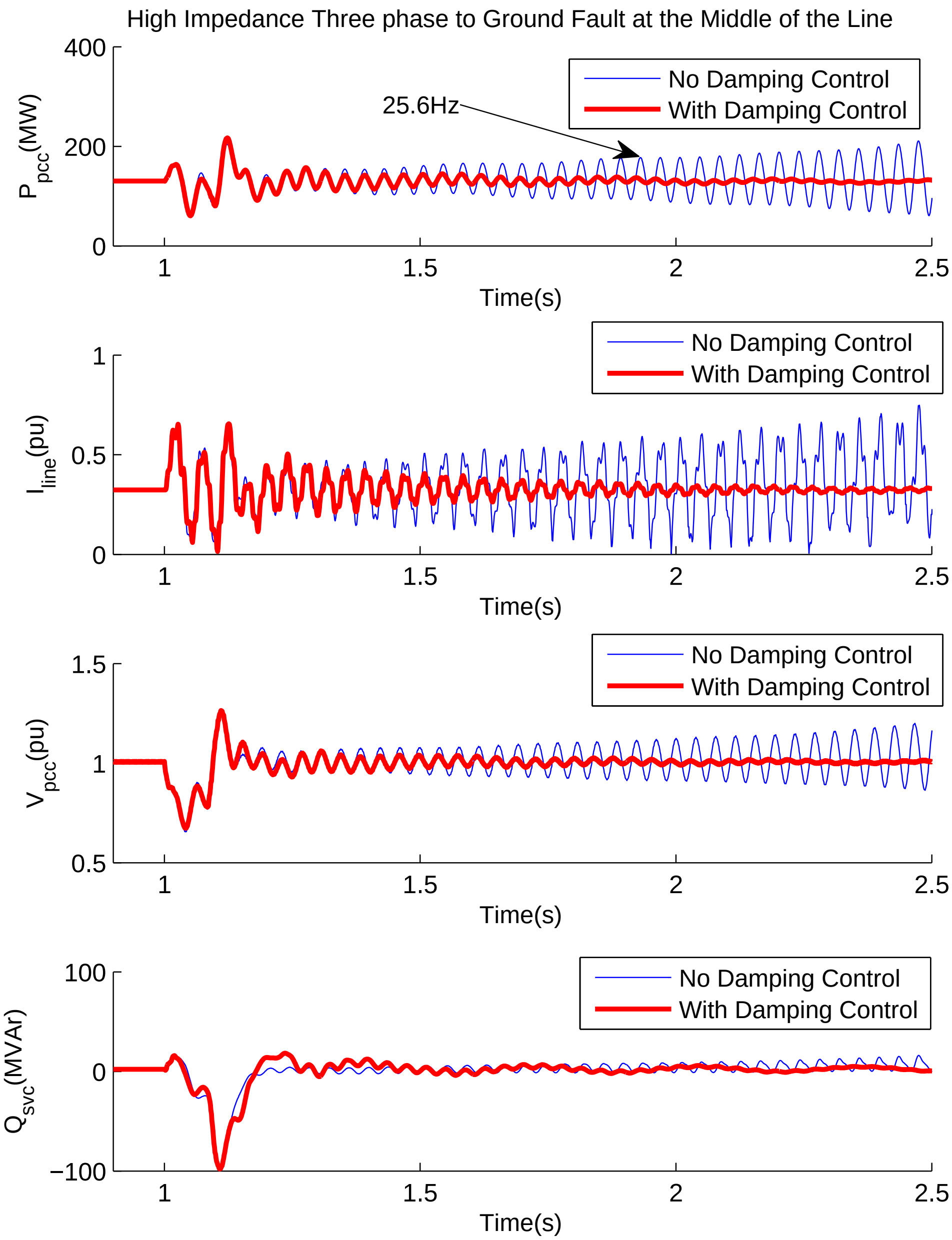

Figure 5.11: Response of the wind power plant to a high impedance three phase to ground fault at the middle of the line

5.4.2 Mitigating SSI in the Multi-machine Power System

Recall that the sub-synchronous interaction mode present in the multi-machine power system presented in Section 5.3.2 has almost 6% damping during normal system operation. However, the damping of the sub-synchronous interaction mode reduces to -2.61% of the wind power plant is radially operated with the series compensated line following a tripping of Line 1-6. In order to improve the damping of the sub-synchronous oscillations induced due to the interaction of the wind power plant generator with the series compensated line, an SVC is connected at the low voltage side of the point of common coupling transformer.

The damping of the sub-synchronous and super-synchronous mode after connecting the SVC is shown in Table 5.5. The connection of the SVC further improves the damping of the sub-synchronous mode in the system intact case. Although the SVC improves the damping of the sub-synchronous mode during the contingency, the improvement is not sufficient to obtained the desired 2% damping. An important trait of the SVC is that, it reduces the damping of the super-synchronous mode from 4.46% to 4.33% for the system intact case and from 6.22% to 6.07% for the selected contingency case.

Table 5.5: Frequency and damping of the sub-synchronous and super synchronous modes with the SVC (with out the damping controller)

Mode	System Intact		Line 1-6 Tripped	
	f (Hz)	ζ (%)	f (Hz)	ζ (%)
Sub-synchronous	19.77	7.09	22.75	-1.54
Super-synchronous	99.24	4.33	95.32	6.07

A supplemental damping controller as shown in Figure 5.8 is added to the SVC to improve the damping to the desired level. As with the single machine to infinite bus case, the PCC transformer current (I_{pcc}) and the active power flow through the PCC transformer (P_{pcc}) are selected as the candidate for the input signal to the damping controller. The residues of the sub-synchronous mode and the super-synchronous mode with the two candidate input signals are shown in Table 5.6. The higher residues indicate that selecting any one of the two signals would require a small input gain for the damping controller.

Table 5.6: Residues of the sub-synchronous and super-synchronous mode

Mode	Selected Signal	
	I_{pcc}	P_{pcc}
Sub-synchronous	$31.38\angle-178.54^0$	$30.11\angle156.74^0$
Super-synchronous	$31.55\angle-179.78^0$	$31.95\angle172.73^0$

As in the simple test system case, a measuring time constant of 0.02 s and a washout time constant of 0.01 s is used. If I_{pcc} is used as the input signal the phase compensation blocks in the damping controller is required to provide a 34.23^0 phase lead which is achieved by a single phase lead block with T_1=0.011 s and T_2=0.003 s. If P_{pcc} is used then the required phase lead is 59^0 which is provided by a single phase lead block with T_1=0.0166 s and T_2 = 0.001 s. The damping controller gain required for I_{pcc} or P_{pcc} as input is 0.3482 or 0.2438, respectively.

Table 5.7: Impact of the damping controller on some critical modes

Mode	No Damp. Control		P_{pcc} Input		I_{pcc} Input	
	f(Hz)	ζ(%)	f(Hz)	ζ(%)	f(Hz)	ζ(%)
Super-Sync.	95.32	6.07	95.72	6.87	95.73	6.30
SVC 63Hz	63.52	5.57	63.55	5.73	63.57	5.64
SVC 54Hz	54.19	9.50	54.12	9.11	54.06	9.34
Sub-sync.	22.75	-1.54	22.37	1.86	22.74	2.09
Electromechanical	10.89	53.16	11.12	54.12	11.30	52.68
Torsional	3.15	3.91	3.15	4.04	3.15	4.10

Table 5.7 shows the impact of the damping controller on the oscillatory modes in the system with less than 10% damping. These modes are the sub-synchronous

interaction mode and its corresponding super-synchronous mode, two SVC modes with frequencies of 63 Hz and 54 Hz and a torsional mode. The damping controller moved pole corresponding to the electromechanical mode in the simple test system case presented in Section 5.4.1. Therefore, the impact of the damping controller on the electromechanical mode is also shown in Table 5.7. The sub-synchronous damping controller does not significantly alter the damping of the oscillatory modes except for the intended sub-synchronous interaction mode. The damping of the sub-synchronous interaction mode is improved to 1.86% when using P_{pcc} as the damping controller input whereas it is improved to 2.09% when I_{pcc} is used as the damping controller input.

Note that in simple test system case as well as multi-machine power system case, the sub-synchronous damping controller designed using the parameters obtained using the residue analysis do not improve the damping of the intended mode to 2% exactly. Recall that the calculation of the gain is based on assumptions that the movement of the eigenvalue is small and the change in frequency is zero. However, when an eigenvalue is moved further away from its original location, the frequency of the mode also gets changed as shown below.

To improve the damping from -1.54% to 2% the eigenvalue needs to be moved by a distance of 5.0627. Figure 5.12 shows the actual position of the eigenvalue corresponding to the sub-synchronous interaction mode and its desired locations. For example, the two circled points furthest to the left represent the desired location of the eigenvalue in order to have 5% damping and the actual location of the eigenvalue after the damping controller was added. It can be seen from the Figure 5.12 that when the eigenvalue need not to be moved further away from its original location, the actual final location of the eigenvalue is almost the same as the desired location.

However, as the eigenvalue is moved further away from its original location, the separation between the actual and desired locations becomes larger. As it is moving further away, there is a deviation in both real and imaginary parts of the eigenvalue. This attributes to the difference in actual damping of the SSI mode from the desired damping.

Therefore, the residue based sub-synchronous interaction damping controller tuning method can be used to obtain a good estimate of the required damping controller gain. In order to achieve the desired damping exactly, the gain needs to be fine tuned.

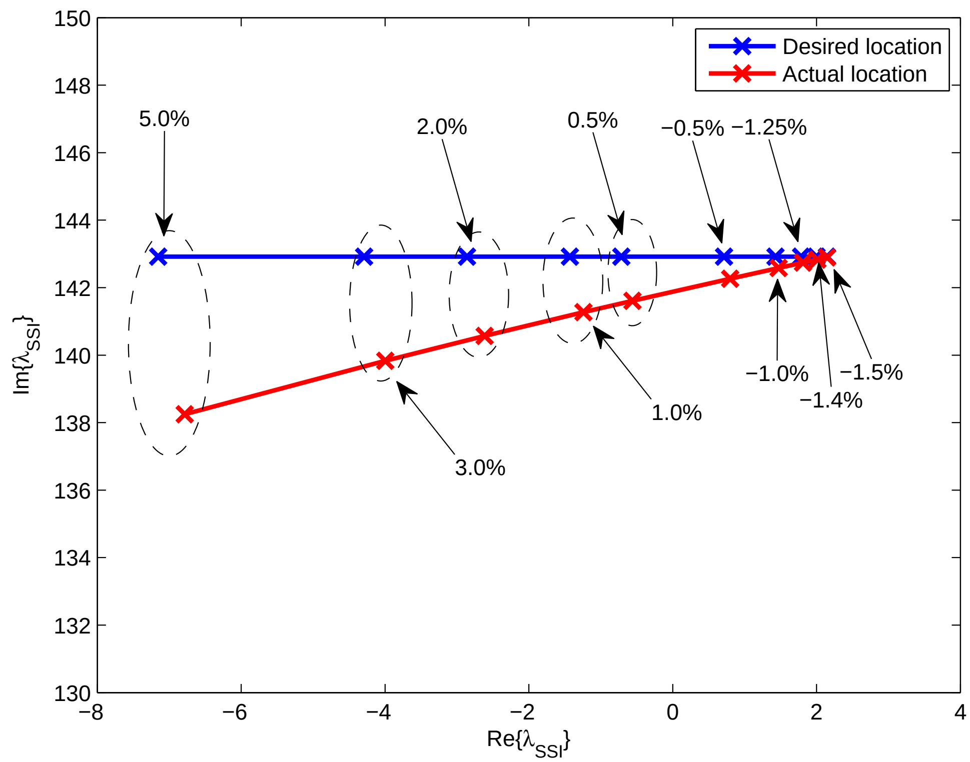

Figure 5.12: The actual position of the eigenvalue corresponding to the SSI mode and its corresponding desired locations

Note that the sub-synchronous damping controller presented in this section was designed based on the selected N-1 contingency where Line 1-6 is out of service.

The system intact case is also tested with the designed sub-synchronous damping controller. In this case the damping of the sub-synchronous interaction is improved from 7.09% to 8.45% without significantly affecting the other modes present in the system. Apart from the sub-synchronous interaction mode, the maximum deviation of the damping is observed in the 63 Hz SVC mode where its damping was increased by 1.9% from 6.23% to 8.12%. The change in the damping of the super-synchronous mode, the 54 Hz SVC mode, the electromechanical mode and the torsional mode are less that 0.7%.

The performance of the designed sub-synchronous damping controller is evaluated using electromagnetic transient simulations. Figures, 5.13 and 5.14 shows the performance of the wind power plant with the damping controller installed SVC for a 1% step change in wind speed and when the Line 1-6 is tripped following a three phase to ground fault, respectively. During the system intact case, the oscillations produced by the sub-synchronous interaction between the wind power plant generator and the series compensated line is well damped and therefore, the effect of the sub-synchronous damping controller is not visible. However, during the contingency, the sub-synchronous damping controller damp outs the otherwise undamped sub-synchronous interaction oscillations. Without the damping controller the frequency of the sub-synchronous oscillations is 22.37 Hz which is very close to the corresponding mode frequency (22.75 Hz) given by the small signal stability analysis. Note that similar to the small test system case previously presented, the sub-synchronous damping controller takes few cycles to start acting.

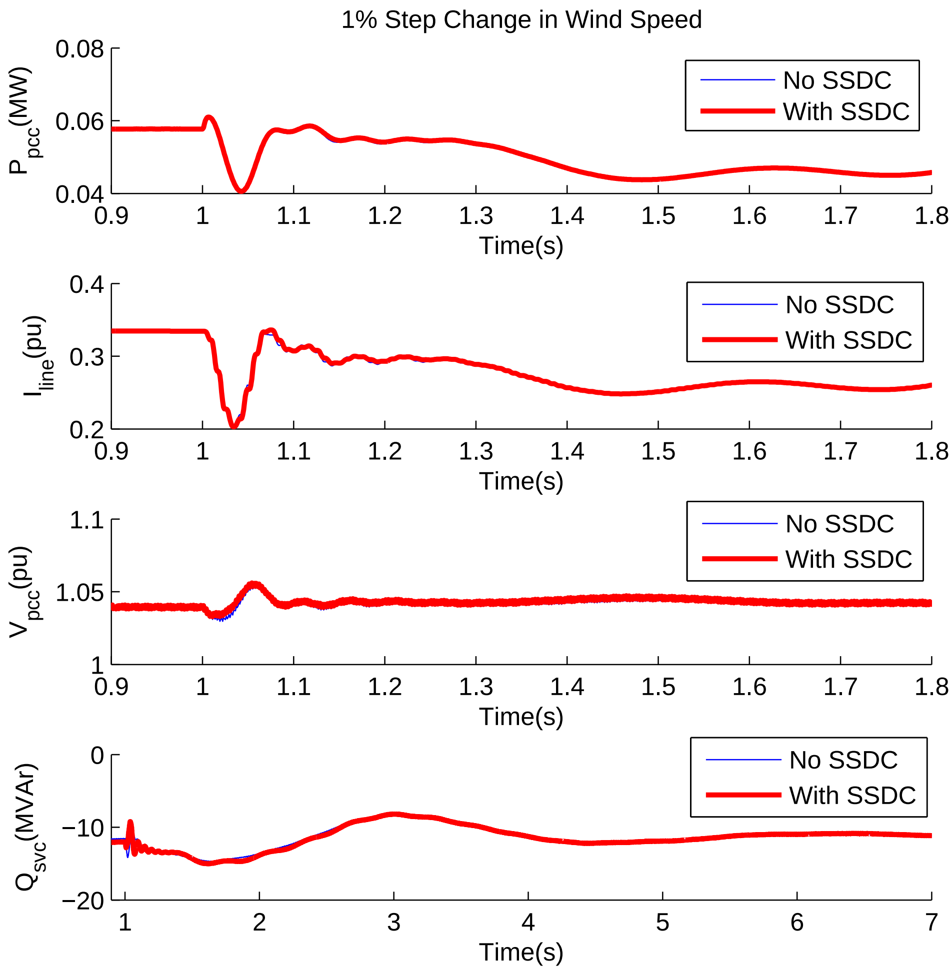

Figure 5.13: Response of the wind power plant for a 1% step change in wind speed

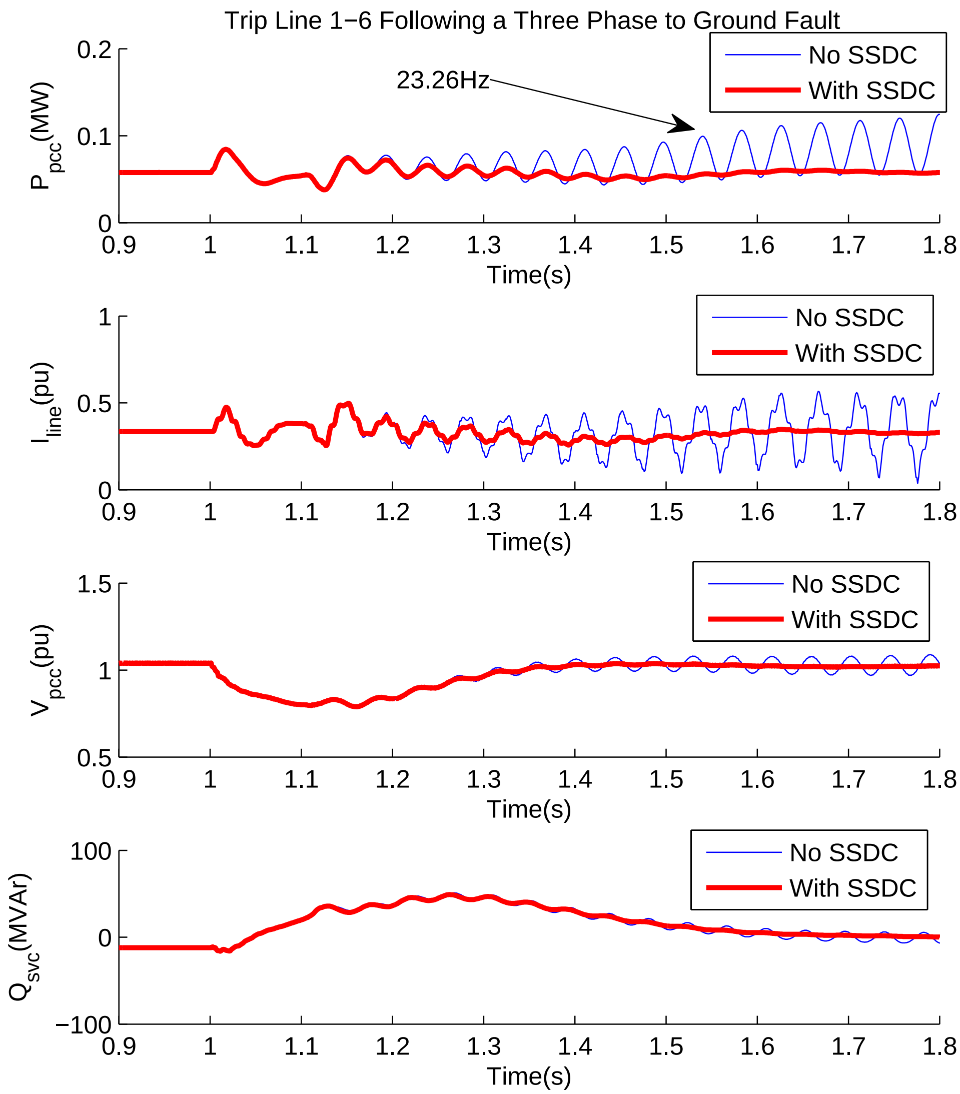

Figure 5.14: Response of the wind power plant when Line 1-6 is tripped following a three phase to ground fault

5.5 Damping of SSI using a Static Synchronous Compensator (STATCOM)

Similar to using an SVC, in this case a STATCOM is connected to the low voltage side of the PCC transformer to damp the sub-synchronous interaction present in the single machine to infinite bus system system shown in Figure 5.1. The STATCOM is used in voltage control mode and no energy storage device has been connected to the STATCOM. Therefore, it does not have active power control capability and the remaining degree of freedom available in the STATCOM controller is used to control the dc capacitor voltage. A detailed description of the STATCOM and its linearized model is given in Appendix C. Also, Appendix C includes the electrical system and controller parameters of the STATCOM used for this work.

When a 75 MVAr STATCOM is added to the low voltage side of the PCC transformer, the damping of the sub-synchronous interaction mode improves from -3.35% to 3.83%. In this case, a supplemental damping controller on the STATCOM is not required. Recall that the SVC was able to improve the damping only up to -1.53%. Figure 5.15 shows the participation factors of the sub-synchronous interaction mode with the SVC and with the STATCOM. The participation of the SVC electrical or controller states is very minimal. However, STATCOM controller states have a significant participation in the sub-synchronous interaction mode. Because of the higher participation, the STATCOM improves the damping of the SSI mode more than the SVC.

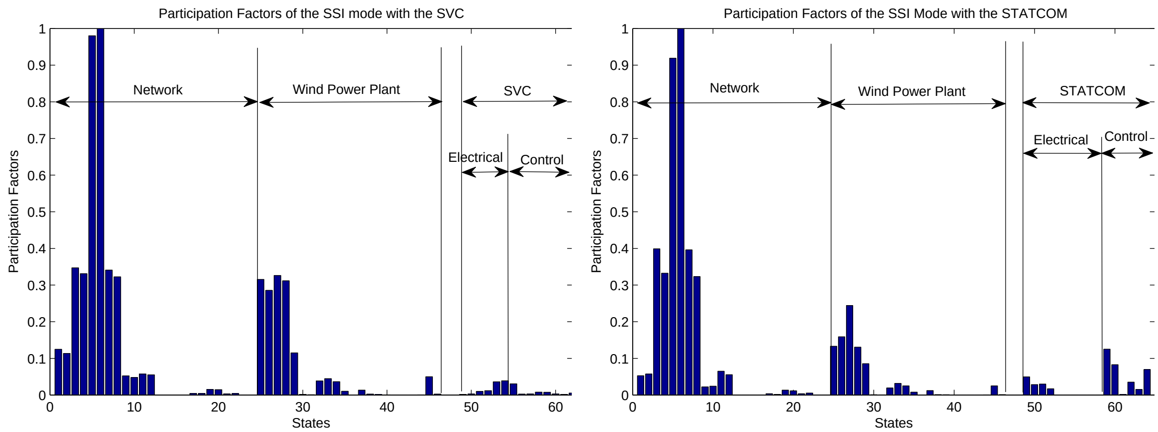

Figure 5.15: Participation factors of the SSI mode: Left - with SVC; Right - with STATCOM

The STATCOM controller states participating in the SSI mode corresponds to the ac voltage measurement filter, ac voltage controller outer-loop (to produce the q-axis current reference), ac voltage controller inner-loop (to produce the required modulation index), dc voltage measurement filter and the dc voltage controller. Figures 5.16 and 5.17 show the sensitivity of the SSI mode to the ac voltage measuring filter time constant (T_{mac}), ac voltage controller proportional gain (K_{pV}), ac voltage controller integrator time constant (T_{iV}), ac voltage controller inner current controller proportional gain (K_{pm}), ac voltage controller inner current controller integrator time constant (T_{im}), ac voltage controller droop (R), dc voltage measuring filter time constant (T_{mdc}), dc voltage controller proportional gain (K_{pdc})and dc voltage controller integrator time constant (T_{idc}). A smaller ac voltage inner current controller time constant, a smaller ac voltage measuring filter time constant, a higher ac voltage controller and inner current controller gains and a smaller droop value improves the damping of the sub-synchronous interaction mode. However, ac voltage controller time constant does not significantly impact on the damping of the SSI mode. Also, the dc voltage controller parameters have no significant impact on the damping of the sub-synchronous interaction mode.

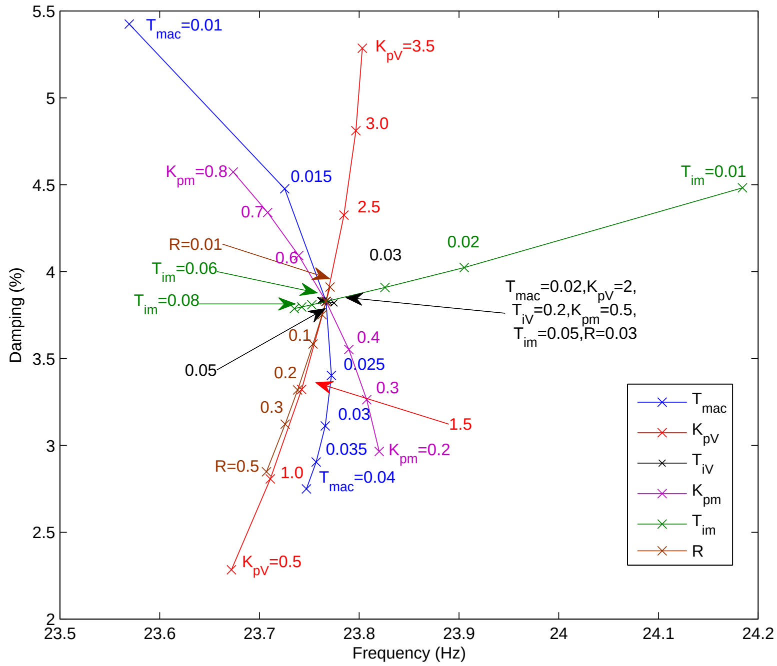

Figure 5.16: Sensitivity of the SSI mode to the STATCOM ac voltage controller parameters

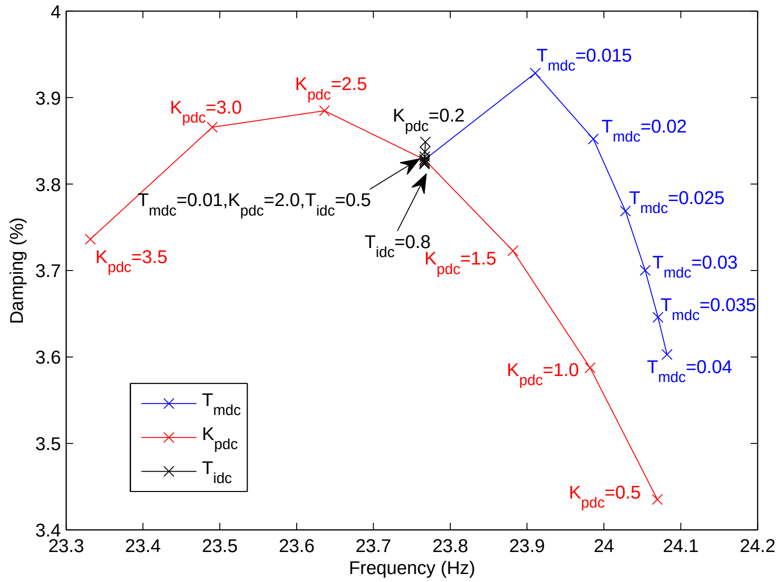

Figure 5.17: Sensitivity of the SSI mode to the STATCOM dc voltage controller parameters

Smaller measuring time constants, higher gains and smaller integral time constants are associated with faster PI controllers. Therefore, the sensitivity analysis results reveals that faster STATCOM ac voltage controller improves the damping of the SSI mode. Also, a faster ac voltage controller and smaller ac voltage droop can be interpreted as controlling the voltage at the point of common coupling strongly. Therefore, the sensitivity analysis results indicates that if the voltage at the wind power plant point of common coupling is controlled strongly, the damping of the subsynchronous interaction between the wind power plant and the series compensated line can be improved.

5.5.1 Electromagnetic Transient Simulation Results

Electromagnetic transient simulations are performed using PSCAD/EMTDC to confirm the results obtained using the small signal analysis and to check the robustness of the proposed method. Figure 5.18 shows the response of the wind power plant to a 1% step increase in wind speed with and without the STATCOM. The SSI oscillations damps out quickly when the STATCOM is present at the low voltage side of the point of common coupling transformer. Also note that the effect of the STATCOM can be seen almost immediately as the disturbance occurred, where as the effect of the SVC can be seen only about 100 ms after the disturbance occurred (see Figure 5.10). During the transient, the STATCOM reactive power varies between $\pm$ 5 MVAr.

Figure 5.19 shows the response of the wind power plant after a high impedance three phase to ground fault at the middle of the transmission line. The fault impedance was selected such that, the point of common coupling bus has 70% residual voltage during the fault. Undamped sub-synchronous oscillations are observed and the system is unstable without the STATCOM. However, after installing a STATCOM, the system becomes stable and the sub-synchronous oscillations damp out quickly. Recall that when using an SVC at the PCC, it needed to be equipped with a supplemental sub-synchronous damping controller to damp out the sub-synchronous interaction mode oscillations. Also note that when the system is recovering from the fault the STATCOM injects approximately 180 MVAr reactive power in to the system in order to recover the dropped terminal voltage due to the fault.

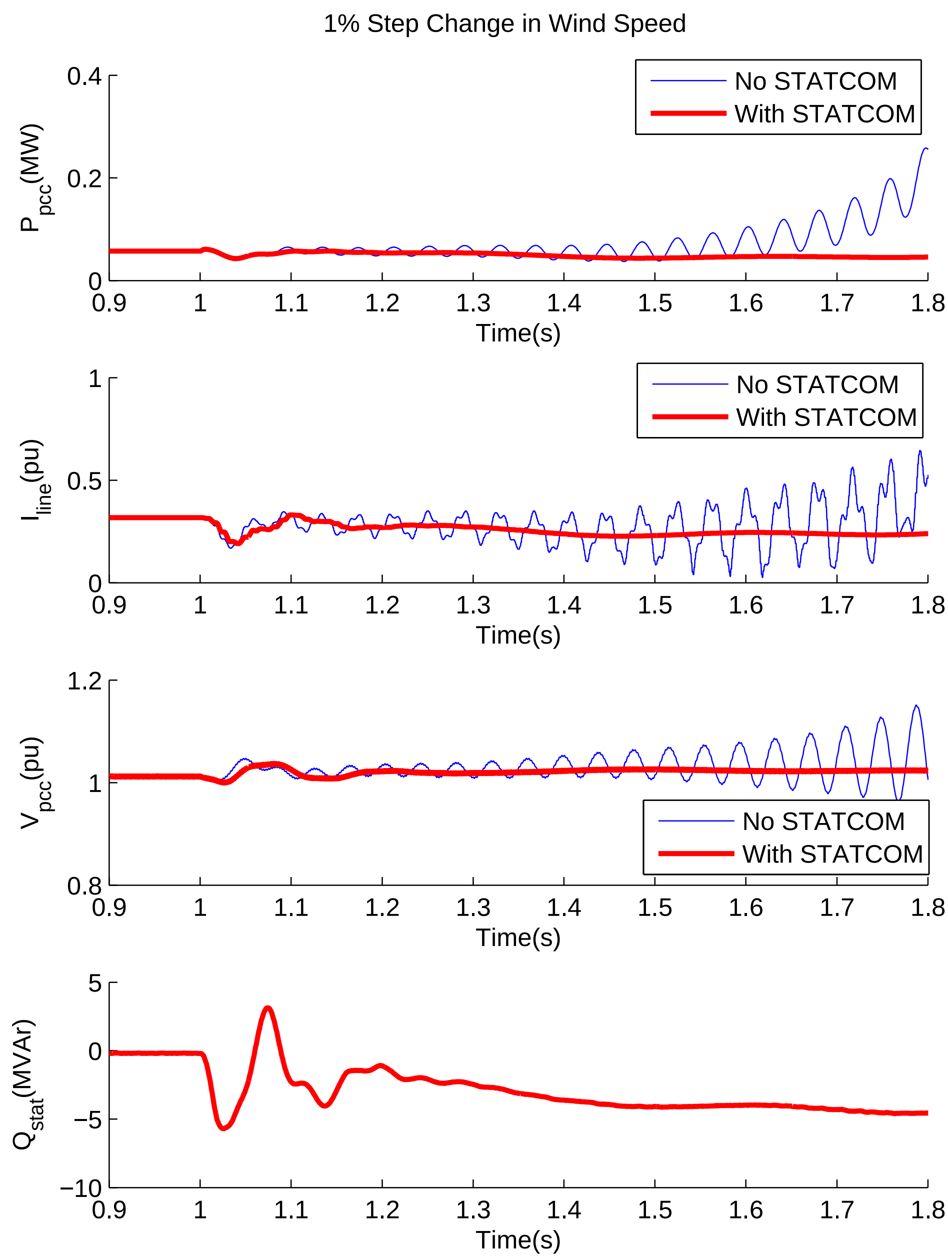

Figure 5.18: Response of the wind power plant for a 1% step change in wind speed

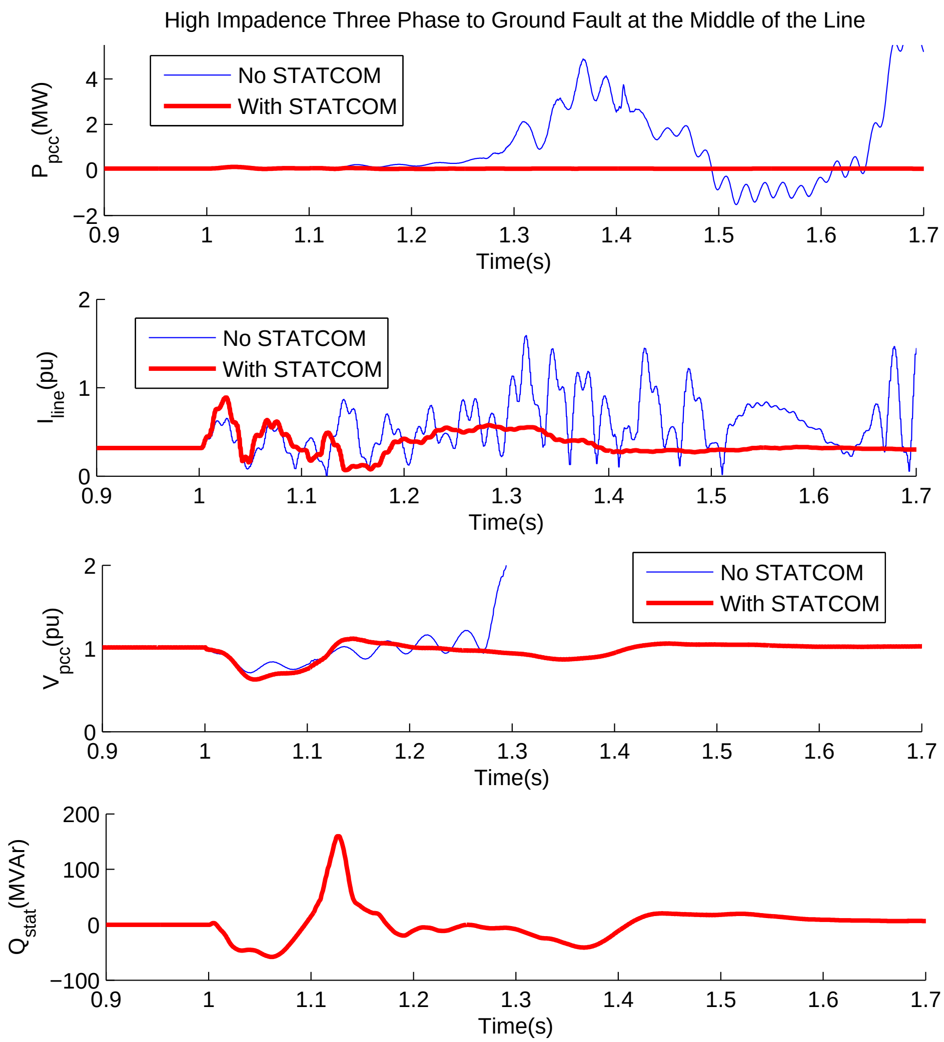

Figure 5.19: Response of the wind power plant to a high impedance three phase to ground fault at the middle of the line

5.5.2 Mitigating SSI in the Multi-machine Power System

Similar to the single machine to infinite bus case, a 75 MVAr STATCOM is connected to the low voltage side of the PCC transformer. All the STATCOM controller parameters are the same as in the previous case except the voltage controller inner current loop gain. For this case it is set to 0.1. Recall that for the multi-machine power system, the sub-synchronous interaction mode damping for the system intact case and the selected contingency is 5.90% and -2.61%, respectively. After connecting the STATCOM the damping of the sub-synchronous interaction mode for the system intact case improves to 9.23%. However, due to the connection of the STATCOM, the damping of the super-synchronous mode decreases from 4.46% to 3.42%. Although the super-synchronous mode damping is reduced it still has sufficiently high damping and therefore, the stability of the system is not compromised.

Figure 5.20 shows the response of the wind power plant with the system intact for a 1% step increase in wind speed. As predicted by the small signal stability analysis, the sub-synchronous oscillations induced due to the interaction of the wind power plant generator with the series compensated line are well damped with and without the STATCOM.

The connection of the STATCOM improved the damping of the sub-synchronous interaction mode to 3.68% when the Line 1-6 is out of service. While improving the damping the sub-synchronous interaction mode, the STATCOM reduces the damping of the super-synchronous mode from 6.22% to 3.32% during the contingency. As in the system intact case, the super-synchronous mode still have sufficiently hight damping so that the system stability is not affected.

The Figure 5.21 shows the response of the wind power plant when the Line 1-6 is tripped following a three phase to ground fault. When the STATCOM is not connected the contingency induces a negatively damped sub-synchronous oscillation at 22.73 Hz. The frequency of oscillation observed in the EMT simulation is very close to the sub-synchronous interaction mode frequency (22.53 Hz) given by the small signal stability analysis. When the STATCOM is connected to the low voltage side of the PCC transformer, the damping of the sub-synchronous interaction mode improves and the wind power plant can operate even with being radially connected with the series compensated line. Note that the damping of sub-synchronous oscillations does not cause additional burden to the STATCOM.

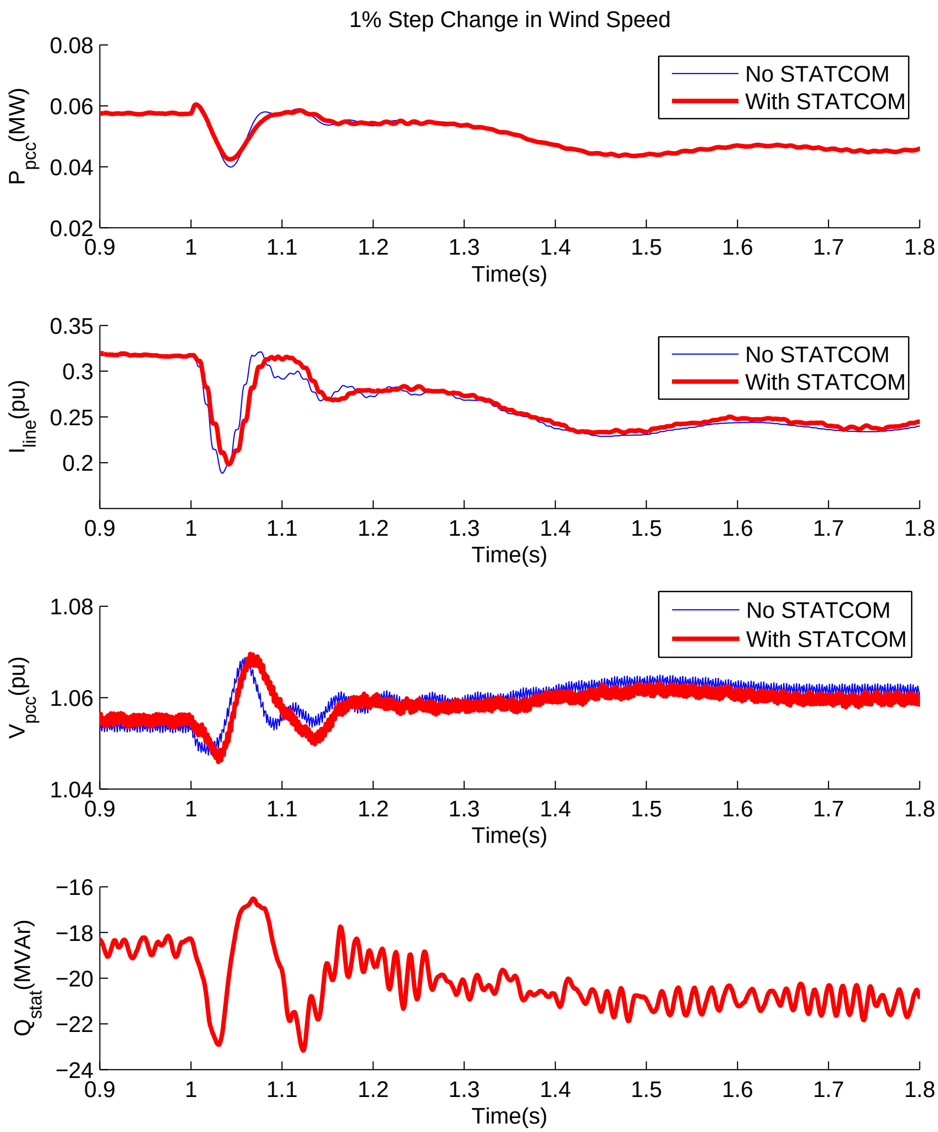

Figure 5.20: Response of the wind power plant for a 1% step change in wind speed

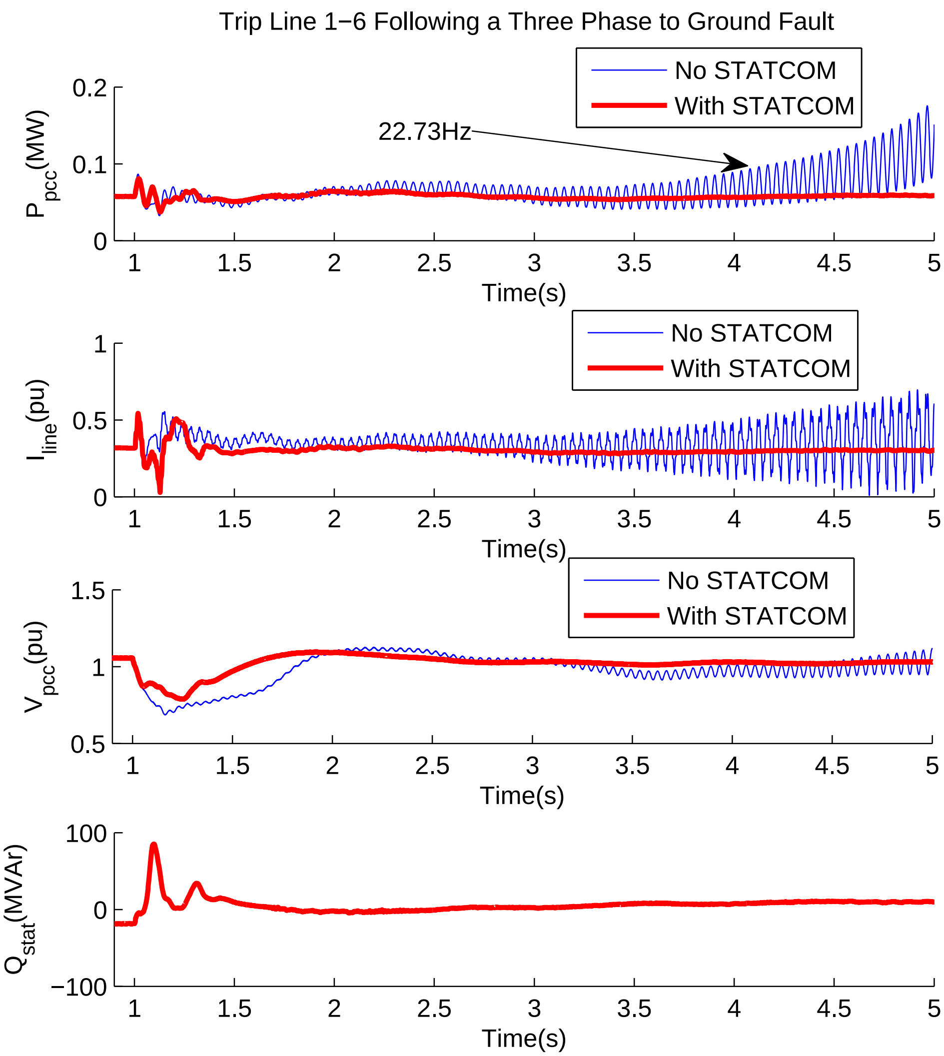

Figure 5.21: Response of the wind power plant when Line 1-6 is tripped following a three phase to ground fault

5.6 Comparison of STATCOM and SVC as a SSI Mitigation Device

In this chapter both a STATCOM and an SVC are used as sub-synchronous oscillations damping device. The main advantage of a SVC over a STATCOM is its relatively low cost. On the other hand the STATCOM has the advantage of requiring less amount of station footprint because of the absence of bulkier passive devices such as reactors and capacitors.

Table 5.8 shows a comparison of the damping of the sub-synchronous interaction mode with the SVC and with the STATCOM connected at the low voltage side of the point of common coupling transformer. As shown the table the STATCOM provides more damping for the sub-synchronous mode than the SVC. A properly tuned sub-synchronous damping controller can improve the damping for the sub-synchronous mode provided by the SVC.

Table 5.8: Impact of the SVC and the STATCOM on the SSI mode damping

Case	Base Case	SVC		STATCOM
		No SSDC	With SSDC	
SMIB	-3.35%	-1.53%	2.05%	3.83%
12 Bus - System intact	6.22%	7.09%	8.45%	9.23%
12 Bus - Line 1-6 tripped	-2.61%	-1.54%	1.86%	3.68%

Figure 5.22 shows the comparison of the performance of the SVC and the STATCOM in damping the sub-synchronous oscillations induced due to the interaction between the wind power plant generator and the series compensated line. The results are obtained by applying a 1% step increase in the wind speed for the small test system. When using the SVC for approximately 100 ms immediately after the disturbance, the effect of the damping controller is not visible. However, the STATCOM starts improving the damping of the SSI mode almost immediately after the

disturbance.

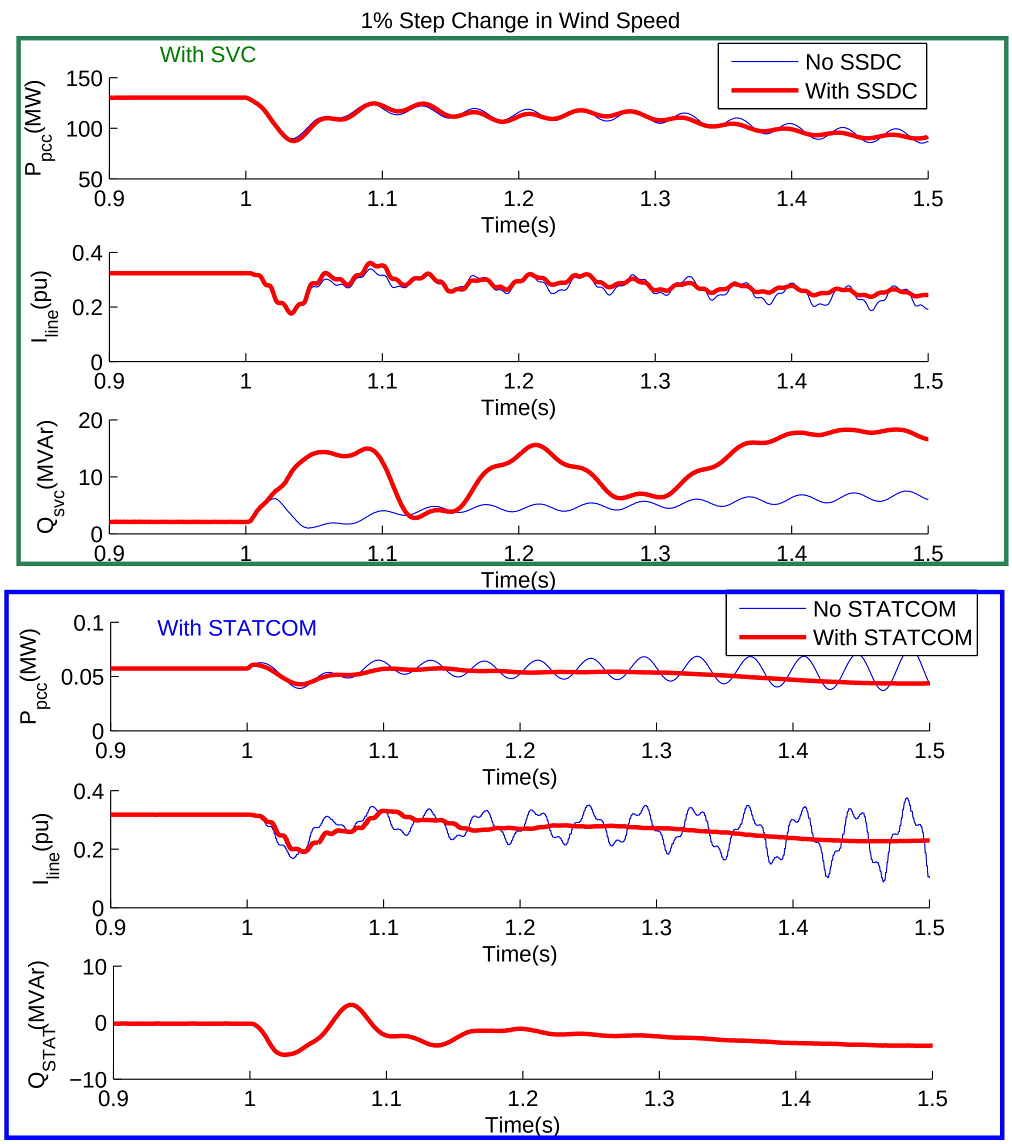

Figure 5.22: Performance of the SVC and the STATCOM in damping SSI induced due to a 1% step increase in wind speed - simple test system

The delay in sub-synchronous damping controller response is possibly attributed to the inherently slower response of the SVC due to the usage of the reactors and capacitors. On the other hand, the STATCOM uses fast electronic switching to provide the reactive power support. Therefore, the STATCOM can respond to the disturbance much quicker than an SVC. Thus, the STATCOM responds faster in improving the damping of the sub-synchronous interaction mode.

Table 5.9: Impact of the SVC and the STATCOM on the super-synchronous mode damping

Case	Base Case	SVC		STATCOM
		No SSDC	With SSDC	
SMIB	6.39%	5.82%	5.85%	2.98%
12 Bus - System intact	4.46%	4.33%	4.61%	3.42%
12 Bus - Line 1-6 tripped	6.22%	6.07%	6.87%	3.32%

A STATCOM has the potential of reducing the damping of the super-synchronous mode. Table 5.9 shows the damping of the super-synchronous mode observed in the three cases presented in this chapter with the SVC and with the STATCOM connected at the low voltage side of the PCC transformer. As shown in Table 5.9, unlike the STATCOM the SVC with the sub-synchronous damping controller does not significantly alter the damping of the super-synchronous mode. In fact, it slightly improves the damping of the super-synchronous mode in some cases.

Although the STATCOM reduces the damping of the super-synchronous mode, its still has almost 3% damping so that the stability of the system is not compromised.

5.7 Conclusions

A network-based sub-synchronous interaction mitigation method has been proposed in this chapter. An SVC or a STATCOM connected at the low voltage side of the point of common coupling transformer has been utilized to improve the damping of the sub-synchronous interaction mode. The advantage of this method is that the connected device can provide voltage support at the PCC bus in addition to the sub-synchronous interaction damping. A supplemental sub-synchronous damping controller was required when using the SVC. The small signal stability analysis results has been used to design the supplemental damping controller.

The input signals for the damping controller and the damping controller parameters has been systematically selected using the controllability and observability indices and the residues. The damping controller gain required to move the eigenvalue correspond to the sub-synchronous interaction mode to a desired location has been obtained using the residues. It was shown that the calculated gain does not exactly move the eigenvalue to the desired location but it will serve as a good starting point for fine tuning. It was also shown that the designed damping controller can improve the damping of the sub-synchronous interaction mode without significantly altering the other modes present in the system.

A supplemental sub-synchronous damping controller was not required when using the STATCOM. It was shown that the damping of the sub-synchronous interaction mode can be improved by strongly controlling the voltage at the point of common coupling bus. The damping provided by the STATCOM for the sub-synchronous interaction mode was greater than the damping provided by the SVC with the supplemental damping controller. Also it has been shown that the response time of the SVC with the supplemental damping controller in damping the sub-synchronous interaction mode is slower compared to the STATCOM. Therefore, it can be concluded that a STATCOM provides better sub-synchronous interaction damping than an SVC equipped with a supplemental damping controller.

In all the cases in this chapter the STATCOM reduced the damping of the super-synchronous mode. Although this could be a system specific issue, it is recommended to be careful about the reduction in damping of the super-synchronous mode when connecting a STATCOM to a Type 3 wind power plant connected to a series compensated power system.

The robustness of the proposed designs presented in this chapter has been investigated using electromagnetic transient simulations.

Chapter 6

Conclusions, Contributions and Future Work

.

6.1 General Conclusions

A comprehensive procedure to analyze sub-synchronous interactions present in power systems with Type 3 wind power plants and series compensated lines has been proposed in this thesis. The proposed procedure includes a combination of frequency scan, small signal analysis and electromagnetic transient simulations. Using the proposed procedure it was shown that the sub-synchronous interaction between a Type 3 wind power plant and a series compensated line is caused by the interaction between the wind power plant generator and the series compensated line. It has also been shown that the damping of the oscillations caused by this interaction is highly sensitive to the rotor side converter current controller gains. Since small signal analysis is nucleolus of the analysis in this thesis, a detailed linearized model of the Type 3 wind power plant has been presented in this thesis. The developed linearized model has been validated against the electromagnetic transient simulations. Once the root cause of the sub-synchronous interactions has been identified a network based sub-synchronous interaction mitigation method has been proposed in this thesis. The advantage of the network based sub-synchronous interaction mitigation method is that it allows the network operators to develop their transmission networks independent of the development of the wind generation.

The modelling of wind integrated power systems for small signal stability analysis has been discussed in detail in Chapter 2. The wind power plant model included the generator, drive train, rotor and grid side converter controllers, dc capacitor, converter transformer and the pitch controller models. To take the effects of the blade oscillations into account a three mass model has been used for the drive train. An aggregated model has been used to represent the hundreds of wind turbines in the wind power plant. To accurately capture the effects of sub-synchronous interactions, the ac network has been modelled using dynamic phasors.

The validation of the linearized model of the wind power plant has been presented in Chapter 3. The linearized models were validated by comparing with the electromagnetic transient simulations performed using PSCAD/EMTDC. The results presented confirmed that the non-linear system equations for the wind power plant and the ac network can be linearized around a steady state operating point without affecting the accuracy of the simulation.

The comprehensive procedure proposed to study sub-synchronous oscillations in power systems with Type 3 wind power plants and series compensated transmission lines was presented in Chapter 4. As the first step in the proposed procedure, frequency scanning has been performed to identify the presence of network resonances.

The use of a conventional induction generator equivalent circuit has been compared against a more accurate equivalent circuit and it was shown that the conventional equivalent circuit is adequate. It has been shown that, if a network resonance is revealed in the first step, it is essential to perform a detailed eigenvalue analysis regardless of whether the net resistance seen by the generator rotor is negative or positive. The proposed detailed analysis clearly identifies the participating state variables, and the controllability of the sub-synchronous oscillation mode. The sensitivity studies performed resulted in following conclusions.

- Higher RSC controller current loop gains reduce the damping of the network mode. They do not have a significant impact on the frequency of the network mode.
- Higher stator reactive power controller gains reduce the damping of the network mode. No significant impact on the frequency of the network mode.
- Rotor speed controller gains do not have a significant impact on either the network mode frequency or damping.
- Both inner and outer loop GSC gains do not have a significant impact on either the network mode frequency or damping.
- Increased

  i line length,

  ii compensation level, and

  iii wind power plant size

  decreases the network mode frequency.

- Increased line length, wind power plant size improves the network mode damping.
- Increased compensation level decreases the network mode damping.
- Increased wind speed improves the network mode damping. No significant impact on the network mode frequency.

The aforementioned conclusions on the sub-synchronous interactions have been further verified using multi-machine case studies. The results have also been verified using electromagnetic transient simulations. The network based sub-synchronous interaction mitigation method has been proposed in Chapter 6. An SVC or a STATCOM connected at the low voltage side of the point of common coupling transformer has been utilized to improve the damping of the sub-synchronous interaction mode. The advantage of this method is that the connected device can provide voltage support at the PCC bus in addition to the sub-synchronous interaction damping. A supplemental sub-synchronous damping controller was required when using the SVC. The small signal stability analysis results has been used to design the supplemental damping controller.The input signals for the damping controller and the damping controller parameters has been systematically selected using the controllability and observability indices and the residues. The damping controller gain required to move the eigenvalue correspond to the sub-synchronous interaction mode to a desired location has been obtained using the residues. It was shown that the calculated gain does not exactly move the eigenvalue to the desired location but it will serve as a good starting point for fine tuning. It was also shown that the designed damping controller can improve the damping of the sub-synchronous interaction mode without significantly altering the other modes present in the system. A supplemental sub-synchronous damping controller was not required when using the STATCOM. It was shown that the damping of the sub-synchronous interaction mode can be improved by strongly controlling the voltage at the point of common coupling bus. The damping provided by the STATCOM for the sub-synchronous interaction mode was greater than the damping provided by the SVC with the supplemental damping controller. Also it has been shown that the response time of the SVC with the supplemental damping controller in damping the sub-synchronous interaction mode is slower compared to the STATCOM. Therefore, it can be concluded that a STATCOM provides better sub-synchronous interaction damping than an SVC equipped with a supplemental damping controller. In all the cases in Chapter 6 the STATCOM reduced the damping of the super-synchronous mode. Although this could be a system specific issue, it is recommended to be careful about the reduction in damping of the super-synchronous mode when connecting a STATCOM to a type 3 wind power plant connected to a series compensated power system.

6.2 Contributions

The main contributions of the work presented in this thesis are as follows.

- A comprehensive procedure to study sub-synchronous interactions in power systems with Type 3 wind power plants and series compensated lines was proposed. The proposed method includes a combination of frequency scan, small signal analysis and electromagnetic transient simulation. The root cause of the sub-synchronous interaction present can be systematically and efficiently identified using the proposed method.

- The adequacy of the conventional induction generator equivalent circuit when performing the frequency scans for Type 3 wind power plants were demonstrated.

- The root cause of the sub-synchronous interaction in a power systems with Type 3 wind power plants and series compensated transmission lines was clearly identified. It was shown that the sub-synchronous interaction in such systems were caused by the interaction between the wind power plant generator electrical system and the series capacitor. It was also shown that this mode is highly controllable through the rotor side converter current controller.

- A network based sub-synchronous interaction mitigation method was proposed. The performance of an SVC and a STATCOM in improving the damping of the sub-synchronous interaction mode was evaluated. It was shown that the damping of the oscillations produced by the sub-synchronous interaction can be improved by strongly controlling the point of common common coupling voltage.

- A small signal stability analysis based method has been proposed to design a sub-synchronous damping controller for an SVC. The input signals for the damping controller and the damping controller parameters can be systematically selected when using the small signal analysis based design.

The aforementioned contributions have led to the following publications.

- D.H.R. Suriyaarachchi, U.D. Annakkage, C. Karawita and D.A. Jacobson, ”A Procedure to Study Sub-Synchronous Interactions in Wind Integrated Power Systems”, IEEE Trans. Power Syst., vol. 28, no. 1, pp. 377-384, Feb. 2013.

- D.H.R. Suriyaarachchi, U.D. Annakkage, C. Karawita, D. Kell, R. Mendis, and R. Chopra, ”Application of an SVC to damp sub-synchronous interaction between wind farms and series compensated transmission lines", IEEE PES General Meeting, San Diego, CA, USA, July 22-26, 2012.

- D.H.R. Suriyaarachchi, C. Karawita, D. Kell and U.D. Annakkage, "Understanding Sub-synchronous Interactions in Power Systems using Dynamic Phasor Based Small Signal Stability Analysis", 2012 CIGRÉ Canada Conference, Montréal, QC, Canada, Sept. 24-26, 2012.

6.3 Recommendations for Studying Sub-synchronous Interactions in Wind Integrated Power Systems

Based on the findings of this research, the following recommendations will be proposed for studies related to sub-synchronous interactions in wind integrated power systems.

- If series compensated transmission lines and Type 3 wind power plants are located electrically close to each other, a detailed sub-synchronous interaction study needs to be performed.

- It is recommended to used the proposed procedure involving frequency scan, small signal analysis and electromagnetic transient simulation when studying wind integrated power systems for sub-synchronous interactions. As shown in this thesis, the proposed procedure pin points the root cause of the problem efficiently and effectively.

- The black-box models of the wind turbine generators are widely used in the wind industry. These back-box models hide the wind turbine manufacturers valuable proprietary information. Because of the limited access to the wind turbine-generator model data it is difficult to properly do a detailed sub-synchronous interaction analysis. Also, at the pre-specification stage of a project where the sub-synchronous interaction studies are usually performed, the project owner may have not finalized a specific manufacturer and in such cases the black-box models provided by the manufacturers may not be available. Therefore, it is recommended to develop a generic Type 3 wind turbine-generator model to be used in pre-specification studies. The generic model should have the turbine and generator data of a typical Type 3 unit and it is important that it should reveal the basic structure and typical parameters of the higher level converter controllers, especially the outer and inner loop PI controllers. As shown in Chapter 4, the sub-synchronous interaction is highly sensitive to these controller parameters. The other details of the model such as signal conditioning, protection, other details of the controllers can still be black-boxed. As shown in Chapter 4, since there is no possibility to have a sub-synchronous torsional interaction, it is sufficient to model the turbine and the drive train with a two-mass or three-mass model with generic data.

6.4 Suggestions for Future Work

Wind power plant can interact with other devices in the power system. The proposed procedure in this thesis can be used to analyze sub-synchronous interactions with other devices in the power systems. Some suggestions for further research are given below.

- HVdc converter controllers can produce high frequency oscillations. These oscillations may interact with a Type 3 wind power plant converter controller if a wind power plant is located in a close proximity to the HVdc station. A combination of small signal analysis and electromagnetic transient simulation can be used to study a HVdc and wind power plant interactions.

- The scope of research has been limited to Type 3 wind power plant in this thesis. However, there are other types of wind power plants connected to the power systems. The other commonly used type of wind power plant are Type 4 wind power plants. Since the wind turbine and the generator are decoupled from the external ac system by the converter in front of the unit, a turbine-generator interaction with the rest of the power system is highly unlikely. However, still there can be converter controller interaction with the devices in the external power system. Therefore, it is important to investigate the possibility of having such controller interactions in Type 4 power plants.

- In this thesis it has been shown that the sub-synchronous interaction between a Type 3 wind power plant and a series capacitor can be mitigated by strongly controlling the point of common coupling voltage. Since Type 4 wind power plant in essence behave as a voltage source converter it would be interesting to investigate the impact of having a Type 4 wind power plant in a close proximity to a Type 3 wind power plant and a series compensated transmission line. Also, further investigations can be carried out to investigate the impact on sub-synchronous interactions if a wind power plant is consisting of a mix of Type 3 and Type 4 units.

- A modified version of the IEEE first benchmark model for sub-synchronous resonance studies and IEEE 12 bus system proposed in [53] used in this thesis. Also, it has been shown using an actual heavily meshed power system with a number of series compensated lines and Type 3 wind power plants, sub-synchronous interactions between wind power plant and the series compensated line are possible even without the wind power plant being radially connected to a series compensated line. Therefore, a development of a benchmark test system to study sub-synchronous interactions in wind integrated power system would be highly beneficial for future researchers.

Appendix A

Wind Power Plant and Network Data

A.1 Wind Power Plant Parameters

A.1.1 Wind Turbine Parameters

Table A.1: Wind Turbine Parameters

Parameter	Symbol	Value
Rated power	$P_{t,rated}$	2 MW
Blade length	R	37.5 m
Performance coefficient	C_p	0.28
Air density	ρ	1.225 kg/m^3
Wind speed/rotor speed	K_t	10.909

A.1.2 Generator Parameters

The generator parameters presented below are from [33].

Table A.2: Generator Parameters

Parameter	Symbol	Value
Rated Voltage	V_{rated}	690 V
Base MVA	S_0	2 MVA
Stator resistance	R_s	0.001164 Ω
Rotor resistance	R_r	0.00131 Ω
Stator leakage inductance	L_s	0.0584 mH
Rotor leakage inductance	L_r	0.0629 mH
Mutual inductance	L_m	2.4961 mH

A.1.3 DC Capacitor and Unit Transformer Parameters

Table A.3: DC Capacitor and Unit Transformer Parameters

Parameter	Symbol	Value
DC Capacitance	C_{dc}	25 mF
DC voltage	V_{dc}	1000 V
Converter transformer base	$S_{tf,conv}$	$0.3S_0$
Transformer leakage reactance	$X_{tf,conv}$	0.06 pu-Tf base

A.1.4 Drive Train Parameters

The three mass drive train parameters presented below are from [39].

Table A.4: Drive Train Parameters

Parameter	Symbol	Value
Blade inertia	H_b	4.00 s
Hub inertia	H_h	0.30 s
Generator inertia	H_g	0.42 s
Shaft stiffness constants	K_1, K_2	0.3 (pu Torure)/rad

A.1.5 Internal Network Parameters

Table A.5: Internal Network Parameters

Parameter	Symbol	Value
Internal network voltage	V_{MV}	33 kV
PCC Transformer MVA	S_{pcc}	200 MVA
PCC transformer leakage reactance	X_{pcc}	0.06 pu-Tf base
Internal network resistance	R_{int}	0.4713 Ω
Internal network reactance	X_{int}	0.7766 Ω
Internal network suceptance	B_{int}	5.42×10^{-4} S

Table A.6: Transmission Line Parameters

Parameter	Symbol	Value
Line resistance	R_l	0.05 Ω/km
Line inductance	L_l	1.30 mH/km
Line capacitance	C_l	0.0089 μF/km

A.2 Multi Machine Power System Parameters

A.2.1 Power Flow Data

Bus Data

Table A.7: Multi-machine System Bus Data

Bus number	Rated Voltage [kV]	Type
1	230.00	Non Generator
2	230.00	Non Generator
3	230.00	Non Generator
4	230.00	Non Generator
5	230.00	Non Generator
6	230.00	Non Generator
7	345.00	Non Generator
8	345.00	Non Generator
9	22.00	Slack
10	22.00	Generator
11	22.00	Generator
12	0.69	Wind Generator
61	230.00	Non Generator
62	230.00	Non Generator
121	33.00	Non Generator
122	33.00	Non Generator

Load Data

Table A.8: Multi-machine System Load Data

Bus number	P_{load} (MW)	Q_{load} (MVAr)
2	280.0	200.0
3	320.0	240.0
4	250.0	225.0
5	100.0	60.0

Generator Data

Table A.9: Multi-machine System Generator Data

Bus Number	P(MW)	Q(MVAr)	V(pu)	MVA
9	145.59	-155.885	1.04	200.000
10	500.000	198.133	1.02	588.000
11	200.000	74.391	1.01	235.000
12	130.13	30.000	1.00	200.000

Transmission Line Data

Table A.10: Multi-machine System Line Data

From Bus	To Bus	Id	R_{line} (pu)	X_{line} (pu)	B_{line} (pu)
1	2	1	9.37051E-3	9.14562E-2	0.17679
1	6	1	2.83555E-2	2.76749E-1	0.53499
2	5	1	1.98488E-2	1.93725E-1	0.37449
3	4	1	9.42820E-3	9.20189E-2	0.17788
3	4	2	9.42820E-3	9.20189E-2	0.17788
4	5	1	1.98490E-2	1.93725E-1	0.37449
4	62	1	1.41775E-2	1.38375E-1	0.26750
6	61	1	1.41780E-2	1.38375E-1	0.26750
7	8	1	1.55430E-2	1.54169E-1	2.68875
7	8	2	1.55430E-2	1.54169E-1	2.68875
61	62	1	0.00000E+0	-2.07563E-1	0.00000
121	122	1	4.32740E-2	7.13150E-2	0.00590

Transformer Data

Table A.11: Multi-machine System Transformer Data

From Bus	To Bus	MVA	X_{tf}(pu)
1	7	1000	0.1
1	9	100	0.01
2	10	600	0.1
3	8	1000	0.1
3	11	250	0.1
6	122	200	0.06
121	12	200	0.06

A.2.2 Dynamic Data

The dynamic data given in this section is in the form of PSS/E version 32 data format [57]. Note that the generator connected to Bus 9 is the slack generator and the wind generator is connected to Bus 12. Therefore the dynamic data for generators at Bus 10 and Bus 11 is presented. Both these generators are assumed to be round rotor type and therefore, they are represented by the PSS/E GENROU model.

Generator Data

Table A.12: Generator Dynamic Data - GENROU

Bus	T'_{d0}(s)	T''_{d0}(s)	T'_{q0}(s)	T''_{q0}(s)	H(s)	D (pu)	X_d (pu)
10,11	8.0	0.003	0.4	0.05	4.0	0.0	1.8
	X_q (pu)	X'_d (pu)	X'_d (pu)	$X''_d = X''_q$ (pu)	X_l (pu)	$S(1.0)$	$S(2.0)$
	1.7	0.3	0.55	0.25	0.2	0.03	0.4

Exciter Data

The generators at Bus 10 and Bus 11 are assumed to be equipped with IEEE type AC4 excitation system. Therefore it is represented using PEE/E ESAC4A model.

Table A.13: Excitation System Data - ESAC4A

Bus	T_R (s)	V_{IMAX} (kV)	V_{IMIN} (kV)	T_C (s)	T_B (s)
10,11	0.02	10.0	-10.0	1.0	10.0
	K_A	T_A (s)	V_{RMAX} (kV)	V_{RMIN} (kV)	K_C
	200	0.015	5.64	-4.53	0.0

Appendix B

Static Var Compensator Small Signal Model

Static Var Compensator (SVC) is a reactive power controlling device made with passive components which are usually controlled by a thyristor. There are many configurations of SVCs but the frequently used configuration consists of a thyristor controlled reactor (TCR) and a thyristor switched capacitor (TSC). The fast switching of the TCR generates harmonics of the fundamental frequency. Therefore, SVCs require filters to avoid distortions in terminal voltages and currents.

If the fast switching of the thyristor is neglected, an SVC can be assumed as a variable reactor and a capacitor in the modeling perspective. Therefore, the dynamics of the SVC is mainly governed by the dynamics of the capacitor and the controllable reactor. Also, the SVC dynamics depend on the dynamics of the SVC transformer, filters and the controllers. The schematic diagram of the SVC electrical circuit is shown in Figure B.1.

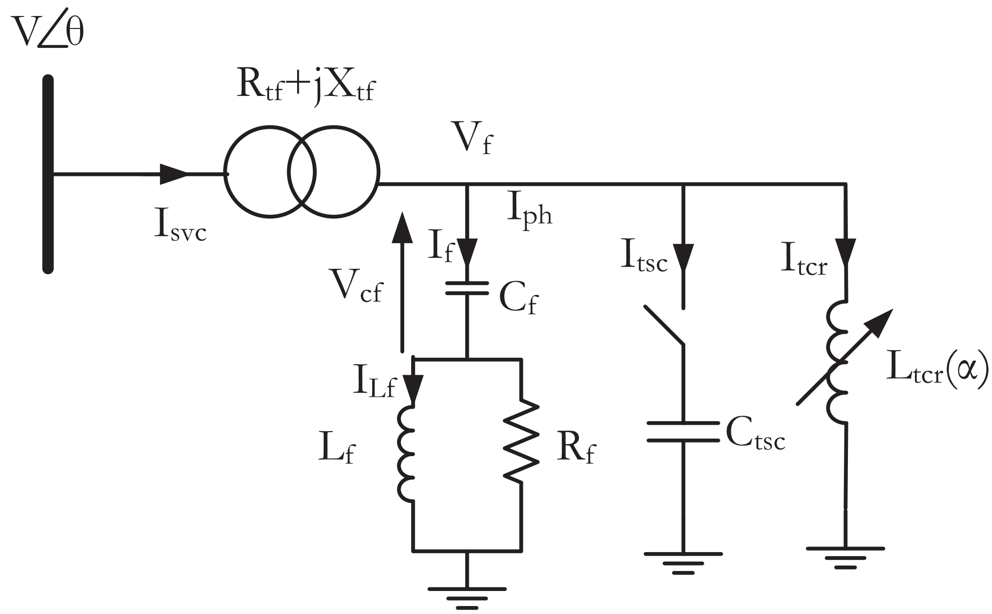

Figure B.1: SVC electrical circuit model

When developing the SVC small signal model, the electrical system model which includes the transformer, filter, capacitor and controlled reactor model and the controller model is developed separately and later combined together to obtain the final model. The modelled presented in this chapter assumed currents flowing into the SVC as positive.

B.1 SVC Transformer Model

Dynamic phasors are used to represent the SVC transformer. Let R_{tf} and X_{tf} be the resistance and the leakage reactance of the transformer, respectively. If I_{svc} is the current flowing into the SVC through the transformer, $V\angle\theta$ is the point of common coupling voltage and V_f is the SVC filter bus voltage, the dynamic phasor model of the transformer can be written in per unit as,

$$\dot{I}_{svc} = -\frac{\omega_0 R_{tf}}{X_{tf}} I_{svc} - j\omega_0 I_{tf} + \frac{\omega_0}{X_{tf}} V - \frac{\omega_0}{X_{tf}} V_f \tag{B.1}$$

The small signal model of the transformer is obtained by linearizing Equation (B.1) and decomposing voltage and current terms into real (R) and imaginary (I) axis as,

$$\Delta\dot{\mathbf{X}}_{tf} = \mathbf{A}_{tf}\Delta\mathbf{X}_{tf} + \mathbf{E}_{tf}\Delta\mathbf{V} + \mathbf{F}_{tf}\Delta\mathbf{Z}_{tf} \tag{B.2}$$

where,

$\Delta\mathbf{X}_{tf} = [\Delta I_{svcR}, \Delta I_{svcI}]^T$, $\Delta\mathbf{V} = [\Delta V_R, \Delta V_I]^T$, $\Delta\mathbf{Z}_{tf} = [\Delta V_{fR}, \Delta V_{fI}]^T$

$$\mathbf{A}_{tf} = \begin{bmatrix} -\frac{\omega_0 R_{tf}}{X_{tf}} & \omega_0 \\ -\omega_0 & -\frac{\omega_0 R_{tf}}{X_{tf}} \end{bmatrix}, \quad \mathbf{E}_{tf} = \begin{bmatrix} \frac{\omega_0}{X_{tf}} & 0 \\ 0 & \frac{\omega_0}{X_{tf}} \end{bmatrix}, \quad \mathbf{F}_{tf} = -\begin{bmatrix} \frac{\omega_0}{X_{tf}} & 0 \\ 0 & \frac{\omega_0}{X_{tf}} \end{bmatrix}$$

B.2 Filter Model

A high pass filter is used to filter out the high frequency harmonics generated by the continuous switching of the reactor. In this model a series RLC filter is used. Let R_f be the filter resistance, L_f be the filter inductance, C_f be the filter capacitance, I_f be the filter current, I_{Lf} be the current flowing through the filter inductor, and V_{cf} be the voltage across the filter capacitor. The per unit dynamic phasor model of the filter capacitor is given by

$$\dot{V}_{cf} = -j\omega_0 V_{cf} + \frac{\omega_0}{C_f} I_f \tag{B.3}$$

The per unit dynamic phasor model of the inductor is given by,

$$\dot{I}_{Lf} = -j\omega_0 I_{Lf} + \frac{\omega_0}{L_f}V_f - \frac{\omega_0}{L_f}V_{cf} \tag{B.4}$$

Using the voltage drop across the filter resistor, the filter current can be expressed in terms of the filter bus voltage, voltage across the filter capacitor and the current flowing through the filter inductor as,

$$I_f = \frac{1}{R_f}V_f - \frac{1}{R_f}V_{cf} + I_{Lf} \tag{B.5}$$

The small signal model of the filter is obtained by expressing Equations (B.3)-(B.5) in $R - I$ reference frame, linearizing and eliminating I_f. The linearized model of the filter is given by,

$$\Delta\dot{\mathbf{X}}_f = \mathbf{A}_f\Delta\mathbf{X}_f + \mathbf{F}_f\Delta\mathbf{Z} \tag{B.6}$$

where,

$$\Delta\mathbf{X}_f = [\Delta V_{cfR}, \Delta V_{cfI}, \Delta I_{LfR}, \Delta I_{LfI}]^T, \qquad \Delta\mathbf{Z} = [\Delta V_{fR}, \Delta V_{fI}]^T$$

$$\mathbf{A}_f = \begin{bmatrix} -\dfrac{\omega_0}{R_fC_f} & \omega_0 & \dfrac{\omega_0}{C_f} & 0 \\ -\omega_0 & -\dfrac{\omega_0}{R_fC_f} & 0 & \dfrac{\omega_0}{C_f} \\ -\dfrac{\omega_0}{L_f} & 0 & 0 & \omega_0 \\ 0 & -\dfrac{\omega_0}{L_f} & -\omega_0 & 0 \end{bmatrix}, \qquad \mathbf{F}_f = \begin{bmatrix} \dfrac{\omega_0}{R_fC_f} & 0 \\ 0 & \dfrac{\omega_0}{R_fC_f} \\ \dfrac{\omega_0}{L_f} & 0 \\ 0 & \dfrac{\omega_0}{L_f} \end{bmatrix}$$

B.3 Thyristor Controlled Reactor Model

The thyristor controlled reactor is the main controlled element in the SVC. The effective inductance of the SVC is varied by varying the firing angle of the thyristor. Therefore, the relationship between the instantaneous voltage across the controllable reactor (v_f) and the current flowing through it (i_{tcr}) is given by,

$$v_f = L_{tcr}(\alpha) i_{tcr} \tag{B.7}$$

where, L_{tcr} is the inductance of the controllable reactor and α is the firing angle.

Per unitizing Equation (B.7) and expressing it in phasor domain results in,

$$\dot{I}_{tcr} = -j\omega_0 I_{tcr} + \frac{\omega_0}{L_{tcr}(\alpha)} V_f \tag{B.8}$$

Linearizing Equation (B.8) yields,

$$\Delta\dot{I}_{tcr} = -j\omega_0 \Delta I_{tcr} + \frac{\omega_0}{L_{tcr}(\alpha)} \Delta V_f + \omega_0 V_s \Delta \left(\frac{1}{L_{tcr}(\alpha)} \right) \tag{B.9}$$

Considering only the fundamental component of the current, the effective reactive admittance of the SVC is given by, [58],

$$B_{tcr}(\alpha) = \frac{1}{\omega L} \left(1 - \frac{2\alpha}{\pi} - \frac{1}{\pi} \sin 2\alpha \right) \tag{B.10}$$

Note that $-\pi/2 \leq \alpha \leq \pi/2$, $B_{tcr} < 0$ and $L_{tcr} = L_{tcr}(0)$. Realizing that $B_{tcr}(\alpha) = 1/[\omega L(\alpha)]$ and linearizing Equation (B.10),

$$\Delta \left(\frac{1}{L_{tcr}(\alpha)} \right) = \frac{-2}{L\pi} \left(1 + \cos 2\alpha \right) \Delta\alpha = K_{svc} \Delta\alpha \tag{B.11}$$

where, $K_{svc} = \dfrac{-2}{L\pi} (1 + \cos 2\alpha)$.

Substituting $\Delta \left(\frac{1}{L_{tcr}(\alpha)} \right)$ in Equation (B.9) with (B.11), the current flowing through the TCR can be found as,

$$\Delta \dot{I}_{tcr} = -j\omega_0 \Delta I_{tcr} + \frac{\omega_0}{L_{tcr}(\alpha)} \Delta V_s + \omega_0 V_f K_{svc} \Delta\alpha \tag{B.12}$$

Expressing Equation (B.12) in R-I reference frame, the small signal model of the thyristor controlled reactor can be found as,

$$\Delta \dot{\mathbf{X}}_{tcr} = \mathbf{A}_{tcr} \Delta \mathbf{X}_{tcr} + \mathbf{B}_{tcr} \Delta U_{tcr} + \mathbf{F}_{tcr} \Delta \mathbf{Z} \tag{B.13}$$

where,

$$\Delta \mathbf{X}_f = [\Delta I_{tcrR}, \Delta I_{tcrI}]^T, \quad \Delta U_{tcr} = \Delta\alpha, \qquad \Delta \mathbf{Z} = [\Delta V_{fR}, \Delta V_{fI}]^T$$

$$\mathbf{A}_{tcr} = \begin{bmatrix} 0 & \omega_0 \\ -\omega_0 & 0 \end{bmatrix}, \qquad \mathbf{B}_{tcr} = \begin{bmatrix} K_{svc}\omega_0 V_{fR} \\ K_{svc}\omega_0 V_{fI} \end{bmatrix}, \quad \mathbf{F}_{tcr} = \begin{bmatrix} \frac{\omega_0}{L(\alpha)} & 0 \\ 0 & \frac{\omega_0}{L(\alpha)} \end{bmatrix}$$

B.4 Thyristor Switched Capacitor Model

The thyristor switched capacitor is used by the SVC to provide the capacitive reactive power into the system. When the system requires the capacitive reactive power, the TSC is switched on. The amount of capacitive reactive power is controlled by controlling inductive reactive power absorbed by the TCR.

If C_{tsc} is the TCR capacitance and I_{tsc} is the current flowing into the TSC, the per unit dynamic phasor model of the TSC is given by,

$$\dot{V}_f = -j\omega_0 V_f + \frac{\omega_0}{C_{tsc}} I_{tsc} \tag{B.14}$$

Also note that from the Kirchoff's current law,

$$I_{svc} = I_f + I_{tsc} + I_{tcr} \tag{B.15}$$

Substituting for I_{tsc} in B.14 from Equations B.5 and B.14 and linearizing results in the small signal model of the TSC shown in Equation (B.16).

$$\Delta\dot{\mathbf{X}}_{tsc} = \mathbf{A}_{tsc}\Delta\mathbf{X}_{tsc} + \mathbf{F}_{tsc}\Delta\mathbf{Z}_{tsc} \tag{B.16}$$

where,

$\Delta\mathbf{X}_{tsc} = [\Delta V_{fR}, \Delta V_{fI}]^T$,

$\Delta\mathbf{Z}_{tsc} = [\Delta I_{svcR}, \Delta I_{svcI}, \Delta V_{cfR}, \Delta V_{cfI}, \Delta I_{LfR}, \Delta I_{LfI}, \Delta I_{tcrR}, \Delta I_{tcrI}]^T$

$$\mathbf{A}_{tsc} = \begin{bmatrix} -\dfrac{\omega_0}{R_f C_{tsc}} & \omega_0 \\ -\omega_0 & -\dfrac{\omega_0}{R_f C_{tsc}} \end{bmatrix},$$

$$\mathbf{F}_{tsc} = \begin{bmatrix} \dfrac{\omega_0}{C_{tsc}} & 0 & \dfrac{\omega_0}{R_f C_{tsc}} & 0 & -\dfrac{\omega_0}{C_{tsc}} & 0 & -\dfrac{\omega_0}{C_{tsc}} & 0 \\ 0 & \dfrac{\omega_0}{C_{tsc}} & 0 & \dfrac{\omega_0}{R_f C_{tsc}} & 0 & -\dfrac{\omega_0}{C_{tsc}} & 0 & -\dfrac{\omega_0}{C_{tsc}} \end{bmatrix}$$

Note that the TSC is in service only when the SVC is supplying reactive power into the system. Therefore, when the SVC is absorbing the reactive power the TSC model is not included in the SVC model.

The complete electrical model of the SVC is obtained by combining the transformer mode, filter model, TSC model, and the TCR model as shown below.

$$\Delta\dot{\mathbf{X}}_{SVCe} = \mathbf{A}_{SVCe}\Delta\mathbf{X}_{SVCe} + \mathbf{B}_{SVCe}\Delta U_{SVCe} + \mathbf{E}_{SVCe}\Delta\mathbf{V} \tag{B.17}$$

where,

$$\Delta \mathbf{X}_{SVCe} = [\Delta \mathbf{X}_{tf}, \Delta \mathbf{X}_{f}, \Delta \mathbf{X}_{tcr}, \Delta \mathbf{X}_{tsc}]^T, \qquad \Delta U_{SVCe} = \Delta\alpha$$

B.5 SVC Controller Model

The controller block diagram of the SVC is shown in Figure B.2. The firing angle of the TCR is obtained by comparing the filtered terminal voltage magnitude with the voltage reference. Note that the SVC controller is operated with a droop R. A Low pass filter and two band reject filters are included in the controller to filter out the high frequency oscillations produced by the thyristor switching and also to avoid the parallel resonances present in the system getting destabilized by the voltage regulator [59]. The small signal model presented below includes the measuring filter, low pass filter, two band reject filters and PI controller models.

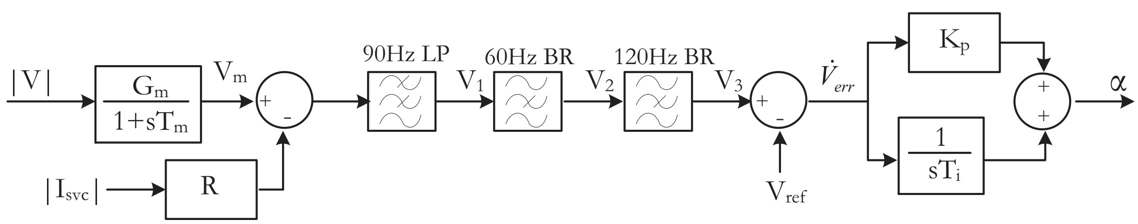

Figure B.2: SVC Controller

B.5.1 Measuring Filter Model

If G_m is the measuring filter gain, T_m is the measuring filter time constant and V_m is the measured voltage, the linearized model of the measuring filter can be easily obtained as,

$$\Delta \dot{V}_m = \frac{1}{T_m}(G_m \Delta V - \Delta V_m) \tag{B.18}$$

Recognizing $\Delta V = \dfrac{V_R}{|V|}\Delta V_R + \dfrac{V_I}{|V|}\Delta V_I$, the small signal model of the measuring filter can be written as,

$$\Delta \dot{X}_m = -\frac{1}{T_m}\Delta X_m + \mathbf{E}_m \Delta V \tag{B.19}$$

where,

$$\Delta X_m = \Delta V_m, \qquad \Delta \mathbf{V} = [\Delta V_R, \Delta V_I]^T$$

$$\mathbf{E}_m = \left[\begin{array}{cc} \frac{G_m V_R}{T_m |V|} & \frac{G_m V_I}{T_m |V|} \end{array} \right]$$

B.5.2 Low Pass Filter Model

In this model, a second order low pass filter is used. If G_{LP} is the filter gain, ω_{cLP} is the filter cut-off frequency, ζ_{LP} is the damping coefficient, V_0 is the filter input, and V_1 is the filter output, the transfer function of the low pass filter is given by,

$$\frac{V_1}{V_0} = \frac{G_{LP}\omega_{cLP}^2}{s^2 + 2\zeta_{LP}\omega_{cLP}s + \omega_{cLP}^2} \tag{B.20}$$

Equation (B.20) can be re-written in the form,

$$V_1(s^2 + 2\zeta_{LP}\omega_{cLP}s + \omega_{cLP}^2) = G_{LP}\omega_{cLP}^2 V_0 \tag{B.21}$$

Let

$$V_1{}' = sV_1. \tag{B.22}$$

Then Equation (B.21) can be written as,

$$\dot{V_1}{}' = G_{LP}\omega_{cLP}^2 V_0 - 2\zeta_{LP}\omega_{cLP}V_1{}' - \omega_{cLP}^2 V_1 \tag{B.23}$$

Using the control block diagram shown in Figure B.2 the low pass filter input can be written as

$$V_0 = V_m - R|I_{svc}| \tag{B.24}$$

Therefore, the small signal model of the low pass filter is obtained by linearizing Equations (B.22)-(B.24) as,

$$\Delta\dot{\mathbf{X}}_{LP} = \mathbf{A}_{LP}\Delta\mathbf{X}_{LP} + \mathbf{F}_{LP}\Delta\mathbf{Z}_{LP} \tag{B.25}$$

where,

$$\Delta\mathbf{X}_{LP} = [\Delta V_1, \Delta V_1{}']^T ,$$

$$\Delta\mathbf{Z} = [\Delta V_m, \Delta I_{svcR}, \Delta I_{svcI}]^T ,$$

$$\mathbf{A}_{LP} = \begin{bmatrix} 0 & 1 \\ -\omega_{cLP}^2 & -2\zeta_{LP}\omega_{cLP} \end{bmatrix},$$

$$\mathbf{F}_{LP} = \begin{bmatrix} 0 & 0 & 0 \\ G_{LP}\omega_{cLP}^2 & -\dfrac{G_{LP}R\omega_{cLP}^2 I_{svcR}}{I_{svc}} & -\dfrac{G_{LP}R\omega_{cLP}^2 I_{svcI}}{I_{svc}} \end{bmatrix}$$

B.5.3 Band Reject Filter Model

In this model a second order band reject filter is used. If G_{B1} is the filter gain, ω_{cB1} is the filter cut-off frequency, ζ_{B1} is the damping coefficient, and V_2 is the filter output, the transfer function of the filter is given by,

$$\frac{V_2}{V_1} = \frac{G_{B1}\omega_{cB1}s + G_{B1}\omega_{cB1}^2}{s^2 + 2\zeta_{B1}\omega_{cB1}s + \omega_{cB1}^2} \tag{B.26}$$

If $V_2{}' = sV_2$, the band reject filter small signal model can be obtain by following a procedure similar to the one followed to obtain the low pass filter model. The band reject filter small signal model is given by,

$$\Delta\dot{\mathbf{X}}_{B1} = \mathbf{A}_{B1}\Delta\mathbf{X}_{B1} + \mathbf{F}_{B1}\Delta\mathbf{Z}_{B1} \tag{B.27}$$

where,

$$\Delta\mathbf{X}_{B1} = [\Delta V_2, \Delta V_2{}']^T, \qquad \Delta\mathbf{Z} = [\Delta V_1, \Delta V_1{}']^T,$$

$$\mathbf{A}_{B1} = \begin{bmatrix} 0 & 1 \\ -\omega_{cB1}^2 & -2\zeta_{B1}\omega_{cB1} \end{bmatrix}, \qquad \mathbf{F}_{B1} = \begin{bmatrix} 0 & 0 \\ G_{B1}\omega_{cB1}^2 & G_{B1}\omega_{cB1} \end{bmatrix}$$

Similarly, the second band reject filter model is given by,

$$\Delta\dot{\mathbf{X}}_{B2} = \mathbf{A}_{B2}\Delta\mathbf{X}_{B2} + \mathbf{F}_{B2}\Delta\mathbf{Z}_{B2} \tag{B.28}$$

where,

$$\Delta\mathbf{X}_{B2} = [\Delta V_3, \Delta V_3{}']^T, \qquad \Delta\mathbf{Z} = [\Delta V_2, \Delta V_2{}']^T,$$

$$\mathbf{A}_{B2} = \begin{bmatrix} 0 & 1 \\ -\omega_{cB2}^2 & -2\zeta_{B2}\omega_{cB2} \end{bmatrix}, \qquad \mathbf{F}_{B2} = \begin{bmatrix} 0 & 0 \\ G_{B2}\omega_{cB2}^2 & G_{B2}\omega_{cB1} \end{bmatrix}$$

B.5.4 PI Controller Model

Let K_p and T_i be the proportional gain and the integrator time constant of the PI controller, respectively. Then the small signal model of the PI controller can be easily obtained as,

$$\Delta\dot{V}_{err} = \Delta V_3 - \Delta V_{ref} \tag{B.29}$$

$$\Delta\alpha = \frac{1}{T_i}\Delta V_{err} - K_p\Delta V_{ref} + K_p\Delta V_3 \tag{B.30}$$

The complete small signal model of the SVC controller is obtained by combining the models for the measuring filter, low pass filter, two band reject filters and the PI controller. The controller small signal model is given in Equation (B.32).

$$\begin{aligned}
\Delta\dot{\mathbf{X}}_{SVCc} &= \mathbf{A}_{SVCc}\Delta\mathbf{X}_{SVCc} + \mathbf{B}_{SVCc}\Delta U_{SVCc} + \mathbf{E}_{SVCc}\Delta\mathbf{V} \qquad \text{(B.31)} \\
&\quad + \mathbf{F}_{SVCc}\Delta\mathbf{Z}_{SVCc} \\
\Delta Y_{SVCc} &= \mathbf{C}_{SVCc}\Delta\mathbf{X}_{SVCc} + D_{SVCc}\Delta U_{SVCc} \qquad \text{(B.32)} \\
& \qquad \text{(B.33)}
\end{aligned}$$

where,

$$\Delta\mathbf{X}_{SVCc} = [\Delta V_m, \Delta V_1, \Delta {V_1}', \Delta V_2, \Delta {V_2}', \Delta V_3, \Delta {V_3}', \Delta V_{err}]^T,$$

$$\Delta U_{SVCc} = V_{ref}$$

$$\Delta\mathbf{Z}_{SVCc} = [\Delta I_{svcR}, \Delta I_{svcI}]^T$$

$$\Delta Y_{SVCc} = \alpha$$

Finally, the complete SVC small signal model is obtained by combining the electrical model and the controller model as,

$$\Delta\dot{\mathbf{X}}_{SVC} = \mathbf{A}_{SVC}\Delta\mathbf{X}_{SVC} + \mathbf{B}_{SVC}\Delta U_{SVC} + \mathbf{E}_{SVC}\Delta\mathbf{V} \qquad \text{(B.34)}$$

$$\text{(B.35)}$$

where,

$$\Delta\mathbf{X}_{SVC} = [\Delta\mathbf{X}_{SVCe}, \Delta\mathbf{X}_{SVCc}]^T, \qquad \Delta U_{SVC} = \Delta V_{ref}.$$

Appendix C

Small Signal Model of a STATCOM

The Static Synchronous Compensator (STATCOM) is voltage source converter based reactive power control device. It can be viewed as a controlled voltage source placed behind a reactance. When the voltage behind the reactance is greater than the network voltage, the STATCOM supplies reactive power to the network; whereas when the voltage behind the reactance is less than the network voltage, the STATCOM absorbs reactive power from the network. The steady state characteristics of a STATCOM is shown in Figure C.1. Under normal operation the STATCOM linearly varies its reactive current as the network voltage changes. However, the STATCOM can supply its maximum inductive or capacitive current regardless of the network voltage when it is operating at the limit. This constant current characteristic outside the control range gives a STATCOM superior voltage support capabilities over an SVC. Due to the usage of voltage source converter technology, a STATCOM has faster dynamic response compared to an SVC. Other advantages of a STATCOM includes less or no filtering requirements, less station footprint requirement due to the replacement of passive elements with compact active elements and ability to control active power if the dc capacitor banks are replaced with an energy storage device. However, the main disadvantage of a STATCOM is its high cost compared to an SVC.

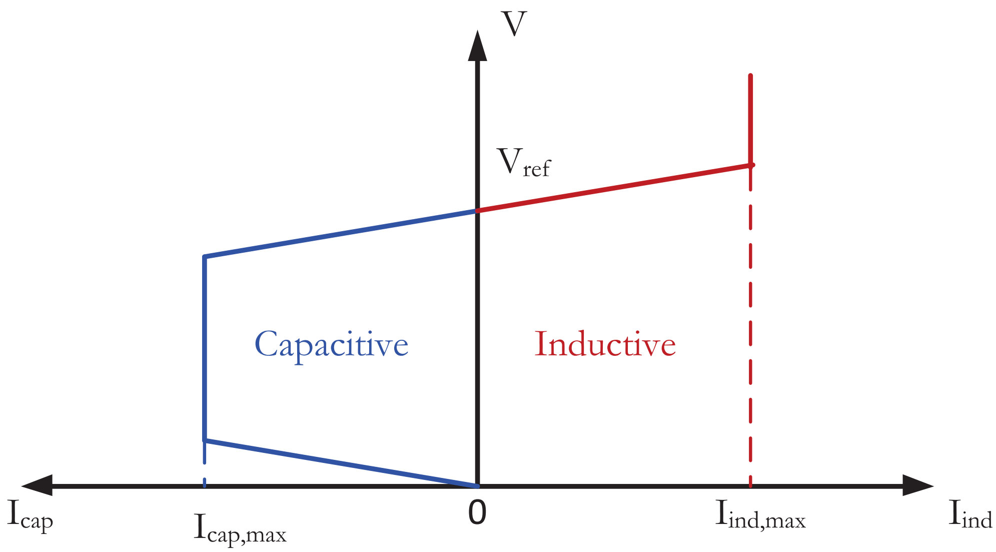

Figure C.1: Steady state characteristics of a STATCOM

A schematic diagram of the small signal model of a STATCOM is shown in Figure C.2. It is assumed that the voltage source converter uses the two level pulse width modulated switching. Since the typical switching frequency of a PWM converter is in kHz range, the converter switching is neglected in the small signal model. The STATCOM transformer, phase reactor, the high pass filter and the dc capacitor are included in the model. The current flowing into the STATCOM is assumed to be positive in this model. Also, the STATCOM is assumed to have no active power control capability.

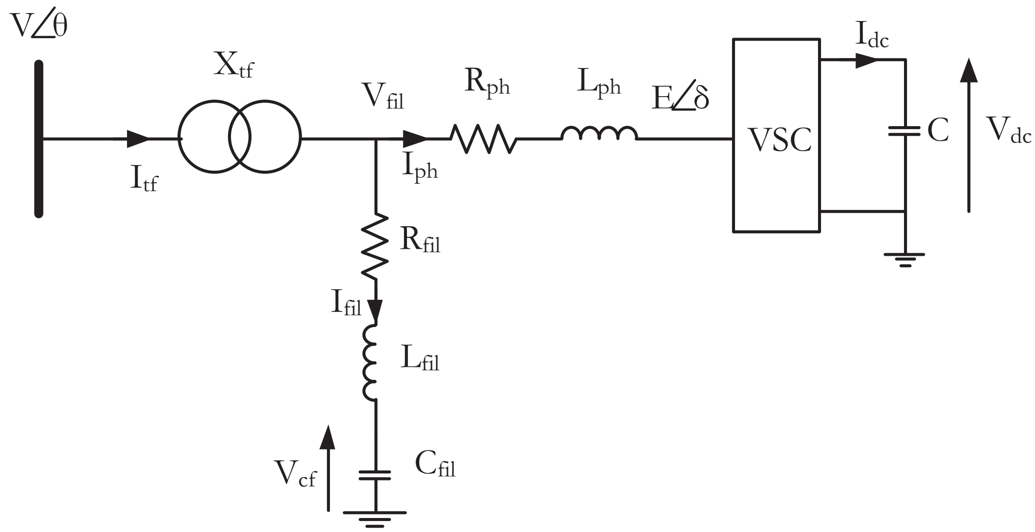

Figure C.2: STATCOM small signal model

C.1 STATCOM Transformer Model

Dynamic phasors are used to represent the STATCOM transformer. Let R_{tf} and X_{tf} be the resistance and the leakage reactance of the transformer, respectively. If I_{tf} is the current flowing into the STATCOM through the transformer, $V_{pcc}\angle\theta$ is the point of common coupling voltage and V_f is the STATCOM filter bus voltage, the dynamic phasor model of the transformer can be written in per unit as,

$$\dot{I}_{tf} = -\frac{\omega_0 R_{tf}}{X_{tf}} I_{tf} - j\omega_0 I_{tf} + \frac{\omega_0}{X_{tf}} V_{pcc} - \frac{\omega_0}{X_{tf}} V_f \tag{C.1}$$

The small signal model of the transformer is obtained by linearizing Equation (C.1) and decomposing voltage and current terms into real (R) and imaginary (I) axis as,

$$\Delta\dot{\mathbf{X}}_{tf} = \mathbf{A}_{tf}\Delta\mathbf{X}_{tf} + \mathbf{E}_{tf}\Delta\mathbf{V} + \mathbf{F}_{tf}\Delta\mathbf{Z}_{tf} \tag{C.2}$$

where,

$$\Delta\mathbf{X}_{tf} = [\Delta I_{tfR}, \Delta I_{tfI}]^T, \qquad \Delta\mathbf{V} = [\Delta V_{pccR}, \Delta V_{pccI}]^T, \quad \Delta\mathbf{Z}_{tf} = [\Delta V_{fR}, \Delta V_{fI}]^T$$

$$\mathbf{A}_{tf} = \begin{bmatrix} -\frac{\omega_0 R_{tf}}{X_{tf}} & \omega_0 \\ -\omega_0 & -\frac{\omega_0 R_{tf}}{X_{tf}} \end{bmatrix}, \quad \mathbf{E}_{tf} = \begin{bmatrix} \frac{\omega_0}{X_{tf}} & 0 \\ 0 & \frac{\omega_0}{X_{tf}} \end{bmatrix}, \quad \mathbf{F}_{tf} = -\begin{bmatrix} \frac{\omega_0}{X_{tf}} & 0 \\ 0 & \frac{\omega_0}{X_{tf}} \end{bmatrix}$$

C.2 Phase Reactor Model

If R_{ph} is the phase reactor resistance, L_{ph} is the phase reactor inductance, and $E\angle\delta$ is the voltage at the converter terminal, the linearized dynamic phasor model for the phase reactor in per unit can be obtained similar to the transformer model.

$$\Delta\dot{\mathbf{X}}_{ph} = \mathbf{A}_{ph}\Delta\mathbf{X}_{ph} + \mathbf{B}'_{ph}\Delta\mathbf{U}'_{ph} + \mathbf{F}_{ph}\Delta\mathbf{Z} \tag{C.3}$$

where,

$$\Delta\mathbf{X}_{ph} = [\Delta I_{phR}, \Delta I_{phI}]^T, \qquad \Delta\mathbf{U}'_{ph} = [\Delta E_R, \Delta E_I]^T, \qquad \Delta\mathbf{Z} = [\Delta V_{fR}, \Delta V_{fI}]^T$$

$$\mathbf{A}_{ph} = \begin{bmatrix} -\frac{\omega_0 R_{ph}}{L_{ph}} & \omega_0 \\ -\omega_0 & -\frac{\omega_0 R_{ph}}{L_{ph}} \end{bmatrix}, \quad \mathbf{B}'_{ph} = \begin{bmatrix} -\frac{\omega_0}{L_{ph}} & 0 \\ 0 & -\frac{\omega_0}{L_{ph}} \end{bmatrix}, \quad \mathbf{F}_{ph} = \begin{bmatrix} \frac{\omega_0}{L_{ph}} & 0 \\ 0 & \frac{\omega_0}{L_{ph}} \end{bmatrix}$$

If m is the modulation index of the converter, V_{dc} is the dc voltage, V_{base} is the STATCOM base voltage, the converter terminal voltage magnitude E can be expressed as,

$$E = \frac{\sqrt{3} m V_{dc}}{\sqrt{8} V_{base}} \tag{C.4}$$

Then the real and imaginary axis components of the converter terminal voltage is given by,

$$E_R = E\cos(\theta + \delta), \qquad E_I = E\sin(\theta + \delta) \tag{C.5}$$

The term $\Delta\mathbf{U}'_{ph}$ in Equation (C.3) can be found by substituting Equation (C.4) in Equation (C.5) and linearizing.

$$\Delta\mathbf{U}'_{ph} = \mathbf{B}''_{ph}\Delta\mathbf{U}_{ph} \tag{C.6}$$

where,

$$\Delta\mathbf{U}_{ph} = [\Delta m, \Delta\delta, \Delta V_{dc}, \Delta\theta]^T, \qquad \mathbf{B}''_{ph} = \begin{bmatrix} b^{11}_{ph} & b^{12}_{ph} & b^{13}_{ph} & b^{14}_{ph} \\ b^{21}_{ph} & b^{22}_{ph} & b^{23}_{ph} & b^{24}_{ph} \end{bmatrix}$$

$$K_{ph} = \frac{\sqrt{3}\omega_0}{\sqrt{8}V_{base}L_{ph}}, \qquad b^{11}_{ph} = -K_{ph}V_{dc0}\cos(\theta + 0 + \delta_0),$$

$$b^{12}_{ph} = K_{ph}m_0V_{dc0}\sin(\theta_0 + \delta_0), \qquad b^{13}_{ph} = -K_{ph}m_0\cos(\theta_0 + \delta_0),$$

$$b^{14}_{ph} = K_{ph}m_0V_{dc0}\sin(\theta_0 + \delta_0), \qquad b^{21}_{ph} = -K_{ph}V_{dc0}\sin(\theta_0 + \delta_0),$$

$$b^{22}_{ph} = -K_{ph}m_0V_{dc0}\cos(\theta_0 + \delta_0), \qquad b^{23}_{ph} = -K_{ph}m_0\sin(\theta_0 + \delta_0),$$

$$b^{24}_{ph} = -K_{ph}m_0V_{dc0}\cos(\theta_0 + \delta_0)$$

Note that subscript 0 denotes a steady state quantity. The linearized model of the phase reactor can be obtained in the form,

$$\Delta\dot{\mathbf{X}}_{ph} = \mathbf{A}_{ph}\Delta\mathbf{X}_{ph} + \mathbf{B}\Delta\mathbf{U}_{ph} + \mathbf{F}_{ph}\Delta\mathbf{Z}_{ph} \tag{C.7}$$

where, $\mathbf{B}_{ph} = \mathbf{B}'_{ph}\mathbf{B}''_{ph}$.

C.3 Filter Model

A high pass filter is used to filter out the high frequency harmonics generated by the PWM converter. In this model a series RLC filter is used. Let R_{fil} be the filter resistance, L_{fil} be the filter inductance, C_{fil} be the filter capacitance, I_{fil} be the filter current and V_{cf} be the voltage across the filter capacitor. The RL portion of the filter is modelled similar to the transformer and the phase reactor. The per unit dynamic phasor model of the filter capacitor is given by

$$\dot{V}_{cf} = -j\omega_0 V_{cf} + \frac{\omega_0}{C_{fil}} I_{fil} \tag{C.8}$$

The small signal model of the filter is obtained by expressing Equation (C.7) in $R-I$ reference frame, linearizing and combined with the filter RL model. The filter linearized model is expressed in the form,

$$\Delta\dot{\mathbf{X}}_{fil} = \mathbf{A}_{fil}\Delta\mathbf{X}_{fil} + \mathbf{F}_{fil}\Delta\mathbf{Z} \tag{C.9}$$

where,

$$\Delta\mathbf{X}_{fil} = [\Delta I_{filR}, \Delta I_{filI}, \Delta V_{cfR}, \Delta V_{cfI}]^T, \qquad \Delta\mathbf{Z} = [\Delta V_{fR}, \Delta V_{fI}]^T$$

$$\mathbf{A}_{fil} = \begin{bmatrix} -\frac{\omega_0 R_{fil}}{L_{fil}} & \omega_0 & -\frac{\omega_0}{L_{fil}} & 0 \\ -\omega_0 & -\frac{\omega_0 R_{fil}}{L_{fil}} & 0 & -\frac{\omega_0}{L_{fil}} \\ \frac{\omega_0}{C_{fil}} & 0 & 0 & \omega_0 \\ 0 & \frac{\omega_0}{C_{fil}} & -\omega_0 & 0 \end{bmatrix}, \qquad \mathbf{F}_{fil} = \begin{bmatrix} \frac{\omega_0}{L_{fil}} & 0 \\ 0 & \frac{\omega_0}{L_{fil}} \\ 0 & 0 \\ 0 & 0 \end{bmatrix}$$

C.4 Converter Model

As mentioned earlier in this chapter, the high frequency PWM switching is neglected in the small signal model. Since the frequency range of interest is well below the switching frequency of the converter, this assumption does not cause significant impact to the results obtained with the small signal model. In developing the converter model, a loss less converter is assumed.

Equation (C.10) can be written considering the active power balance in the converter.

$$V_{dc}I_{dc} = (E_R I_{phR} + E_I I_{phI})M_{base} \tag{C.10}$$

where, M_{base} is the STATCOM MVA base. Note that the dc voltage and the current in Equation (C.10) are expressed in actual units where as the ac quantities are expressed in per unit. Using the above equation together with Equations (C.4) and (C.5), an expression for the dc current can be obtained in the following form.

$$I_{dc} = \frac{\sqrt{3}mM_{base}}{\sqrt{8}V_{base}}\left[I_{phR}\cos(\theta+\delta) + I_{phI}\sin(\theta+\delta)\right] \tag{C.11}$$

The converter dynamics are governed by the converter controllers and the dynamics of the dc capacitor. The converter controller model will be presented later in this chapter. The dc capacitor model can be simply written using Equation (C.8) with $\omega_0 = 0$ as,

$$\dot{V}_{dc} = \frac{1}{C}I_{dc} \tag{C.12}$$

where C is the dc capacitor capacitance.

The small signal model of the dc capacitor can be obtained by substituting for I_{dc} from Equation (C.11) and linearizing Equation (C.12) as,

$$\Delta\dot{V}_{dc} = \mathbf{B}_{dc}\Delta\mathbf{U}_{dc} \tag{C.13}$$

where,

$$\Delta\mathbf{U}_{dc} = [\Delta I_{phR}, \Delta I_{phI}, \Delta\theta, \Delta\delta, \Delta m]^T, \qquad \mathbf{B}_{dc} = \begin{bmatrix} b_{dc}^{11} & b_{dc}^{12} & b_{dc}^{13} & b_{dc}^{14} & b_{dc}^{15} \end{bmatrix},$$

$$K_{dc} = \frac{\sqrt{3}S_{base}}{\sqrt{8}V_{base}C} \qquad b_{dc}^{11} = K_{dc}m_0\cos(\theta_0+\delta_0), \qquad b_{dc}^{12} = K_{dc}m_0\sin(\theta_0+\delta_0),$$

$$b_{dc}^{13} = K_{dc}m_0(-I_{phR0}\sin(\theta_0+\delta_0) + I_{phI0}\cos(\theta_0+\delta_0)),$$

$$b_{dc}^{14} = K_{dc}m_0(-I_{phR0}\sin(\theta_0+\delta_0) + I_{phI0}\cos(\theta_0+\delta_0)),$$

$$b_{dc}^{15} = K_{dc}(I_{phR0}\cos(\theta_0+\delta_0) + I_{phI0}\sin(\theta_0+\delta_0)).$$

C.5 Phase Locked Loop Model

The phase locked loop (PLL) generates a ramp signal that is synchronized to a reference signal. Therefore, a PLL is used in the STATCOM to synchronize the voltage generated by the converter to the point of common coupling voltage. The control block diagram of a typical PLL [48] is shown in Figure C.3. The dynamic model of the PLL can be easily derived by looking at the control block diagram as follows.

$$\dot{X}_{PLL} = \sin(\theta_{ref} - \theta) \tag{C.14}$$

$$\dot{\theta} = K_{pp}\dot{X}_{PLL} + K_{ip}X_{PLL} + \omega_0 \tag{C.15}$$

$$\tan\theta = \frac{V_{pccI}}{V_{pccR}} \tag{C.16}$$

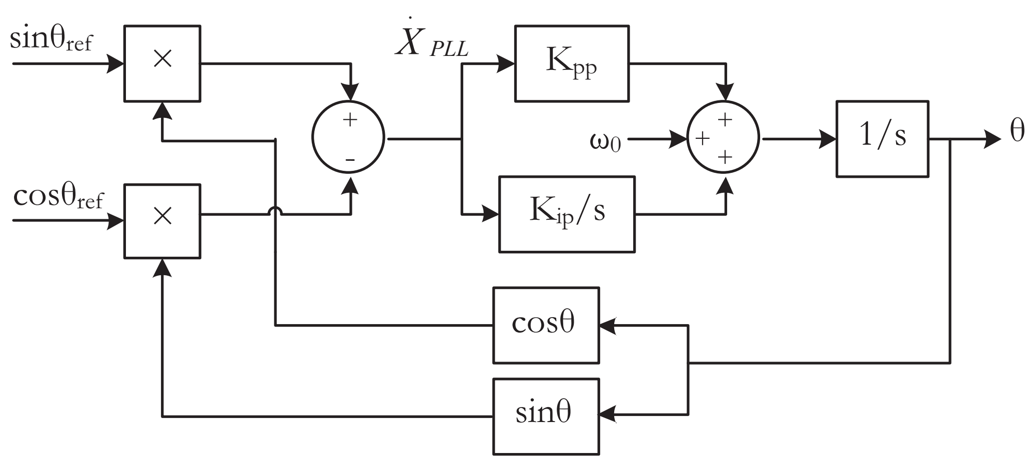

Figure C.3: PLL control block diagram

The small signal model of the PLL is obtained in the form shown in Equation (C.17) by linearizing Equations (C.14 - C.16) and eliminating $\Delta\theta_{ref}$.

$$\Delta\dot{\mathbf{X}}_{pl} = \mathbf{A}_{pl}\Delta\mathbf{X}_{pl} + \mathbf{E}_{pl}\Delta\mathbf{V} \tag{C.17}$$

where,

$$\Delta\mathbf{X}_{pl} = [\Delta X_{PLL}, \Delta\theta]^T, \qquad \Delta\mathbf{V} = [\Delta V_{pccR}, \Delta V_{pccI}]^T$$

$$\mathbf{A}_{pl} = \begin{bmatrix} 0 & -1 \\ K_{ip} & -K_{pp} \end{bmatrix}, \qquad \mathbf{E}_{pl} = \begin{bmatrix} \dfrac{-V_{pccI0}}{(V_{pccR0}\sec\theta_0)^2} & \dfrac{1}{V_{pccR0}\sec^2\theta_0} \\ \dfrac{-V_{pccI0}K_{pp}}{(V_{pccR0}\sec\theta_0)^2} & \dfrac{K_{pp}}{V_{pccR0}\sec^2\theta_0} \end{bmatrix}$$

The complete electrical system model of the STATCOM is obtained by combining the transformer model, the phase reactor model, the filter model, the converter model and the phase locked loop model. Note that inputs for some models are states in some other models. For example, $\Delta\theta$ is considered as an input in the phase reactor model and in the converter model. However it is a state in the PLL model. Therefore, when combining models those inputs are moved to the state matrix. The model for the electrical system after moving the inputs is shown in Equation (C.18).

$$\Delta\dot{\mathbf{X}}_{STe} = \mathbf{A}'_{STe}\Delta\mathbf{X}_{STe} + \mathbf{B}_{STe}\Delta\mathbf{U}_{STe} + \mathbf{E}_{STe}\Delta\mathbf{V} + \mathbf{F}_{STe}\Delta\mathbf{Z} \tag{C.18}$$

where,

$$\Delta\mathbf{X}_{STe} = [\Delta\mathbf{X}_{tf}, \Delta\mathbf{X}_{ph}, \Delta\mathbf{X}_{fil}, \Delta V_{dc}, \Delta\mathbf{X}_{pl}]^T, \qquad \Delta\mathbf{U}_{STe} = [\Delta m, \Delta\delta]^T$$

Note that Equation (C.18) consists of $\Delta\mathbf{Z}$ which do not contain either states, inputs or terminal voltage terms. Therefore, those algebraic variables need to be eliminated from the final state space model. To eliminate $\Delta\mathbf{Z}$, a large fictitious resistor R_{sh} connected to the ground from the filter bus is used. Then using Ohm's law and Kirchhoff's current law at the filter bus, the filter bus voltages can be easily found in terms of the states as

$$\Delta\mathbf{Z} = \mathbf{A}_{sh}\Delta\mathbf{X}_{STe} \tag{C.19}$$

where,

$$\mathbf{A}_{sh} = \begin{bmatrix} R_{sh} & 0 & -R_{sh} & 0 & -R_{sh} & 0 & 0 & 0 & 0 & 0 & 0 \\ 0 & R_{sh} & 0 & -R_{sh} & 0 & -R_{sh} & 0 & 0 & 0 & 0 & 0 \end{bmatrix}$$

Therefore, the final electrical model of the STATCOM is obtained using Equations (C.18) and (C.19) in the from,

$$\Delta\dot{\mathbf{X}}_{STe} = \mathbf{A}_{STe}\Delta\mathbf{X}_{STe} + \mathbf{B}_{STe}\Delta\mathbf{U}_{STe} + \mathbf{E}_{STe}\Delta\mathbf{V}, \tag{C.20}$$

where, $\mathbf{A}_{STe} = \mathbf{A}'_{STe} + \mathbf{F}_{STe}\mathbf{A}_{sh}$.

C.6 STATCOM Controller Model

Cascaded PI controllers are used to control the STATCOM with a slower outer loop and a faster inner current control loop. One outer loop controller controls the dc voltage across the capacitor while the other outer loop controller controls the STATCOM terminal voltage. The inner loops control the current flowing into the STATCOM through the transformer in an orthogonal rotating axis frame. The direct axis (d-axis) of this rotating frame is selected so that it is along the STATCOM terminal voltage where as its quadrature axis (q-axis) is is selected as it is leading the direct axis. Since the STATCOM is assumed to have no active power control capability and its own active power consumption is negligible compared to the reactive power injection/absorption, the direct axis component of the current is assumed to be zero. Therefore, only the ac voltage controller is assumed to have an inner current loop. The output of the voltage controller inner current loop produces the angle order for the converter terminal voltage whereas the dc voltage controller output produces the modulation index of the converter. The STATCOM controllers and the selection of the $d-q$ axis frame is shown in Figure C.4. The measuring transducers used to measure the ac and dc voltages and the STATCOM current are represented by the three single pole transfer functions in the block diagrams.

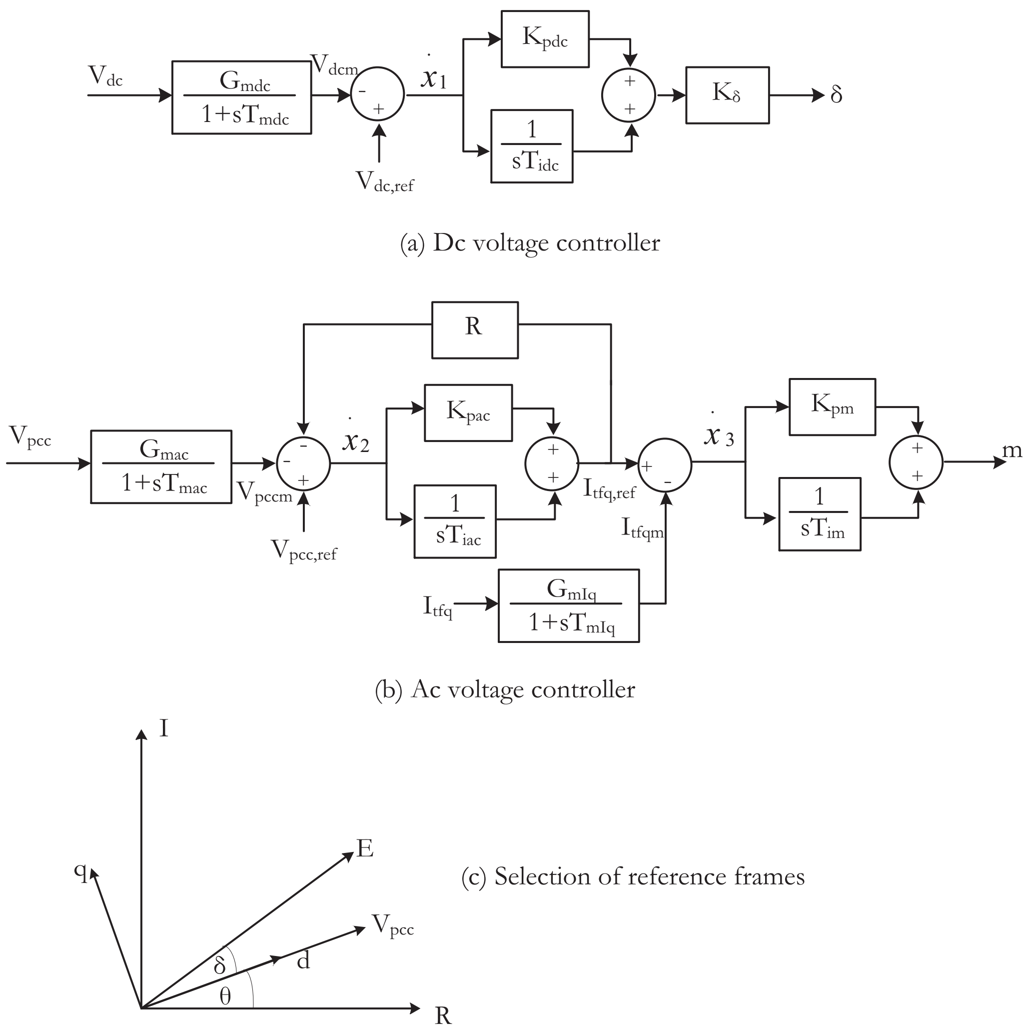

Figure C.4: STATCOM controllers: (a) DC voltage controller; (b) AC voltage controller; (c) Selection of reference frames

C.6.1 DC Voltage Controller

The dynamic model for the dc voltage controller can be written from the block diagram shown in Figure C.4(a) as,

$$\dot{V}_{dc} = \frac{1}{T_{mdc}}\left(G_{mdc}V_{dc} - V_{dcm}\right) \tag{C.21}$$

$$\dot{x}_1 = V_{dc,ref} - V_{dcm} \tag{C.22}$$

The output of the ac voltage controller can be expressed as,

$$\delta = K_\delta\left(K_{pdc}\dot{x}_1 + \frac{1}{T_{idc}}x_1\right) \tag{C.23}$$

Note that the gain K_δ is the radian to degrees conversion factor. The small signal model of the dc voltage controller is obtained by linearizing Equations (C.21 - C.23).

$$\Delta\dot{\mathbf{X}}_{dcc} = \mathbf{A}_{dcc}\Delta\mathbf{X}_{dcc} + \mathbf{B}_{dcc}\Delta\mathbf{U}_{dcc} \tag{C.24}$$

$$\Delta\delta = \mathbf{C}_{dcc}\Delta\mathbf{X}_{dcc} + \mathbf{D}_{dcc}\Delta\mathbf{U}_{dcc} \tag{C.25}$$

where,

$$\Delta\mathbf{X}_{dcc} = \left[\Delta V_{dcm}, \Delta x_1\right]^T, \qquad \Delta\mathbf{U}_{dcc} = \left[\Delta V_{dc,ref}, \Delta V_{dc}\right]^T$$

$$\mathbf{A}_{dcc} = \begin{bmatrix} -\frac{1}{T_{mdc}} & 0 \\ -1 & 0 \end{bmatrix}, \quad \mathbf{B}_{dcc} = \begin{bmatrix} 0 & \frac{G_{mdc}}{T_{mdc}} \\ 1 & 0 \end{bmatrix}, \quad \mathbf{C}_{dcc} = \begin{bmatrix} -K_\delta K_{pdc} & K_\delta K_{idc} \end{bmatrix}, \quad \mathbf{D}_{dcc} = \begin{bmatrix} K_\delta K_{pdc} & 0 \end{bmatrix}$$

C.6.2 AC Voltage Controller

The ac voltage controller shown in Figure C.4(b) is used to control the STATCOM terminal voltage at the set value with a droop R. The dynamic model for the ac voltage controller is given in Equations (C.26 - C.28).

$$\begin{aligned}
\dot{V}_{pccm} &= \frac{1}{T_{mac}}\left(G_{mac}V_{pcc} - V_{pccm}\right) && \text{(C.26)}\\
\dot{x}_2 &= \frac{1}{1+RK_{pac}}\left(V_{pcc,ref} - V_{pccm} - RK_{iac}x_2\right) && \text{(C.27)}\\
\dot{x}_3 &= K_{pac}\dot{x}_2 + K_{iac}x_2 - I_{tfqm} && \text{(C.28)}\\
\dot{I}_{tfqm} &= \frac{1}{T_{mIq}}\left(G_{mIq}I_{tfq} - I_{tfqm}\right) && \text{(C.29)}
\end{aligned}$$

The output of the ac voltage controller, the modulation index of the converter is given by,

$$m = K_{pm}\dot{x}_3 + K_{im}x_3 \tag{C.30}$$

In the electrical model of the STATCOM the voltage and currents were expressed in the $R-I$ frame. But the ac voltage controller operates in the $d-q$ frame as explained earlier in this chapter. Therefore, the quadrature axis component of the STATCOM current need to be expressed in the $R-I$ frame in order to facilitate the amalgamation of the ac voltage controller with the rest of the STATCOM model. The relationship between the two reference frames is derived from the phasor diagram shown in Figure C.4(c) as,

$$\begin{aligned}
I_{tfd} &= I_{tfR}\cos\theta + I_{tfI}\sin\theta && \text{(C.31)}\\
I_{tfq} &= -I_{tfR}\sin\theta + I_{tfI}\cos\theta && \text{(C.32)}
\end{aligned}$$

The small signal model of the ac voltage controller is obtained by linearizing Equations (C.26 - C.30). The linearized equations can be expressed in the state space form as,

$$\Delta\dot{\mathbf{X}}_{acc} = \mathbf{A}_{acc}\Delta\mathbf{X}_{acc} + \mathbf{B}_{acc}\Delta\mathbf{U}_{acc} + \mathbf{E}_{acc}\Delta\mathbf{V} \tag{C.33}$$

$$\Delta m = \mathbf{C}_{acc}\Delta\mathbf{X}_{acc} + \mathbf{D}_{acc}\Delta\mathbf{U}_{acc} \tag{C.34}$$

where,

$$\Delta\mathbf{X}_{acc} = [\Delta V_{acm}, \Delta x_2, \Delta x_3, \Delta I_{tfqm}]^T, \qquad \Delta\mathbf{V} = [\Delta V_{pccR}, \Delta V_{pccI}]^T,$$

$$\Delta\mathbf{U}_{acc} = [\Delta V_{ac,ref}, \Delta I_{tfR}, \Delta I_{tfI}, \Delta\theta]^T,$$

$$\mathbf{A}_{acc} = \begin{bmatrix} a_{acc}^{11} & 0 & 0 & 0 \\ a_{acc}^{21} & a_{acc}^{22} & 0 & 0 \\ a_{acc}^{31} & a_{acc}^{32} & 0 & -1 \\ a_{acc}^{41} & 0 & 0 & 0 \end{bmatrix}, \qquad \mathbf{B}_{acc} = \begin{bmatrix} 0 & 0 & 0 & 0 \\ b_{acc}^{21} & 0 & 0 & 0 \\ b_{acc}^{31} & 0 & 0 & 0 \\ 0 & b_{acc}^{42} & b_{acc}^{43} & b_{acc}^{44} \end{bmatrix},$$

$$\mathbf{E}_{acc} = \begin{bmatrix} e_{acc}^{11} & e_{acc}^{12} \\ 0 & 0 \\ 0 & 0 \\ 0 & 0 \end{bmatrix}, \qquad \mathbf{C}_{acc} = \begin{bmatrix} c_{acc}^{11} & c_{acc}^{12} & c_{acc}^{13} & c_{acc}^{14} \end{bmatrix}, \quad \mathbf{D}_{acc} = \begin{bmatrix} d_{acc}^{11} & 0 & 0 & 0 \end{bmatrix},$$

$$a_{acc}^{11} = -\frac{1}{T_{mac}}, \qquad a_{acc}^{21} = -\frac{1}{1 + RK_{pac}}, \qquad a_{acc}^{22} = -\frac{RK_{iac}}{1 + RK_{pac}},$$

$$a_{acc}^{31} = K_{pac}a_{acc}^{21}, \qquad a_{acc}^{32} = K_{pac}a_{acc}^{22} + K_{iac}, \qquad a_{acc}^{41} = -\frac{1}{T_{mIq}},$$

$$b_{acc}^{21} = -a_{acc}^{21}, \quad b_{acc}^{31} = K_{pac} b_{acc}^{21}, \quad b_{acc}^{42} = -\frac{G_{mIq}\sin\theta_0}{T_{mIq}}, \quad b_{acc}^{43} = \frac{G_{mIq}\cos\theta_0}{T_{mIq}},$$

$$b_{acc}^{44} = \frac{G_{mIq}}{T_{mIq}}\left(-I_{tfR0}\cos\theta_0 - I_{tfI0}\sin\theta_0\right), \quad e_{acc}^{11} = \frac{G_{mac}V_{pccR0}}{T_{mac}V_{pcc0}}, \quad e_{acc}^{12} = \frac{G_{mac}V_{pccI0}}{T_{mac}V_{pcc0}},$$

$$c_{acc}^{11} = K_{pm} a_{acc}^{31}, \quad c_{acc}^{12} = K_{pm} a_{acc}^{32}, \quad c_{acc}^{13} = K_{im}, \quad c_{acc}^{14} = K_{pm} a_{acc}^{34}, \quad d_{acc}^{11} = K_{pm} b_{acc}^{31}.$$

The complete controller model for the STATCOM is obtained by collecting the states, inputs and terminal voltage terms in the ac and dc voltage controller models. The combined controller model is shown in Equations (C.35) and (C.36).

$$\Delta\dot{\mathbf{X}}_{STc} = \mathbf{A}_{STc}\Delta\mathbf{X}_{STc} + \mathbf{B}_{STc}\Delta\mathbf{U}_{STc} + \mathbf{E}_{STc}\Delta\mathbf{V} \tag{C.35}$$

$$\Delta\mathbf{Y}_{STc} = \mathbf{C}_{STc}\Delta\mathbf{X}_{STc} + \mathbf{D}_{STc}\Delta\mathbf{U}_{STc} \tag{C.36}$$

where,

$$\Delta\mathbf{X}_{STc} = \left[\Delta\mathbf{X}_{dcc}, \Delta\mathbf{X}_{acc}\right]^T, \quad \Delta\mathbf{U}_{acc} = \left[\Delta\mathbf{U}_{dcc}, \Delta\mathbf{U}_{acc}\right]^T, \quad \Delta\mathbf{Y}_{STc} = \left[\Delta\delta, \Delta m\right]^T,$$

$$\mathbf{A}_{STc} = \begin{bmatrix} \mathbf{A}_{dcc} & 0 \\ 0 & \mathbf{A}_{acc} \end{bmatrix}, \quad \mathbf{B}_{STc} = \begin{bmatrix} \mathbf{B}_{dcc} & 0 \\ 0 & \mathbf{B}_{acc} \end{bmatrix}, \quad \mathbf{E}_{STc} = \begin{bmatrix} 0 \\ \mathbf{E}_{acc} \end{bmatrix},$$

$$\mathbf{C}_{STc} = \begin{bmatrix} \mathbf{C}_{dcc} & 0 \\ 0 & \mathbf{C}_{acc} \end{bmatrix}, \quad \mathbf{D}_{STc} = \begin{bmatrix} \mathbf{D}_{dcc} & 0 \\ 0 & \mathbf{D}_{acc} \end{bmatrix}.$$

The final STATCOM model is obtained by combining the electrical and controller models derived above. When combining the two models all the states are grouped together and put into one state matrix. Note that the inputs to the electrical models are in fact outputs of the controller model. Therefore, Equation (C.36) is used to eliminate the two inputs of the electrical model. Also note that ΔV_{dc}, ΔI_{tfR}, ΔI_{tfI} and $\Delta\theta$ inputs in the controller model are considered as states in the electrical model. Therefore, when combining the two models those inputs are moved to the state matrix. The final state space model of the STATCOM will be in the form shown in (C.37).

$$\Delta\dot{\mathbf{X}}_{STAT} = \mathbf{A}_{STAT}\Delta\mathbf{X}_{STAT} + \mathbf{B}_{STAT}\Delta\mathbf{U}_{STAT} + \mathbf{E}_{STAT}\Delta\mathbf{V} \tag{C.37}$$

$$\tag{C.38}$$

where,

$$\Delta\mathbf{X}_{STAT} = [\Delta\mathbf{X}_{STe}, \Delta\mathbf{X}_{STc}]^T, \qquad \Delta\mathbf{U}_{STAT} = [\Delta V_{dc,ref}, \Delta V_{ac,ref}]^T.$$

Acronyms

DFIG	Doubly-Fed Induction Generator
FACTS	Flexible Alternative Current Transmission System
HVDC	High Voltage Direct Current
IEEE	Institute of Electrical and Electronics Engineers
SSR	Sub-Synchronous Resonance
WPP	Wind Power Plant
SVC	Static Var Compensator
STATCOM	Static Synchronous Compensator
TSR	Tip Speed Ratio
RSC	Rotor Side Converter
GSC	Grid Side Converter
PWM	Pulse Width Modulation
EMT	Electro Magnetic Transient
SSI	Sub-Synchronous Interaction
SSTI	Sub-Synchronous Torsional Interaction
PCC	Point of Common Coupling
MIMO	Multiple Input Multiple Output
SMIB	Single Machine to Infinite Bus
TCR	Thyristor Controlled Reactor
TSC	Thyristor Switched Capacitor
AC	Alternating Current
DC	Direct Current
MV	Medium Voltage
HV	High Voltage
RMS	Root Mean Square
PI	Proportional and Integral (controller)
SSDC	Sub-Synchronous Damping Controller

References

[1] World Wind Energy Association, "World wind energy report 2011", [Online] Available: http://www.wwindea.org/webimages/WorldWindEnergyReport2011.pdf, May 2012.

[2] European Union, "The european strategic energy technology plan: Towards a low carbon future", [Online] http://ec.europa.eu/energy/publications/doc/2010_setplan_brochure.pdf, 2010.

[3] European Wind Energy Association, "The european wind initiative", [Online] Available: http://www.ewea.org/fileadmin/ewea_documents/documents/publications/EWI/EWI_2010_final.pdf, June 2010.

[4] J. Daniel, C. Han, S. Hutchinson, R. Koessler, D. Martin, G. Shen, and W. Wong, "ERCOT CREZ reactive power compensation study", Tech. Rep., Grid Systems Consulting Group, Power Systems Division, ABB Inc, 2010.

[5] T. Ackermann, *Wind Power in Power Systems*, Wiley, 2005.

[6] ABB, "Technical application papers no.13: Wind power plants", Tech. Rep., ABB, 2011.

[7] J. W. Butler and C. Concordia, "Analysis of series capacitor application problems", *AIEE Trans.*, vol. 56, pp. 975–988, Aug. 1937.

[8] R. G. Farmer, A. L. Schwalb, and Eli Katz, "Navajo project report on subsynchronous resonanceanalysis and solutions", *IEEE Trans. Power App. Syst.*, vol. PAS-96, no. 4, pp. 1226–1232, Jul./Aug. 1977.

[9] IEEE subsynchronous working group, "Readers guide to subsynchronous resonance", *IEEE Trans. Power Syst.*, vol. 7, no. 1, pp. 150–157, Feb. 1992.

[10] P. M. Anderson, B. L. Agrawal, and J. E. Van Ness, *Subsynchronous resonance in power systems*, IEEE Press, 1990.

[11] P. Pourbeik, D.G. Ramey, N. Abi-Samra, D. Brooks, and A. Gaikwad, "Vulnerability of large steam turbine generators to torsional interactions during electrical grid disturbances", *IEEE Trans. Power Syst.*, vol. 22, no. 3, pp. 1250 –1258, Aug. 2007.

[12] C. Karawita and U. D. Annakkage, "Multi-infeed HVDC interaction studies using small-signal stability assessment", *IEEE Trans. Power Del.*, vol. 24, no. 2, pp. 910–910, Apr. 2009.

[13] N. Rostamkolai, R.J. Piwko, E.V. Larsen, D.A. Fisher, M.A. Mobarak, and A.E. Poitras, "Subsynchronous interactions with static var compensators-concepts and practical implications", *IEEE Trans. Power Syst.*, vol. 5, no. 4, pp. 1324 –1332, Nov 1990.

[14] M. Elfayoumy and C. G. Moran, "A comprehensive approach for subsynchronous resonance screening analysis using frequency scanning technique", in *Proc. IEEE PowerTech Conference*, Bologna, Italy, Jun. 23-26, 2003, pp. 1–5.

[15] N. Johansson, L. Ängquist, and H.-P. Nee, "A comparison of different frequency scanning methods for study of subsynchronous resonance", *IEEE Trans. Power Syst.*, vol. 26, no. 1, pp. 356–363, Feb. 2011.

[16] L. A. Kilgore, D. G. Ramey, and M. C. Hall, "Simplified transmission and generation system analysis procedures for subsynchronous resonance problems", *IEEE Trans. Power App. Syst.*, vol. PAS-96, no. 6, pp. 1840–1846, Nov. 1977.

[17] B. L. Agrawal and R. G. Farmer, "Use of frequency scanning techniques for subsynchronous resonance analysis", *IEEE Trans. Power App. Syst.*, vol. PAS-98, no. 2, pp. 341–349, Mar./Apr. 1979.

[18] M. A. Pai, D. P. Sen Gupta, and K. R. Padiyar, *Small Signal Analysis of Power Systems*, Alpha Science International, 2004.

[19] IEEE Commitee Report, "First benchmark model for computer simulation of subsynchronous resonance", *IEEE Trans. Power App. Syst.*, vol. PAS-96, no. 5, pp. 1565–1572, Sep./Oct. 1977.

[20] H. W. Dommel, "Digital computer solution of electromagnetic transients in single-and multi-phase networks", *IEEE Trans. Power App. Syst.*, vol. PAS-88, pp. 388–399, April 1969.

[21] K. R. Padiyar, *Analysis of Subsynchronous Resonance in Power Systems*, Kluwer Academic Publishers, 1999.

[22] R. K. Varma, S. Auddy, and Y. Semsedini, "Mitigation of subsynchronous resonancein a series-compensated wind farm using FACTS controllers", *IEEE Trans. Power Del.*, vol. 23, no. 3, pp. 1645–1654, Jul. 2008.

[23] A. Ostadi, A. Yazdani, and R. K. Varma, "Modeling and stability analysis of a DFIG-based wind-power generator interfaced with a series-compensated line", *IEEE Trans. Power Del.*, vol. 24, no. 3, pp. 1504–1514, Jul. 2009.

[24] L. Fan, R. Kavasseri, Z. L. Miao, and C. Zhu, "Modeling of DFIG-based wind farms for SSR analysis", *IEEE Trans. Power Del.*, vol. 25, no. 4, pp. 2073–2082, Oct. 2010.

[25] G. D. Irwin, A. K. Jindal, and A. L. Isaacs, "Sub-synchronous control interactions between type 3 wind turbines and series compensated AC transmission systems", in *Proc. IEEE PES General Meeting*, Detroit, MI, USA, Jul. 24-28, 2011.

[26] C. E. J. Bowler, D. H. Baker, N. A. Mincer, and P. R. Vandiveer, "Operation and test of the navajo SSR protective equipment", *IEEE Trans. Power App. Syst.*, vol. PAS-97, no. 4, pp. 1030–1035, July/Aug. 1978.

[27] D. H. Baker, G. E. Boukarim, R. D. Aquilla, and R. J. Piwako, "Subsynchronous resonance studies and mitigation methods for series capacitor", in *Proc. Power Eng. Soc. Inaugural Conf. Expo. Africa*, Durban, South Africa, Jul. 2005, pp. 386–392.

[28] A. Yan, *Multi-mode stabilization of torsional oscillations in single and multi-machine systems using excitation control*, PhD thesis, Unibersity of British Columbia, Feb. 1982.

[29] N. Perera, K. Narendra, D. Fedirchuk, R. Midence, and V. Sood, "Performance evaluation of a sub-harmonic protection relay using practical waveform", in *IEEE Electrical Power and Energy Conference (EPEC)*, London, ON, Canada, Oct. 10-12 2012, pp. 51–56.

[30] R. J. Piwko, C. A. Wegner, S. J. Kinney, and J.D. Eden, "Subsynchronous resonance performance tests of the slatt thyristor-controlled series capacitor", *IEEE Trans. Power Del.*, vol. 11, no. 2, pp. 1112–1119, Apr. 1996.

[31] L. Fan and Z. Miao, "Mitigating SSR using DFIG-based wind generation", *IEEE Trans. Sustainable Enery*, vol. 3, no. 3, pp. 349–358, Jul. 2012.

[32] K. Ogata, *Modern Control Engineering*, Prentice-Hall, New Jersey, 4th edition, 2002.

[33] O. Anaya-Lara, N. Jenkins, J. Ekanayake, P. Cartwright, and M. Hughes, *Wind Energy Generation Modelling and Control*, Wiley, UK, 2009.

[34] The MathWorks Inc., *MATLAB R2007b Documentation*.

[35] P. Kundur, *Power System Stability and Control*, MacGraw-Hill, 1st edition, 1994.

[36] J. G. Slootweg, H. Polinder, and W. L. Kling, "Dynamic modeling of a wind turbine with doubly fed induction generator", in *Proc. IEEE PowerEng. Soc. Summer Meeting*, Vancouver, BC, Canada, Jul. 15-19, 2001.

[37] J. B. Ekanayake, L. Holdsworth, X. Wu, and N. Jenkins, "Dynamic modeling of doubly fed induction generator wind turbines", *IEEE Trans. Power Syst.*, vol. 18, no. 3, pp. 803–809, May 2003.

[38] F. Mei, *Small-signal modelling and analysis of Doubly-Fed Induction Generators in wind power applications*, PhD thesis, Imperial College London, 2008.

[39] H. Li and Z. Chen, "Transient stability analysis of wind turbines with induction generators considering blades and shaft flexibility", in *Proc. 33rd Annual*

Conference of the IEEE Industrial Electronics Society (IECON), Taipei, Taiwan, Nov. 5-8, 2007.

[40] N. Kshatriya, U. D. Annakkage, F. M. Hughes, and A. M. Gole, "Optimized partial eigenstructure assignment-baseddesign of a combined PSS and active damping controller for a DFIG", *IEEE Trans. Power Syst.*, vol. 25, no. 2, pp. 866–876, May 2010.

[41] R. Pena, J. C. Clare, and G. M. Asher, "Doubly fed induction generator using back-to-back PWM converters and its application to variable speed wind-energy generation", *IEE Proc.-Electr. Power Appl.*, vol. 143, no. 3, pp. 231–241, May 1996.

[42] A. Madariaga, C. J. Martínez de Ilarduya, I. Martínez de Alegía, and J. L. Martín, "Electrical losses in multi-MW wind energy conversion systems", in *Proc. International Conference on Renewable Energies and Power Quality (ICREPQ '12)*, Santiago de Compostela, Spain, Mar. 28-30, 2012.

[43] J. L. Rodrguez-Amenedo, S. Arnalte, and J. C. Burgos, "Automatic generation control of a wind farm with variable speed wind turbines", *IEEE Trans. Energy Convers.*, vol. 17, no. 2, pp. 279–284, Jun. 2002.

[44] S. Lundberg, "Evaluation of wind farm layouts", in *Nordic Workshop on Power and Industrial Electronics*, Trondheim, Norway, 2004.

[45] L. M. Fernández, F. Jurado, and J. R. Saenz, "Aggregated dynamic model for wind farms with doubly fed induction generator wind turbines", *Renewable Energy*, vol. 33, no. 1, pp. 129–140, Jan. 2008.

[46] A. Shafiu, O. Anaya-Lara, G. Bathurst, and N. Jenkins, "Aggregated wind turbine models for power system dynamic studies", *Wind Engineering*, vol. 30, no. 3, pp. 171–186, May 2006.

[47] M. Pöller and S. Achilles, "Aggregated wind park models for analyzing power system dynamics", in *Proc. 4th International Workshop on Large-ScaleIntegration of Wind Power and Transmission Networksfor Offshore Wind farms*, Billund, Denmark, Oct.20-21 2003.

[48] C. Karawita, HVDC *interaction studies using small signal stability assessment*, PhD thesis, University of Manitoba, 2009.

[49] Manitoba HVDC Research centre, *PSCAD X4 Online Help*, May 2011.

[50] R. Gagnon, G. Turmel, C. Larose, J. Brochu, and M. Fecteau G. Sybille, "Large-scale real-time simulation of wind power plants into hydro-québec power system", in *Proc. 9th International Workshop on Large-scale Integration of Wind Power into Power Systems as well as on Transmission Networks for Offshore Wind Power Plants*, Québec City, Québec, Canada, Oct. 18-19, 2010.

[51] C. Karawita and U. D. Annakkage, "A hybrid network model for small signal stability analysis of power systems", *IEEE Trans. Power Syst.*, vol. 25, no. 1, pp. 443–451, Feb. 2010.

[52] IEEE Task Force on Load Representation for Dynamic Performance, "Standard load models for power flow and dynamic performance simulation", *IEEE Trans. Power Syst.*, vol. 10, no. 3, pp. 1302–1313, Aug. 1995.

[53] S. Jiang, U. D. Annakkage, and A. M. Gole, "A platform for validation of FACTS models", *IEEE Trans. Power Del.*, vol. 21, no. 1, pp. 484–491, Jan. 2006.

[54] N. Kshatriya, U.D. Annakkage, A.M. Gole, and I.T. Fernando, "A comparison of the use of participation factors and residues for design and location of power system stabilizers", in *Proc. X Symp. of Specialists in Electrical Operational and Expansion Planning (XSEPOPE)*, 2006.

[55] Y.Y. Hsu and C.L. Chen, "Identification of optimum location for stabiliser applications using participation factors", in *IEE Proc. C Generation, Transmission and Distribution,*, May 1987, number 3 in 134, pp. 238–244.

[56] F.L. Pagola, I.J. Perez-Arriaga, and George C. Verghese, "On sensitivities, residues and participations: applications to oscillatory stability analysis and control", *IEEE Trans. Power Syst.*, vol. 4, no. 1, pp. 278–285, Feb. 1987.

[57] Siemens PTI, *PSS/E Version 32.0.5 Documentation*, Oct. 2010.

[58] N. G. Hingorani and L. Gyugyi, *Understanding FACTS: Concepts and Technology of Flexible AC Transmission Systems*, Wiley, 2000.

[59] I.T. Fernando, W.T. Kwasnicki, and A.M. Gole, "Modeling of conventional and advanced static var compensators in an electromagnetic transients simulation program", [Online] Available: http://www.ee.umanitoba.ca/~hvdc/faq_docs /statcom.pdf.